Jürgen Köfinger

Water in Nanopores

Dissertation

April 10, 2009

Universität Wien

Für Beatrix

Kurzfassung

Wir untersuchen das Verhalten von Wasser in engen, unpolaren Poren, deren geringer Durchmesser die Wassermoleküle zwingt, sich hintereinander anzuordnen. Aufgrund dieser fast eindimensionalen räumlichen Einschränkung der Moleküle zeigt sich neuartiges physikalisches Verhalten im Vergleich zu Wasser in makroskopischen Volumina. Um diese Eigenschaften, die unter anderem von der Länge der Pore abhängen, zu untersuchen, entwickeln wir ein eindimensionales Dipol-Gittermodell, für welches wir drei mathematisch äquivalente Darstellungen ableiten. Diese bilden die Grundlage für unsere theoretischen Überlegungen und ermöglichen es uns, Poren von nanoskopischen bis makroskopischen Längen zu simulieren. Das Dipolmodell, welches wir mit Resultaten von molekularen Simulationen parametrisieren, beschreibt die freie Energetik und die Struktur von Wasser in Nanoporen quantitativ. Wir untersuchen das Füllverhalten von Kohlenstoffnanoröhren und die Ordnung der sich bildenden Wasserketten, in welchen die Moleküle durch Wasserstoffbrücken miteinander verbunden sind. Es stellt sich heraus, dass eine enge Kohlenstoffröhre in Kontakt mit einem Wasserbad bei Raumtemperatur und unter atmosphärischem Druck vollständig mit einer praktisch ununterbrochenen Wasserkette gefüllt ist, die bis zu einer makroskopischen Länge von ~ 0.1 mm dipolar geordnet ist. Um die Konsequenzen dieser Ordnungseigenschaften für das dielektrische Verhalten zu untersuchen, erweitern wir das Gittermodell um die Kinetik von Orientierungsdefekten und bestimmen die lineare Antwort von Wasserketten auf ein zeitlich veränderliches elektrisches Feld in Richtung der Röhrenachse. Die Ketten zeigen für alle Längen Debye-Relaxation, deren Ursache die Diffusion von nahezu unkorrelierten Defekten ist. Aus diesem Verhalten leiten wir einfache Ausdrücke für die statische Suszeptibilität und die Relaxationszeit für die Grenzfälle von kurzen, geordneten und langen, ungeordneten Ketten ab. Diese Ausdrücke ermöglichen es, die Ordnungseigenschaften mit Impedanzspektroskopie experimentell zu bestimmen und die grundlegenden Größen von Wasser in Nanoröhren zu messen.

Abstract

We investigate the behavior of single-file water in narrow nanopores. The quasi one-dimensional confinement changes the dynamical and structural properties of nanopore water compared to bulk water and new properties emerge. To explore these properties, which depend on the length of the pore, we develop a one-dimensional dipole lattice model and derive three mathematically equivalent representations. These pictures form the basis of our theoretical considerations and allow the simulation of pores from nanoscopic to macroscopic lengths. Parameterized with results from atomically detailed simulations, this model reproduces the free energetics and structure of nanopore water quantitatively. We investigate the filling transition of carbon nanotubes and explore the order properties of hydrogen bonded chains of water molecules within the pore. We find that narrow carbon nanotubes, which are in contact with a water bath at room temperature and atmospheric pressure, fill completely with an essentially continuous chain of water molecules, that is predominately dipole ordered up to a tube length of ~ 0.1 mm. We explore the consequences of these order properties for the dielectric behavior by determining the linear response of a single chain of water molecules to a time-dependent electric field in direction of the tube axis. To this end, we include the kinetics of orientational defects in the dipole lattice model. At all chain lengths, nanopore water shows Debye relaxation due to the diffusion of essentially uncorrelated defects. We derive simple expressions for the static dielectric susceptibility and the relaxation time in the limits of short, ordered and long, disordered chains and suggest how dielectric loss spectroscopy can be used to determine the order properties and to measure the fundamental quantities that determine the behavior of nanopore water.

Danksagung

Sehr viele Dinge beeinflussen den Erfolg eines großen Projekts wie diesem. Glück spielt eine wichtige Rolle. Pech hingegen kann mit der Unterstützung der Kolleginnen und Kollegen, Freunde und Familie überwunden werden.

Sehr vieles hängt von den persönlichen und fachlichen Fähigkeiten des Betreuers ab. Ich danke Christoph Dellago für seine vielfältige Hilfe und Unterstützung in wirklich allen Bereichen meiner Arbeit. Ich habe nicht nur fachlich, sondern auch persönlich viel von ihm gelernt und bin dafür sehr dankbar.

Kooperationen sind ein wesentlicher Bestandteil des wissenschaftlichen Lebens und bieten Gelegenheiten, direkt von anderen zu lernen. Außerdem machen sie Spaß. Ich bin Gerhard Hummer für eine inspirierende und fruchtbare Zusammenarbeit sehr dankbar. Während meines Doktoratsstudiums hatte ich auch Gelegenheit mit Bernhard Reischl und Georg Menzl bei Forschungsthemen zusammenzuarbeiten, die über den Rahmen dieser Arbeit hinausgehen. Ich möchte mich bei ihnen für die gute Zusammenarbeit, für eine großartige Zeit und eine tolle Erfahrung bedanken.

Diskussionen sind eine wichtige Grundlage wissenschaftlicher Erkenntnis, welche in unserer Arbeitsgruppe täglich gepflegt wurde. Ich möchte mich sehr herzlich bei meinen Kolleginnen und Kollegen für die anregende und produktive Arbeitsatmosphäre bedanken, die durch selbstlose Hilfe und Unterstützung geprägt war.

Wer Computersimulationen durchführt, ist auf das Funktionieren des Arbeitsplatzrechners und des Rechen-Clusters angewiesen. Dafür möchte ich mich bei unserem Systemadministrator Walter Penits und meinen Kollegen Harald Oberhofer und Philipp Geiger bedanken.

Manchmal wird die Arbeit in der Verwaltung zu wenig geschätzt, denn je besser diese gemacht wird, desto weniger sichtbar ist sie. Aus diesem Grund möchte ich mich besonders herzlich bei Christl Langstadlinger, Claudia Rennhofer und Edith Wolfsgruber für ihre Unterstützung bedanken.

Wenn man lange Stunden arbeitet, ist es wichtig, dass man sich im Büro wohlfühlt. Ich möchte mich bei Vera Momirovic bedanken, die sich immer mehr um unsere Gruppe gekümmert hat, als ihre Arbeit von ihr verlangte.

Diese Dissertation wäre ohne die finanzielle Unterstützung unterschiedlicher Institutionen nicht möglich gewesen. Ich danke dem Fonds zur Förder-

Manchmal verlangt wissenschaftliche Arbeit die volle Aufmerksamkeit. Gerade dann ist es wichtig, dass Freunde und Familie Verständnis zeigen und dafür sorgen, dass man den Kontakt nicht vernachlässigt. Dafür möchte ich mich sehr herzlich bei ihnen bedanken.

Ich bin Luise, Sabine und Karl Aigner für die Unterstützung in den letzten Jahren sehr dankbar. Ich danke meinen Eltern Rosa und Walter, die wohl den grundlegendsten Beitrag zu dieser Arbeit geleistet haben. Ich danke Beatrix Aigner für ihre Unterstützung, für den Ausgleich und die Abwechslung, die sie in mein Leben bringt.

Acknowledgements

Many things influence the success of a large project like this. Luck is an important factor. Bad luck can be overcome with the help of your colleagues, friends, and family.

A lot depends on the personal and professional skills of your supervisor. I want to thank Christoph Dellago for his help and support in all aspects of my work. I have learned a lot from him, scientifically and personally, for which I am very grateful.

Cooperations are an essential part of scientific life and offer the opportunity to learn directly from others. Besides, they are good fun. I am very thankful to Gerhard Hummer for an inspiring and fruitful cooperation. During my thesis I had the opportunity to cooperate with Bernhard Reischl and Georg Menzl on scientific projects beyond the scope of this thesis. I want to thank them for the pleasure of working with them, a great time, and a great experience.

Discussion is one of the foundations of scientific insight and in our group it has been cultivated on a daily basis. I want to thank my colleagues for the inspiring and fruitful atmosphere, where help and support have always been given selflessly.

Performing computer simulations, a lot depends on the functioning of the work station and the high performance computing facility. I want to thank our system administrator Walter Penits and my colleagues Harald Oberhofer and Philipp Geiger for their tireless support.

Sometimes, administration is not appreciated enough since the better the job is done, the less visible it is. I especially want to thank Christl Langstadlinger, Claudia Rennhofer, and Edith Wolfsgruber for their help and support.

A nice office makes it easier to work long hours. I would like to thank Vera Momirovic for taking care of our group beyond her job description.

Preface

This thesis is based on, and includes parts of the following publications:

1. Jürgen Köfinger and Christoph Dellago
   Orientational relaxation and dielectric response of nanopore water
   submitted to Phys. Rev. Lett. (2009)

2. Jürgen Köfinger, Gerhard Hummer, and Christoph Dellago,
   A one-dimensional dipole lattice model for water in narrow nanopores
   J. Chem. Phys. in print (2009)

3. Jürgen Köfinger, Gerhard Hummer, and Christoph Dellago
   Macroscopically ordered water in nanopores
   Proc. Natl. Acad. Sci. **105** (2008)

Other articles published during my PhD studies, but which are not part of this thesis:

1. Bernhard Reischl, Jürgen Köfinger, and Christoph Dellago
   The statistics of electric field fluctuations in liquid water
   Mol. Phys. in print (2009)

2. Jürgen Köfinger and Christoph Dellago
   Biasing the center of charge in molecular dynamics simulations with empirical valence bond models: free energetics of an excess proton in a water droplet
   J. Phys. Chem. B **112** (2007)

3. Jürgen Köfinger, Nigel B. Wilding, and Gerhard Kahl
   Phase behaviour of a symmetrical binary mixture
   J. Chem. Phys. **125** (2006)

4. Jürgen Köfinger, Gerhard Kahl, and Nigel B. Wilding
   Phase behaviour of a symmetrical binary mixture in a field
   Europhys. Lett. **75** (2006)

Contents

Chapter 1

Introduction

Our day to day lives rely on the transport of fluids through pipes and tubes with flows controlled by pumps and valves. Life itself depends on similar flows of water through channels in plants and trees or of blood through veins and arteries [1, 2]. Less obvious, but essential for all living beings is the role of pores with diameters in the order of the size of molecules formed by transmembrane proteins in biological cells. The physical properties of fluids confined to such molecularly narrow pores no longer comply with our every day experience with fluids in tubes of macroscopic diameters [3–5].

Transmembrane proteins control the transport of water, protons, and ions [6]. Aquaporins, for example, are found in nearly all life forms and are permeable for water molecules but not for protons [7]. Gramicidin A channels in phospholipid bilayer membranes are selective for monovalent cations [8–10]. Other prominent examples for nanopores are the proton pumps cytochrome c oxidase [11] and bacteriorhodopsin [12], and cytochrome P450 [13]. The diverse properties of these biological pores are essentially due to their different structures. What these pores have in common is that they are nonpolar or weakly polar and that they are filled with water at least temporarily [14].

Carbon nanotubes lend themselves for the study and application of these properties as they confine water in a relatively non-specific way to a nearly cylindrical volume [15]. Molecular dynamics simulations of a short and molecularly narrow carbon nanotube immersed in water at ambient conditions showed that although hydrophobic, the tube is filled with a single-file chain of hydrogen bonded molecules [16]. The filling with water of carbon nanotubes with diameters in the nanometer range has been confirmed with neutron diffraction experiments [17] and transmission electron microscopy [18]. Due to their smooth inner tube wall carbon nanotubes allow

1
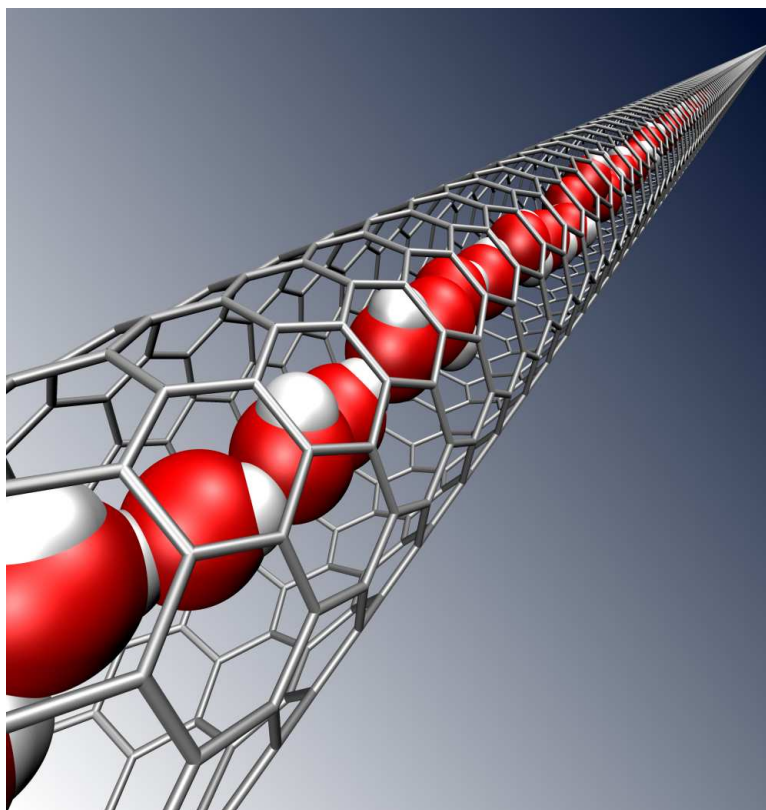
Figure 1.1: Snapshot of a molecular dynamics simulation of water in a carbon nanotube. The tube is completely filled with a single chain of hydrogen bonded molecules, oriented in the same direction.

for high, nearly friction-less fluxes as observed in gas and water flow measurements [16, 19, 20]. Additionally, these tubes can be functionalized with charges to mimic the special properties of transmembrane proteins [21, 22].

The chain of molecules that is formed within a short (6,6) type single-wall carbon nanotube is orientationally and dipolarly ordered as each water molecule donates a hydrogen bond to the molecule on the left and accepts one from the right, or the other way round, as illustrated in Fig. 1.1 [16]. Flips of the chain occur via the diffusion of orientational defects that preserve the number of hydrogen bonds and connect ordered domains of water molecules of opposite direction [23].

Such water wires allow for fast proton transport via the so-called Grotthus mechanism [8, 9, 23]. A hydronium ion within a water wire donates two hydrogen bonds to ordered domains of opposite direction. A proton donat-

ing such a bond can hop along the bond to a next neighbor molecule, thus forming a new hydronium ion, from which a different proton can hop to the next molecule. Since no water molecules have to be displaced, the proton mobility in a one-dimensional water wire exceeds that in bulk water by a factor of 40 [23]. This is in agreement with observations of gramicidin A, where the proton transport is faster than the transport of other cations [8,9]. The precondition for fast water-mediated proton transport is that the water wire is orientationally and translationally ordered [23].

This leads to the seemingly simple but fundamental question as to what tube length the translational and orientational order observed for short tubes is maintained. Based on the statistical mechanics of one-dimensional systems, one would expect this microscopic order to disappear on macroscopic length scales. In a single-file arrangement, dipole-dipole interactions dominate the energetics, decaying as $1/r^3$ with distance r. For a true order/disorder phase transition in the thermodynamic limit, that decay would have to be slower than $1/r^2$ [24,25]. Thus, strictly speaking, long-range order cannot exist in one-dimensional water chains, and defects destroying the order are bound to occur at any finite temperature for a sufficiently large system. But despite this exact result, valid in the thermodynamic limit, water chains in narrow pores may support order to large distances.

To this end, we have developed a one-dimensional dipole lattice model based on the insights of Dellago *et al.* in Ref. [23]. Parameterized against detailed molecular simulations, it quantitatively captures the free energetics of nanopore water, including particle number and defect number fluctuations [26,27].

In this dipole lattice model molecules within ordered domains are represented by dipoles parallel to the tube axis and defects by orthogonal dipoles, located on the sites of a one-dimensional lattice. We find two additional, mathematically equivalent formulations of this *dipole picture* of the model. In the *segment picture* the total energy depends on the interactions of dipole ordered domains of water molecules. It is not only of practical use for computer simulations, as it allows for an efficient implementation of the model, it is also an important step in the derivation of the *charge picture*. In this charge picture all long-range (in the sense of non-nearest neighbor) interactions are given by Coulomb-like interactions of charges located at the ends of dipole ordered domains. Defects are formed by pairs of charges of the same magnitude and sign and interact approximately Coulombically with each other and chain ends [23]. The charge picture is the physically most appealing representation and allows for a very efficient calculation of the total energy. The dipole lattice model in its different representations al-

lows us to do highly efficient Monte Carlo simulations spanning huge length scales (and in its kinetic extension also huge times scales) and builds the framework for our theoretical considerations.

For small tube lengths we observe bistable behavior of the occupancy number with similar free energies of the completely filled and the nearly empty state [16,28]. Using the dipole lattice model we quantify this behavior with respect to tube length and chemical potential and find that bistability vanishes for tube lengths $\gtrsim 300$ nm. Tubes longer than approximately 10 nm in contact with a water reservoir at atmospheric pressure and room temperature are almost completely filled, forming a nearly contiguous chain of water molecules. In the thermodynamic limit the filling transition occurs at about 8.4% relative humidity and thus we expect strong capillary action.

At ambient conditions the chain remains dipolarly ordered up to a macroscopic tube length of ~ 0.1 mm corresponding to about $\sim 10^5$ molecules. Only then, defects occur that destroy the orientational order and for tube lengths of ~ 1 cm the chain is completely disordered. Due to the low defect density the order properties are well described by assuming uncorrelated defects and defect pairs, which provides a connection to the one-dimensional Ising model, allowing the analytic calculation of the canonical partition function for fixed total dipole moment.

To date, these order properties lack experimental verification. For this reason, we investigate the dielectric response of water in nanopores and show how the order properties can be probed with dielectric spectroscopy. Based on the diffusive dynamics of orientational defects we extend the dipole lattice model to study the kinetics of a single chain of water molecules. Using this kinetic dipole lattice model, we are able to investigate the linear response of single-file water to a periodically varying electric field in direction of the tube axis, over huge length and time scales. We find that nanopore water exhibits Debye behavior due to the diffusion of highly uncorrelated defects. The dipole lattice model in the charge picture allows us to derive simple expressions for the static susceptibility and the relaxation time in the limits of small and large system sizes from which the defining properties of single-file water, like the excitation energy and diffusion constant of orientational defects, might be deduced. In the thermodynamic limit, we expect the dielectric susceptibility of a membrane of carbon nanotubes with an experimentally feasible tube density of about 2.5×10^{11} cm^{-2} to be about 100 times larger than that of bulk water although the water density in the membrane is more than 3000 times smaller than in bulk water.

Our findings strengthen and extend the important role of carbon nanotubes as promising building blocks for filter, desalination, and separation

devices [5, 29–31], fuel cells [23, 32, 33], and sensing devices [34].

We are optimistic that with the current advances in the production of carbon nanotubes, long, molecularly narrow, and pristine tubes will be available in the near future [20, 35]. Furthermore, other materials might serve as containers for macroscopically ordered water, such as water-filled boron-nitride tubes, which show very similar properties [36–39]. Another interesting possibility to confine water in molecularly narrow pores are silanized channels in silicon wafers [40].

The dipole lattice model is general and should be applicable to other quasi-one dimensional systems with dipolar interactions, including polar fluids other than water as well as magnetic nanoparticles and colloids [41–44]. It should also prove useful in studies of three-dimensionally packed arrays of one-dimensional chains, such as those formed in membranes of parallel nanochannels [26, 29].

This work is organized as follows. In Chapter 2 we introduce the dipole lattice model and derive the segment and charge picture. Based on the latter we derive approximations that neglect Coulomb-like interactions and provide additional insight in the thermodynamic properties of nanopore water. In Chapter 3 we parameterize and validate the dipole lattice model against detailed molecular simulations and present simulation and analytical results for the filling/emptying transition and the order properties of a completely filled tube. We introduce the kinetic dipole lattice model in Chapter 4 and present analytical, numerical, and simulation results for the linear dielectric response of a chain to a time-dependent homogenous electric field in direction of the tube axis.

Chapter 2

Model

2.1 Introduction

Single-file water in narrow pores can be modelled using lattice models with discrete degrees of freedom, due to the reduced mobility of the water molecules in one-dimensional (1D) confinement. Such simplified models capture the essential physics of diverse phenomena ranging from tube filling to protonic conduction and water diffusion [23, 28, 45–47]. Here, we introduce such a one-dimensional lattice model, in which water molecules are represented as point dipoles oriented either parallel or orthogonal to the tube axis [23, 26]. In contrast to other lattice models, our dipole model quantitatively reproduces the structure of quasi one-dimensional water in the tube interior including the formation of defects and their interactions. Moreover, simulations of this model are computationally inexpensive, making studies of large systems possible that would not be feasible otherwise.

We present a detailed derivation of our lattice model and its various, mathematically equivalent representations. In this model, dipoles are arranged on a regular 1D-lattice and interact via $1/r^3$ dipole-dipole interactions. This *dipole picture* can be simplified by grouping domains with equal orientation into segments. In the resulting *segment picture*, the total energy of the system is written as a sum of the internal energies of the segments and their interactions, which are of the dipole-dipole type. As we shall see, this segment picture is especially useful for the design of Monte Carlo moves that satisfy the configurational constraints dictated by the model. Resummation of the energy of the ordered segments finally leads to the *charge picture*, in which the total energy is expressed as a sum of Coulomb-like interactions of effective charges placed at the endpoints of the ordered segments. In this physically appealing picture the Coulomb-like interactions account for

7

all effective interactions of defects, chain ends, and protons. Because of its reduced computational complexity, the charge representation permits simulations of tubes of macroscopic length and investigations of the approach of the thermodynamic limit.

The charge picture lends itself to approximations in which the long-range interactions of the effective charges are neglected and which allow the investigation of the role of the Coulomb-like interactions. These approximations have a low dimensional phase space, with three and four dimensions respectively, for which we can derive analytical expressions for the density of states.

Finally, we show how the dipole lattice model and its approximations are efficiently implemented in a Monte Carlo simulation using non-local trial moves.

2.2   One-dimensional dipole lattice model

Water in nanopores forms hydrogen bonded chains of molecules. Such a chain is dipole ordered if all molecules accept a hydrogen bond from the neighboring molecule on the left and donate a hydrogen bond to a molecule on the right (or the other way round). This order is destroyed by orientational defects. Note, however, that hydrogen bonding defects within a contiguous chain preserve the total number of hydrogen bonds. Figure 2.1(a) shows a chain of water molecules that consists of three ordered segments connected by defect molecules. The segments consist of two molecules each and are orientationally ordered. The D-defect connects two segments pointing towards each other and an L-defect connects two segments pointing away from each other. In contrast to molecules within ordered segments, which donate a single hydrogen bond and accept a single hydrogen bond, the D-defect molecule accepts two hydrogen bonds without donating any and the L-defect donates two hydrogen bonds without accepting any. This also means, that defects cannot be located at chain ends. Another configurational constraint is that defects can not be located next to each other, because the corresponding molecular configurations are unstable and lead to immediate recombination of the defects. Note, that the defect structures shown in Fig. 2.1(a) are the most typical configurations, but others can occur as well.

The free energetics of such a chain of water molecules are captured with great accuracy by a one-dimensional dipole lattice model. Molecular simulations show that, due to the hydrogen bonds, the water molecules are on average located on the sites of a one-dimensional lattice and that the
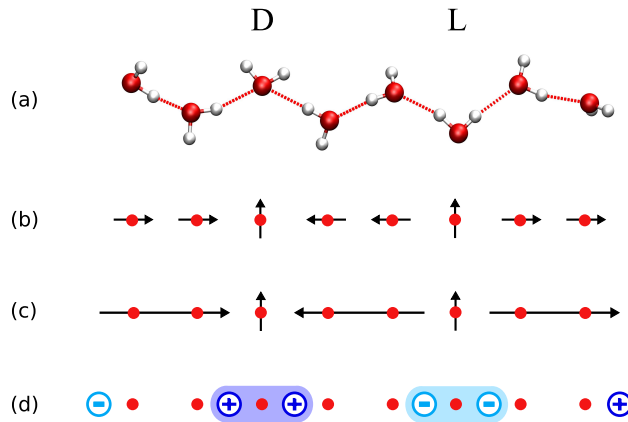
Figure 2.1: 1D water wires in nanopores. (a) Chain configuration with a D-defect and an L-defect, and the corresponding lattice model in the (b) dipole representation, (c) the segment representation, and (d) the effective charge representation. In the lattice model, sites are marked by filled circles, dipoles are represented by short arrows, segments by long arrows, and effective charges by circles with their sign at the center. (a) The D-defect molecule accepts two hydrogen bonds from the two neighboring water molecules; in contrast, the L-defect molecule donates two hydrogen bonds. (b) The next neighbor dipoles of the defect sites point to the defect site for the D-defect and away from it for the L-defect. (c) The configurational energy of the water wire due to the dipoles is determined by the length, orientation, and distance of segments. (d) In the effective charge representation, the segments are replaced by charges at the their ends with signs according to their orientations. As a consequence, defects are formed by pairs of equal charges which are positive for the D- and negative for the L-defect.

long-range interaction of water molecules in an ordered chain is given by the dipole-dipole interaction. The magnitude of the dipoles is given by the average of the component of the dipole moment along the tube axis of a water molecule in an ordered chain. As a consequence, in the dipole model an ordered segment consists of equally oriented dipoles parallel to the tube axis, located on the site of a one-dimensional lattice [Fig. 2.1(b)]. The dipole moments of defect molecules are on average perpendicular to the tube axis and we only include their next-neighbor interactions.

On this basis, we can formulate an effective Hamiltonian with a reduced number of degrees of freedom. This Hamiltonian describes the free energetics of arbitrarily filled tubes that in general consist of ordered or disordered hydrogen bonded chains of water molecules (or fragments), with gaps be-

tween them.

Let us assume that our lattice has N sites. The lattice spacing is a and the dipole moment p. A dipole located on site ν has a direction $\sigma_\nu = 1$ if it points "up", and $\sigma_\nu = -1$ if it points "down" the tube axis. The interaction potential of two dipoles located on sites ν and μ separated by a distance $d_{\nu\mu} = |\nu - \mu|a \neq 0$ is given by

$$\phi_{\nu\mu} = -\epsilon \frac{\sigma_\nu \sigma_\mu}{|\nu - \mu|^3} \, . \qquad (2.1)$$

If a site ν carries a defect or if it is empty, we assign this site $\sigma_\nu = 0$. In these cases Eq. (2.1) remains valid as $\phi_{\nu\mu} = 0$. Here, we introduced the energy $\epsilon = 2p^2/(4\pi\varepsilon_0 a^3)$, where ε_0 is the dielectric constant, setting the scale for the dipole-dipole interaction. In the following, we use reduced units, i.e., ϵ as unit for the energy, a as unit for the length, and p as unit for the dipole moment.

2.2.1   Dipole picture

Molecular simulations show that the interaction energy of next neighbor molecules, the so-called *contact energy*, is different from the dipole-dipole interaction energy of next neighbors, which is given by $\phi_{\nu,\nu+1} = -1$ for $\sigma_\nu \sigma_{\nu+1} = 1$. It will be useful to include the next neighbor dipole-dipole interaction in the Hamiltonian and correct for it to get the right contact energies. Let the configuration consist of n water molecules (occupied sites), n_c hydrogen bonded chains of molecules (fragments), and n_d defects. We add the contact energy E_c for each of the $(n - n_c)$ hydrogen bonds and subtract the next neighbor dipole interaction for the $(n - n_c - 2n_d)$ next neighbor pairs of parallel dipoles. This leads to the following effective Hamiltonian for water in nanopores

$$H = \sum_{\nu=1}^{N-1} \sum_{\mu=\nu+1}^{N} \phi_{\nu\mu} + (n - n_c)(1 + E_c) - 2n_d + n_c S_c \, , \qquad (2.2)$$

where the double sum extends over all pairs of sites. S_c is an entropic contribution that accounts for the different contributions to the phase space volume of molecules at the chain ends and at defect sites compared to molecules within the chain. These different contributions are related to the number of dangling OH bonds (see Sec. 3.2). As we will see, this Hamiltonian is just one of three equivalent descriptions of the system. We will refer to this way of calculating the Hamiltonian as the *dipole picture* [see Fig. 2.1(b)], as we sum over all dipole-dipole interactions.

2.2.2 Segment picture

We can also formulate the Hamiltonian of Eq. (2.2) in terms of the $n_{\mathrm{s}} = n_{\mathrm{c}} + n_{\mathrm{d}}$ segments, numbered from left to right, leading to the so-called *segment picture* [see Fig. 2.1(c)].

For this purpose, we need the *dipolar internal energy* of a segment, which stems from the interaction of the dipoles within a segment, and the *dipolar interaction energy* of two segments, which stems from the interaction of dipoles belonging to two different segments. For the sake of brevity, we will drop the term "dipolar" and speak only of internal and interaction energies of segments in the following.

The beginning of the segment with index i is given by its coordinate x_i and its length is denoted by l_i. The coordinates of the dipoles of segment i are given by $x_i + n - 1/2$ with $1 \leq n \leq l_i$. As all dipoles within a segment i have the same direction, i.e., $\sigma_\nu = s_i$ for all dipoles within the segment i, we assign each segment a direction $s_i = \pm 1$. The internal energy $E(l_i)$ of a segment i is given by the sum over all pair interactions of dipoles ν within the segment, i.e. ,

$$E(l_i) = -\sum_{\nu=1}^{l_i-1} \sum_{\mu=\nu+1}^{l_i} \frac{1}{|\mu - \nu|^3} \, . \tag{2.3}$$

The interaction energy $I(l_i, l_j, s_i s_j, \Delta l_{ij}) \equiv I_{ij}$ of segments i and j, with $i < j$, is defined as

$$I_{ij} = -s_i s_j \sum_{\nu=1}^{l_i} \sum_{\mu=1}^{l_j} \frac{1}{(\mu - \nu + \Delta l_{ij} + l_i)^3} \, , \tag{2.4}$$

with the size of the gap between the two segments given by $\Delta l_{ij} = x_j - (x_i + l_i) > 0$.

In the segment picture we obtain for the Hamiltonian

$$\begin{aligned} H &= \sum_{i=1}^{n_{\mathrm{s}}} E(l_i) + \sum_{i=1}^{n_{\mathrm{s}}-1} \sum_{j=i+1}^{n_{\mathrm{s}}} I_{ij} + \\ &+ (n - n_{\mathrm{c}})(1 + E_{\mathrm{c}}) - 2n_{\mathrm{d}} + n_{\mathrm{c}} S_{\mathrm{c}} \, . \end{aligned} \tag{2.5}$$

The calculation of the energy according to Eq. (2.5) in the segment picture can be simplified considerably by deriving an explicit functional form for the internal energy and expressing the interaction energies in terms of the internal energy. First, we can avoid the double sum in the calculation of the internal energy of Eq. (2.3) by counting all pairs of dipoles separated by a certain distance. In a segment of length l, the interaction potential of

dipoles separated by a distance j with $1 \leq j < l$ appears $(l - j)$ times. This leads to

$$
\begin{aligned}
E(l) & = & -\sum_{j=1}^{l-1}(l-j)j^{-3} = \\
& = & \sum_{j=1}^{l-1}j^{-2} - l\sum_{j=1}^{l-1}j^{-3}
\end{aligned}
\tag{2.6}
$$

for Eq. (2.3).

For $l \to \infty$, the two sums in Eq. (2.6) can be expressed in terms of Riemann's zeta function [48]

$$
\zeta(m) = \sum_{j=1}^{\infty} j^{-m} \,.
\tag{2.7}
$$

Accordingly, for long segments we can approximate the internal energy $E(l)$ as

$$
E_{l \gg 1}(l) = \zeta(2) - l\zeta(3) \,.
\tag{2.8}
$$

The difference, $\Phi(l) = E_{l \gg 1}(l) - E(l)$, between the above approximation and the exact internal energy is given by

$$
\Phi(l) = \sum_{j=l}^{\infty} \frac{1}{j^2} - l\sum_{j=l}^{\infty} \frac{1}{j^3}
\tag{2.9}
$$

and can be rewritten as

$$
\Phi(l) = \Psi'(l) + \frac{l}{2}\Psi''(l)
\tag{2.10}
$$

using the polygamma function [48]

$$
\Psi^{(m)}(l) = (-1)^{m+1}m! \sum_{j=0}^{\infty} \frac{1}{(l+j)^{m+1}} \,.
\tag{2.11}
$$

Hence, the internal energy of a segment of length l can be written as the sum of a linear part, Eq. (2.8), and a non-linear part, Eq. (2.10), leading to the exact expression

$$
E(l) = \zeta(2) - l\zeta(3) - \Phi(l) \,.
\tag{2.12}
$$

The next step towards a simpler energy calculation in the segment picture is to express the interaction energy of two segments i and j in terms of internal energies (see Fig. 2.2). As the directions of the segments only

$$l_i \qquad\qquad \Delta l_{ij} \qquad\qquad l_j$$

(a)   + E(   )

(b)   - E(   )

(c)   - E(   )

(d)   + E(   )

_____

(e)   = I(   )
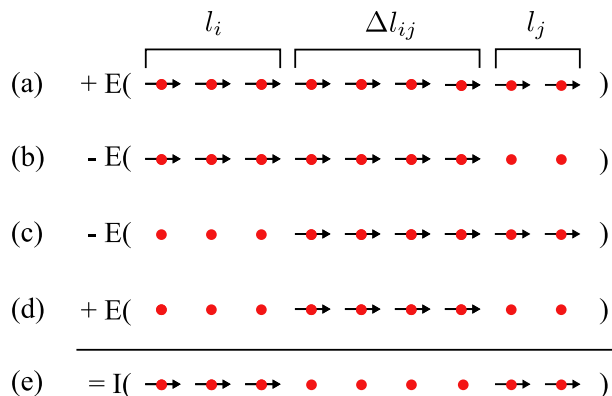
Figure 2.2: Calculation of the interaction energy. The interaction energy I of configuration (e), consisting of two chains of length l_i and l_j, separated by a distance, Δl_{ij}, of four sites, can be calculated by subtracting the internal energies E of configurations (b) and (c) from the internal energy of (a), and adding the internal energy of the configuration (d).

determine the sign of their interaction energy, we assume, for the moment, that the two segments of length l_i and l_j have the same direction, as depicted in Fig. 2.2 (e).

In the following we use the simple fact that the internal energy $E(l)$ of a chain of length l can be calculated from its parts of length l' and l'', with $l = l' + l''$, as

$$E(l) = E(l') + E(l'') + I(l', l'', 1, 0)\,. \qquad (2.13)$$

For brevity we drop s_{ij} and Δl_{ij} as arguments of $I(l_i, l_j, s_{ij}, \Delta_{ij}) \equiv I(l_i, l_j)$ here. Using the equation above the internal energy of a segment with length $l = l_i + l_j + \Delta l_{ij}$ [Fig. 2.2 (a)] can be written as

$$\begin{aligned} E(l) &= E(l_i) + E(l_j) + E(\Delta l_{ij}) + \\ &+ I(l_i, l_j) + I(l_i, \Delta l_{ij}) + I(\Delta l_{ij}, l_j)\,. \end{aligned} \qquad (2.14)$$

To get the desired interaction energy, $I(l_i, l_j)$ on the right hand side of Eq. (2.14), we subtract the internal energies of a segment of length $l_i + \Delta l_{ij}$ and of a segment of length $\Delta l_{ij} + l_j$ [Fig. 2.2 (b) and (c)] . These two energies, given by

$$E(l_i + \Delta l_{ij}) = E(l_i) + E(\Delta l_{ij}) + I(l_i, \Delta l_{ij}) \qquad (2.15)$$

and

$$E(\Delta l_{ij} + l_j) = E(\Delta l_{ij}) + E(l_j) + I(\Delta l_{ij}, l_j)\,, \qquad (2.16)$$

include the internal energies of the two segments i and j, and the interaction energies of the segment i and j with the segment of length Δl_{ij} separating them. They also include twice the internal energy $E(\Delta l_{ij})$ of the segment in the middle. To correct for this double subtraction, we have to add this energy once, Fig. 2.2 (d). As the linear terms of Eq. (2.12) cancel, we obtain for the interaction energy

$$
\begin{aligned}
I_{ij} \;=\; & -s_i s_j \left[\Phi(l_i + l_j + \Delta l_{ij}) + \Phi(\Delta l_{ij}) + \right. \\
& \left. -\Phi(l_i + \Delta l_{ij}) - \Phi(l_j + \Delta l_{ij}) \right] .
\end{aligned} \tag{2.17}
$$

Note that this expression for the interaction energy is also valid for continuous gap distances $\Delta l_{ij} \geq 0$.

This result can also be obtained by simply inserting the expressions for the interaction energies $I(l_i, \Delta l_{ij})$ and $I(\Delta l_{ij}, l_j)$ following from Eqs. (2.15) and (2.16),

$$
\begin{aligned}
I(l_i, \Delta l_{ij}) \;&=\; E(l_i + \Delta l_{ij}) - E(l_i) - E(\Delta l_{ij}) \tag{2.18} \\
I(\Delta l_{ij}, l_j) \;&=\; E(\Delta l_{ij} + l_j) - E(\Delta l_{ij}) - E(l_j) \tag{2.19}
\end{aligned}
$$

into Eq. (2.14).

Using Eqs. (2.12) and (2.17) we can write the total energy in the segment picture, Eq. (2.5), as

$$
\begin{aligned}
H \;=\; & -\sum_{i=1}^{n_{\mathrm{s}}-1} \sum_{j=i+1}^{n_{\mathrm{s}}} s_i s_j \left[\Phi(l_i + l_j + \Delta l_{ij}) + \Phi(\Delta l_{ij}) + \right. \\
& \left. -\Phi(l_i + \Delta l_{ij}) - \Phi(l_j + \Delta l_{ij}) \right] - \sum_{i=1}^{n_{\mathrm{s}}} \Phi(l_i) + \\
& + n_{\mathrm{d}} c_{\mathrm{d}} + n_{\mathrm{c}} c_{\mathrm{c}} + n c \, .
\end{aligned} \tag{2.20}
$$

This Hamiltonian contains terms linear in the number of defects n_{d}, the number of fragments n_{c}, and the number of occupied sites n. The corresponding coefficients c_{d}, c_{c}, and c, which depend on the contact energy E_{c} and the entropic contribution S_{c}, are given by

$$
\begin{aligned}
c_{\mathrm{d}} \;&=\; \zeta(2) + \zeta(3) - 2 \, , \tag{2.21} \\
c_{\mathrm{c}} \;&=\; \zeta(2) - 1 - E_{\mathrm{c}} + S_{\mathrm{c}} \, , \tag{2.22} \\
c \;&=\; 1 + E_{\mathrm{c}} - \zeta(3) \, . \tag{2.23}
\end{aligned}
$$

2.2.3   Charge picture

We can use this expression for the Hamiltonian in the *segment picture* to derive another equivalent description of the system, the so-called *charge*
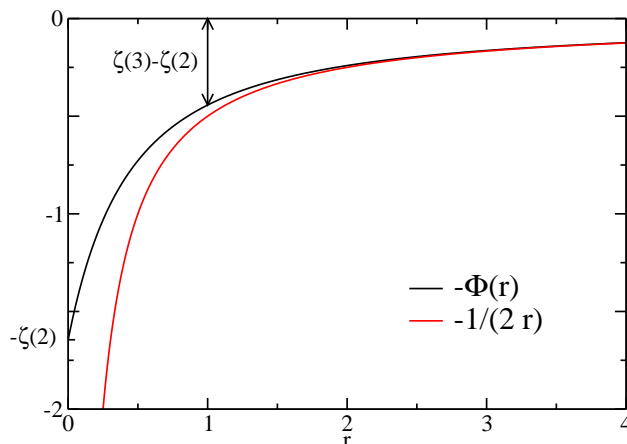
Figure 2.3: Comparison of the Coulomb interaction with the non-linear part of the internal energy. Whereas the Coulomb interaction diverges for $r \to 0$, $\Phi(0) = \zeta(2)$.

picture [see Fig. 2.1(d)]. The first few terms of the series expansion of the non-linear part of the internal energy,

$$\Phi(l) \approx \frac{1}{2l} - \frac{1}{12}\left(\frac{1}{l}\right)^3 + \frac{1}{20}\left(\frac{1}{l}\right)^5 - \mathcal{O}\left[\left(\frac{1}{l}\right)^7\right], \qquad (2.24)$$

show that for large chain lengths l the non-linear part is proportional to $1/l$, i.e., Coulombic. Thus, we replace all segments by charges at their beginnings and their ends according to their orientations. As each segment carries two charges, the indices of the charges are given by $2i - 1$ for the charge at the beginning and $2i$ for the charge at the ends of segment i. The charge at the beginning of segment i is $q_{2i-1} = -s_i$ and the charge at the end is $q_{2i} = s_i$. The coordinates of these charges are $z_{2i-1} = x_i$ and $z_{2i} = x_i + l_i$. The interaction potential of two charges q_m and q_n separated by a distance $z_{mn} = |z_n - z_m|$ is given by $\Phi_c(z_{mn}) = q_m q_n \Phi(z_{mn})$. This interaction is Coulombic in character for large distances and we can rewrite this interaction as

$$\epsilon \Phi_c(z_{mn}) \approx \epsilon \frac{q_m q_n}{2z_{mn}} = \frac{1}{4\pi\varepsilon_0} \frac{Q_m Q_n}{z_{mn} a}, \qquad (2.25)$$

with the magnitude of the charges then given by $|Q_m| = p/a$. Figure 2.3 shows a comparison of this Coulomb-like interaction, $\Phi(r)$, with the Coulomb interaction $1/r$. The main difference is that for a distance $r \to 0$ the Coulomb-like interaction converges to a finite value, $\Phi(0) = \zeta(2)$, whereas the Coulomb interaction diverges to $-\infty$. Note that for all possible distances $z_{mn} \geq 1$ the difference is small.

Rearranging the Hamiltonian in the segment picture given by Eq. (2.20) we obtain the Hamiltonian in the *charge picture* as

$$
H \;=\; \sum_{m=1}^{2n_{\mathrm{s}}-1} \sum_{n=m+1}^{2n_{\mathrm{s}}} q_m q_n \Phi(z_{mn}) +
$$
$$
+ n_{\mathrm{d}} c_{\mathrm{d}} + n_{\mathrm{c}} c_{\mathrm{c}} + nc \,. \tag{2.26}
$$

The sum in Eq. (2.26) includes the interaction of the charges belonging to the same defect. Using Eq. (2.12) and $E(1) = 0$ we obtain $\Phi(1) = \zeta(2) - \zeta(3)$ for this interaction, which occurs n_{d} times in the above Hamiltonian. Introducing the defect excitation energy, i.e., the energy (the free energy in the molecular model) needed to introduce a single defect in an infinitely long chain,

$$
E_{\mathcal{D}} = c_{\mathrm{d}} - \phi(1) = 2\zeta(2) - 2 \tag{2.27}
$$

we can write the Hamiltonian in the charge picture as

$$
H \;=\; \sum_{m=1}^{2n_{\mathrm{s}}-1} \sum_{n=m+1}^{2n_{\mathrm{s}}}{}' q_m q_n \Phi(z_{mn}) +
$$
$$
+ n_{\mathrm{d}} E_{\mathcal{D}} + n_{\mathrm{c}} c_{\mathrm{c}} + nc \,. \tag{2.28}
$$

where the prime indicates that the sum does not include the interactions between two charges belonging to the same defect. The coefficient c_{c} corresponds to the energy needed to break an infinitely long chain, and move the resulting fragments infinitely far apart from each other. The coefficient c is the energy required to add a single dipole to an infinitely long chain. The Hamiltonian in the charge picture depends on the charge positions, z_j, the number of particles n, the number of chains n_{c}, and the number of defects n_{d}. We note that these quantities are not sufficient to specify a configuration of the dipole model unambiguously.

The Hamiltonian in the charge picture [Eq. (2.28)] highlights the Coulomb-like effective interactions of defects and chain ends. L- and D- defects attract each other Coulombically whereas defects of the same kind repel each other. Defects next to a chain end are always attracted by the charge at this end.

2.3   Approximate representations

If the distances between charges are large we should be able to neglect their Coulomb-like interactions that decay as $1/r$. Then, only the linear terms of

Eq. (2.28) remain. The Hamiltonian in this simplest approximation, which we refer to as the no-charge-approximation (NCA), is given by

$$\mathcal{H}_0 = nc + n_c c_c + n_d E_\mathcal{D}. \qquad (2.29)$$

For small distances between effective charges, the Coulomb interaction is strong and cannot be neglected. This is the case for short chains and segments which carry charges at their ends. In particular, chains and segments of length one are represented by two charges of opposite sign which are separated by one lattice constant only. At the next higher level of approximation, we add the interaction energy $-\Phi(1) = -\zeta(2) + \zeta(3)$ between the charge pairs associated with each of the n_I segments of length one. The resulting Hamiltonian is

$$\mathcal{H}_1 = nc + n_c c_c + n_d E_\mathcal{D} + n_I[-\zeta(2) + \zeta(3)]. \qquad (2.30)$$

We will refer to this Hamiltonian as the singlet-charge-approximation (SCA), since we include the interaction of charge pairs associated with single dipoles.

The NCA and SCA do not depend on the lengths, positions, or orientations of the segments. States specified by the particle number n and $\mathbf{n}_0 = \{n_c, n_d\}$ for the NCA, and by n and $\mathbf{n}_1 = \{n_c, n_d, n_I\}$ for the SCA are thus degenerate. Calculating the degeneracy of these states requires to count the number of states for these approximations as a function of these variables. For the NCA, the number of states, $\Gamma_0(N, n, \mathbf{n}_0)$, is given by

$$\Gamma_0 \;=\; 2^{n_c} \binom{n - n_d - 1}{n_s - 1} \binom{n_s - 1}{n_c - 1} \binom{N + 1 - n}{n_c} \qquad (2.31)$$

with the number of segments, $n_s = n_c + n_d$, being a function of the defect number and the chain number. For the SCA the number of states, $\Gamma_1(N, n, \mathbf{n}_1)$, is given by

$$\Gamma_1 \;=\; 2^{n_c} \binom{n - 2n_s + n_c - 1}{n_s - n_I - 1} \binom{n_s}{n_I} \binom{n_s - 1}{n_c - 1} \binom{N + 1 - n}{n_c} \qquad (2.32)$$

for $n > 0$. If $n_s = n_c = n$ then $\Gamma_0 = \Gamma_1 = 2^n \binom{N+1-n}{n}$. For a derivation of these equations, see App. A.

2.4 Proton defects

Up to now we have only considered chains of intact water molecules. If an excess proton is introduced into the system, it forms a hydronium ion consisting of one oxygen atom and three hydrogen atoms. In a single-file

chain, this hydronium ion donates two hydrogen bonds without accepting any. Thus, structurally, the hydronium ion corresponds to an L-defect with an additional proton [23]. In the charge picture, the effective interaction of this protonated L-defect is given by the sum of the effective interaction of a regular L-defect and the effective interaction of the proton with defects and chain ends.

In Ref. [23] an approximate expression for this effective interaction was derived. For completeness we show next how the effective interaction of an additional proton located on an L-defect is included in the charge picture. In the dipole model the interaction of a proton located on an L-defect at site i and a dipole with direction $\sigma_j = \pm 1$ at site j is given by

$$W_{ij} = \frac{1}{4\pi\varepsilon_0} \frac{\sigma_j pe(j-i)}{a^2 |j-i|^3} = \epsilon' \frac{\sigma_j (j-i)}{|j-i|^3} \,, \tag{2.33}$$

where e is the elementary charge and $\epsilon' = \epsilon ae/(2p)$ the unit of the energy for the rest of this subsection.

Following the same approach as in the derivation of the segment and the charge picture, we calculate the interaction energy of a proton and an ordered segment with l dipoles of relative orientation $s = \sigma_j(j-i)/|j-i|$ with respect to the position of the proton, i.e., $s = 1$ ($s = -1$) for dipoles pointing away (towards) the proton. Let us assume the proton is located at the site with index zero, the first dipole of the segment is located at j_1, and the last at $j_2 = j_1 + l - 1$. Using the polygamma function, we obtain

$$
\begin{aligned}
W(j_1, l) &= \sum_{j=j_1}^{j_2} W_{ij} = s \sum_{j=j_1}^{j_2} j^{-2} = \\
&= s \sum_{j=j_1}^{\infty} j^{-2} - s \sum_{j=j_2+1}^{\infty} j^{-2} = \\
&= s \left[-\Psi'(j_1) + \Psi'(j_1 + l) \right]
\end{aligned}
\tag{2.34}
$$

for the interaction energy of the proton with the segment. In the charge picture, the charges are located at the beginnings and ends of segments, i.e., between dipoles, whereas the above expression depends on the positions of the first and the last dipole of the segment. To be consistent with the charge picture, we rewrite this interaction energy as a function of the distance $x = j_1 - 1/2$ from the proton to the beginning of the segment,

$$
\begin{aligned}
W(x, l) &= s \left[-\Psi'(x + 1/2) + \Psi'(x + l + 1/2) \right] = \\
&= s \left[\bar{\Phi}(x) + \bar{\Phi}(x + l) \right],
\end{aligned}
\tag{2.35}
$$

where $x + l$ is the end of the segment. The Coulomb-like interaction $\bar{\bar{\Phi}}(x)$ is given by

$$\bar{\Phi}(x) = \Psi'\left(x + \frac{1}{2}\right) \approx \frac{1}{x} - \frac{1}{12}\left(\frac{1}{x}\right)^3 + \mathcal{O}\left(x^{-5}\right) . \tag{2.36}$$

Thus, the interaction energy of a proton with the dipoles of a segment is equal to a Coulomb-like interaction of the proton with charges at the beginning and the end of the segment. For a protonated L-defect in an infinitely long chain we obtain a proton energy of $E_{\mathrm{p}} = -2\zeta(2)$, stemming from the two charges next to the defect.

For large distances, the interaction energy of a hydronium ion with a defect can be written as

$$\Phi_{\mathrm{PL}}(z) = \frac{1}{4\pi\varepsilon_0}\frac{\mp Q}{az}\left(e - Q\right) , \tag{2.37}$$

where $Q = 2p/a$ is the magnitude of the total effective charge of a defect. The plus sign is valid for the interaction with a D-defect and the minus sign for that with an L-defect. Since the proton charge is larger than Q, a hydronium ion is repelled by D-defects and attracted to L-defects, in agreement with Ref. [23]. Also, the hydronium is repelled by the endpoints of an otherwise ordered water chain. As a consequence, the preferred position of an excess proton in an isolated water wire is at the chain center.

2.5 Monte Carlo simulation

Next, we examine the thermodynamic behavior of water in nanopores in contact with a heat bath and a particle reservoir. Thus, we perform canonical and grand-canonical Monte Carlo simulations of the dipole model.

For the Monte Carlo simulations of the dipole model, we describe configurations in the segment picture and include gaps of unoccupied sites as segments with $s = 0$. Thus, a configuration consists of occupied sections (segments) and empty sections (gaps). (In the following we use the term "segments" only for segments of chains and the term "section" for segments of chains and empty gaps.) Between segments one finds either a defect or an empty section. The boundary conditions are given by two empty gaps at the beginning and the end of the lattice (see App. A). A configuration is unambiguously defined by the beginning x_i, the length l_i, and the value of s_i for each section i. Defects are located between next neighbor sections with $s \neq 0$. Including the empty end sections, there are $n_0 = n_{\mathrm{c}} + 1$ sections with $s = 0$ corresponding to gaps.

With a configuration given by $\mathcal{C}_i = \{\{x_j, l_j, s_j\} : 1 \leq j \leq n_{\mathrm{s}} + n_0\}$ the canonical partition function can be written as

$$Z_N(\beta, n) = \sum_{\{\mathcal{C}_i\}} e^{-\beta H(\mathcal{C}_i)} \,. \tag{2.38}$$

The grand canonical partition function is given by

$$\Xi_N(\beta, z) = 1 + \sum_{n=1}^{\infty} Z_N(\beta, n) z^n \,. \tag{2.39}$$

The fugacity is defined as $z = e^{\beta\mu}$, where μ is the chemical potential and $\beta = 1/(k_{\mathrm{B}}T)$ the reciprocal temperature with k_{B} being Boltzmann's constant.

To enhance the sampling, we use non-local Monte Carlo moves. Monte Carlo simulations with only local moves, in which individual dipoles are flipped, are inefficient for large systems. Here, we apply efficient non-local trial moves with asymmetric generation probabilities for which we have to correct in the acceptance probability. These trial moves change the lengths of sections and their orientations for the generation and recombination of defects, for the displacement of defects and chains, and for the insertion and deletion of particles. For details see App. B.1.

We also perform Monte Carlo simulations for the NCA and SCA for which the canonical partition functions are given by

$$\mathcal{Z}_{\mathrm{N}}^{(i)}(n) = \sum_{\{\mathcal{C}_j\}} e^{-\beta \mathcal{H}_i(n, \mathbf{n}_i)} \tag{2.40}$$

with $i = 0$ for the NCA and $i = 1$ for the SCA, and $\mathbf{n}_i$ implicitly depending on the configurations $\mathcal{C}_j$. Using the degeneracies given by Eqs. (2.31) and (2.32), Eq. (2.40) can be rewritten as

$$\mathcal{Z}_{\mathrm{N}}^{(i)}(n) = \sum_{\mathbf{n}_i} \Gamma_i(N, n, \mathbf{n}_i) e^{-\beta \mathcal{H}_i(n, \mathbf{n}_i)} \,, \tag{2.41}$$

which permits us to formulate new effective Hamiltonians

$$\mathcal{H}_i' = \mathcal{H}_i - T \ln \Gamma_i(N, n, \mathbf{n}_i) \,, \tag{2.42}$$

with canonical partition functions given by

$$\mathcal{Z}_{\mathrm{N}}^{(i)}(n) = \sum_{\mathbf{n}_i} e^{-\beta \mathcal{H}_i'(n, \mathbf{n}_i)} \,. \tag{2.43}$$

We can calculate these partition functions either numerically by direct summation or perform Monte Carlo simulations in the space of $\mathbf{n}_0 = \{n_{\mathrm{c}}, n_{\mathrm{d}}\}$

for the NCA and of $\mathbf{n}_1 = \{n_c, n_d, n_I\}$ for the SCA. The applied trial moves simply increase or decrease the values of the variables of the Hamiltonian within the limits of the phase space given in App. A.

To study the system behavior over a broad range of the chemical potential we use the Wang-Landau algorithm [49, 50] with the particle number as order parameter to find a bias function $w(n)$ corresponding to the negative free energy as a function of the particle number. We use this function for a biased simulation [51] at the fugacity z, resulting in a flat histogram of the particle number, with the Hamiltonian in the biased system given by

$$H' = H - Tw(n)\ln z \, . \tag{2.44}$$

The output are samples of the total energy, chain number, defect number, number of particles, and total dipole moment, $\{E^{(i)}, n_c^{(i)}, n_d^{(i)}, n^{(i)}, D^{(i)}\}$. By unfolding the bias function $w(n)$ and reweighting [51], we obtain estimates for observables that are functions of the above quantities (see App. B.2).

Chapter 3

Water in narrow carbon nanotubes

3.1 Introduction

Equipped with the dipole lattice model derived in the last chapter, we now study water in narrow carbon nanotubes from nanoscopic to macroscopic tube lengths. We parameterize the model with results of detailed molecular simulations and briefly discuss their physical meanings. With this set of parameters we validate our model concerning the particle number and its fluctuations, the free energy of defect generation, and the dipolar order properties of short tubes.

A key factor for the unique properties of 1D-confined water is the nearly perfect molecular order, both translationally and orientationally, with uninterrupted chains of water molecules whose dipoles collectively point either "up" or "down" along the pores [16, 52]. Here, we show that dipolar order persists for water chains in pores up to macroscopic lengths. We quantify the statistics of translational and orientational defects in filled pores, and the particle number fluctuations associated with the first-order like filling/emptying transition.

As we have seen in Chapter 2, the charge picture lends itself to approximations in which the long-range interactions of the effective charges are neglected and which allow the investigation of the role of the Coulomb-like interactions. In these approximations the filling of the tube is reproduced correctly, but the defect number at the filling transition is not. For small system sizes, the particle number distribution function is bimodal with peaks at low and high densities and is captured nicely by the approximations. However, we find that neglecting Coulomb-like interactions qualitatively alters

the form of the low density peak. We quantify the bimodal behavior with respect to the tube length and the chemical potential.

As we shall see, long and completely filled tubes are well described by a system of uncorrelated defects and uncorrelated defect pairs. The latter consist of an L- and a D-defect separated by a single molecule and they essentially lead to a degeneracy of the disordered states with respect to the ordered states. Exploiting the isomorphism of a system of uncorrelated defects to the one-dimensional Ising model, we derive analytical results for the free energy as a function of the total dipole moment, and find them in good agreement with simulation results.

3.2   Parameterization and validation

The parameters of the dipole model are determined by matching its properties to those of a molecular model of water inside a pore. We perform fully-atomistic Monte Carlo simulations of a (6,6)-type carbon nanotube [14, 16], filled with up to 100 molecules. We used the TIP3P potential [53] for the water-water interactions, and the carbon-water potential as in Ref. [16]. To minimize boundary effects, the tubes are considerably longer than the water chain. Moreover, the lattice calculations are performed for equivalent free boundary conditions. The lattice spacing of the dipole model is given by the average distance along the tube axis of neighboring water molecules in a hydrogen bonded chain, $a = 0.265$ nm. The dipole strength of the model is determined by the average dipole moment of water molecules in an "up" orientation projected onto the tube axis, $\mu = 1.9975$ Debye. Using these values for a and μ, we obtain an energy constant of $\epsilon = 2\mu^2/(4\pi\varepsilon_0 a^3) = 25.8236$ kJ/mol, such that $\beta\epsilon = 10.42$ at $T = 298$ K. And finally, the contact energy $E_c = -20.8$ kJ/mol is obtained as the average interaction energy of two neighboring water molecules.

To perform grand canonical simulations of the dipole model, we have to determine the effective tube-water interaction. Since it couples to the particle number we can absorb it in the chemical potential. We also need the entropic contribution which couples to the number of chains. We determine both quantities by comparing the transfer free energy of the molecular and the dipole model and tuning the fugacity and the entropic contribution to obtain agreement between these two models. The transfer free energy, given by $\beta A(n) = -\ln[P(n)/P(0)]$, where $P(n)$ is the particle distribution function, is the free energy needed to put n water molecules in a tube of length L at the inverse temperature β. We obtain for a tube of length $L = 30a$ in contact with a heat bath and a particle reservoir at ambient conditions, i.e. , at
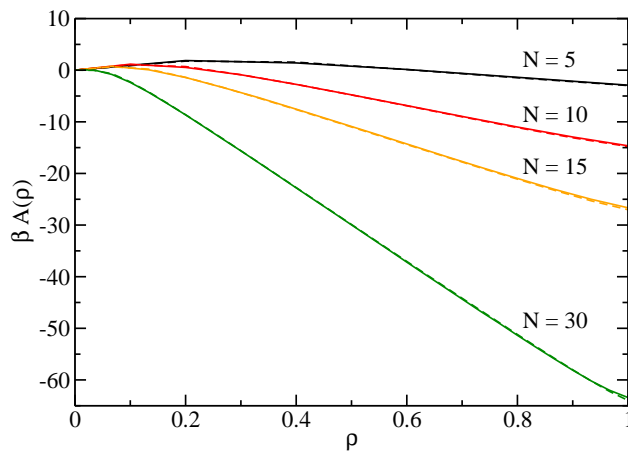
Figure 3.1: The transfer free energy as a function of the density for different system sizes for the molecular model (solid lines) and the dipole model (dashed lines). The excellent agreement renders the curves for the different models nearly indistinguishable.

room temperature and atmospheric pressure, a fugacity $z_0 = 0.000327$ and an entropic contribution $\beta S_c = -3.96$.

Figure 3.1 shows a comparison of the transfer free energy of the molecular and the dipole model for system sizes $N = 5, 10, 15$, and $N = 30$ as a function of the density $\varrho = \langle n \rangle / N$. Since the dipole model is a coarse-grained description of the molecular model, all states in the molecular model with an occupation number equal or larger than the number of sites contribute to the completely filled state, i.e., to $P(N)$. The agreement is excellent as the curves for the molecular and the dipole model lie practically on top of each other. We observe that for small sizes the system shows two minima, one for the empty and one for the filled state. Thus, the particle distribution function is bimodal, i.e., has two peaks (see Sec. 3.3.3). With increasing system size the minimum corresponding to the filled state deepens and the minimum corresponding to the empty state vanishes.

By reweighting the particle distribution functions corresponding to the transfer free energies shown in Fig. 3.1, we obtain the adsorption isotherms and the relative particle number fluctuations as a function of the relative fugacity (Figs. 3.2 and 3.3). The relative fugacity is the actual fugacity divided by the fugacity of a system in contact with a heat and particle reservoir at room temperature and atmospheric pressure. For low fugacities the relative fugacity is equal to the relative humidity. For larger system sizes the density shown in Fig. 3.2 present a steeper increase at the filling
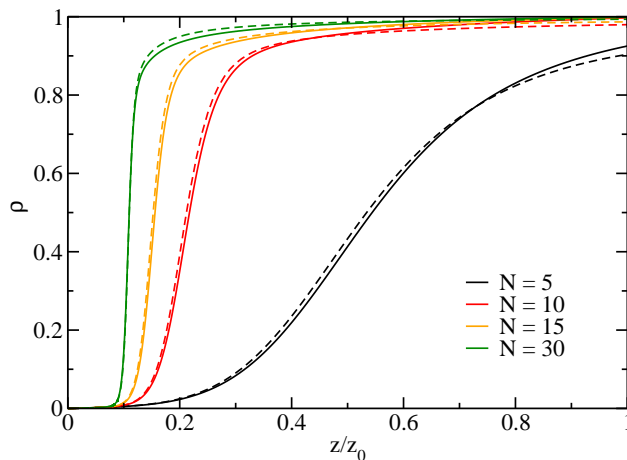
Figure 3.2: The particle density as a function of the relative fugacity. The solid lines are results from molecular simulations and the dashed lines are results for the dipole model.

transition, which moves to smaller fugacities.

The relative variance, i.e., the variance of the particle number divided by the average particle number, is a measure for the fluctuations of the particle number. For macroscopic volumes, the relative variance is related to the isothermal compressibility κ_T via $(\langle n^2 \rangle - \langle n \rangle^2)/\langle n \rangle = \rho k_B T \kappa_T$, where ρ is the particle density, k_B Boltzmann's constant, T the temperature, and angle brackets indicate the canonical ensemble average. The relative variance (Fig. 3.3) has a maximum at the filling transition. The fluctuations become larger with increasing system size. The properties of the filling transition for increasing system size are discussed in detail in the Sec. 3.3.2.

A similar argument can be used to justify the entropic contribution of defect molecules. The L-defect molecule, which donates two hydrogen bonds, is constrained more strongly than the D-defect, which accepts two hydrogen bonds. A chain with a single defect consists either of an L-defect and two end molecules that accept a single hydrogen bond or a D-defect with end molecules that donate a single hydrogen bond. Thus, the more strongly constrained L-defects always exist with end molecules that move more freely, with the opposite holding for D-defects. As an approximation we assume that the different contributions to the phase space volume of defect molecules and end molecules compensate each other. This argument can be easily extended for chains with more than one defect. As a consequence, we only have to account for the larger freedom of the chain ends and do not treat
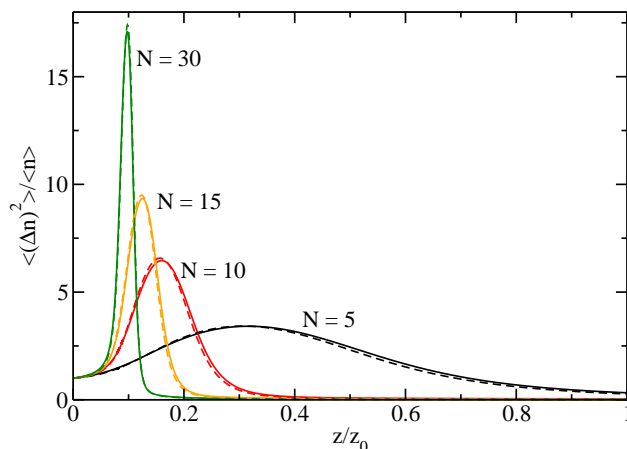
Figure 3.3: Particle number fluctuations as a function of the relative fugacity for different system sizes. The solid lines are results from molecular simulations and the dashed lines are results for the dipole model.

the defect molecules explicitly. It therefore suffices to add the entropic contribution S_c for each chain in the system.

The excellent agreement of the dipole model and the molecular model for different system sizes supports the validity of the entropic contribution. It accounts for the different contributions to the phase space volume of water molecules according to the number of their dangling OH bonds. In an ordered chain all molecules donate a single hydrogen bond except one at one end. In contrast to all other molecules of the chain which have a single dangling OH bond, this molecule has two. Thus, it has more freedom to move and a higher contribution to the entropy of the chain than the other molecules. If we generate an L-defect, which donates two hydrogen bonds without accepting any, both molecules at the chain ends have two dangling OH, thus conserving the number of dangling OH bonds. The situation for the D-defect is similar and thus the number of dangling OH bonds is conserved for any number of L- and D-defects within the chain. Only if a hydrogen bond is broken/formed, the number of dangling OH bonds is increased/decreased by one.

Since the entropic contribution accounts for the difference in the phase space contributions of a dangling OH bond and one that donates a hydrogen bond, we can obtain an estimate for the entropic contribution from simple geometric considerations. We assume that an OH bond of a water molecule within a segment that donates a hydrogen bond is restricted to a spherical cap with an opening angle α. For a hydrogen bond of a water molecule at

α	10°	20°	30°	40°
$\Delta S/k_{\mathrm{B}}$	4.88	3.50	2.70	2.15

Table 3.1: Estimates for the entropic contribution.

the chain end that accepts a single bond, this cap is about half a sphere. The ratio of these areas gives us an estimate for the difference of the contributions to the entropy of these two water molecules. The surface area of a spherical cap with opening angle α of a sphere with radius r is given by $A = 2\pi r^2(1 - \cos\alpha)$. The difference in the entropies between a dangling OH bond and a hydrogen bonded OH bond is given by

$$\frac{\Delta S}{k_{\mathrm{B}}} = \ln\left(\frac{4\pi r^2}{A}\right) = \ln\left(\frac{2}{1 - \cos\alpha}\right).$$ (3.1)

The entropic contribution is an energy in our effective Hamiltonian and is related to the entropy difference by $\beta S_{\mathrm{c}} = -\Delta S/k_{\mathrm{B}}$. Table 3.1 shows results for different opening angles α which are indeed of the order of the entropic contribution, $\beta S_{\mathrm{c}} = -3.96$.

Dipole ordering and defect creation

To verify the accuracy of the dipole model with respect to the free energies of dipole ordering and defect creation we performed Monte Carlo simulations of a completely filled tube for both the molecular system and the dipole model and calculated free energy profiles as a function of the reduced total dipole moment per site, $F(D/N)$. Here, $D = M/\mu$, where M is the total dipole moment. The results of these calculations are depicted in Fig. 3.4 for system sizes of $N = 10, 20, 40$, and 100 molecules. For a better comparison of the discrete dipole model with the continuous molecular system we coarse grained the probability distribution function of the dipole model using a bin size of 2μ. This particular value corresponds to the change in the magnitude of the total dipole moment when a defect hops from one site to the next. As is evident from the free energy profiles shown in Fig. 3.4, the agreement between the TIP3P system and the dipole model curves is excellent, both qualitatively and quantitatively. Essentially, the only difference noticeable in the plots is that, as expected, the dipole model lacks the small scale fluctuations of D about the two dipole ordered states observed in the continuous molecular system.

The insets of Fig. 3.4 show the free energy $\beta F = -\ln P(|D| < D_0)$ configurations in which the magnitude $|D|$ of the total dipole moment is less
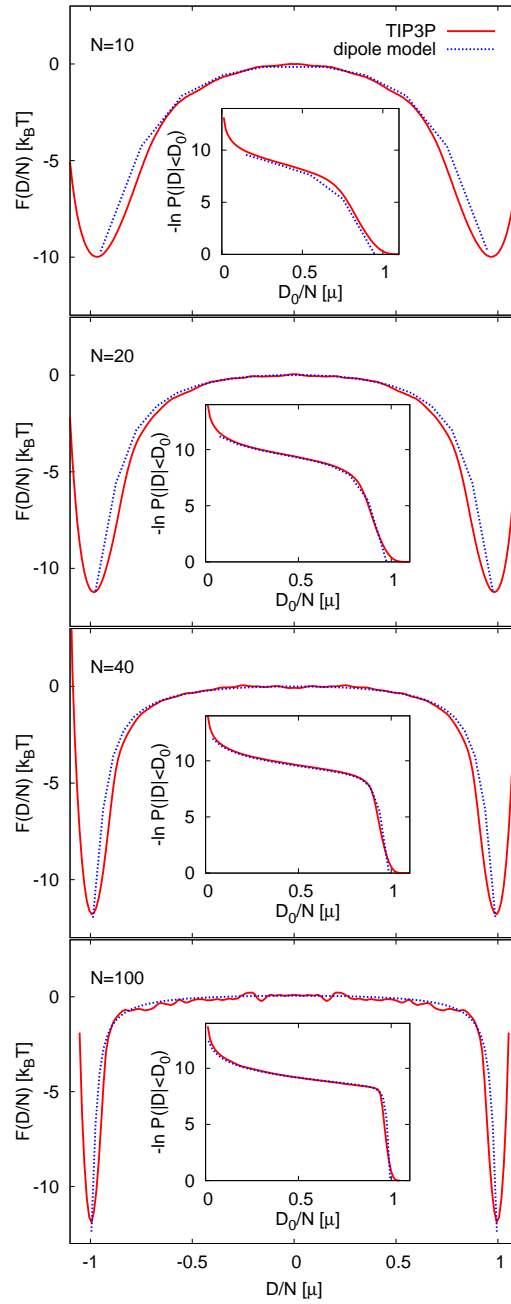
Figure 3.4: Free energy $F(D/N)$ as a function of the dipole moment per site for system sizes $N = 10, 20, 40, 100$ (from top to bottom) of the molecular system (solid lines) and the dipole model (dotted lines). The insets show the free energy $\beta F = -\ln P(|D| < D_0)$ of configurations with a total dipole moment magnitude $|D| < D_0$.
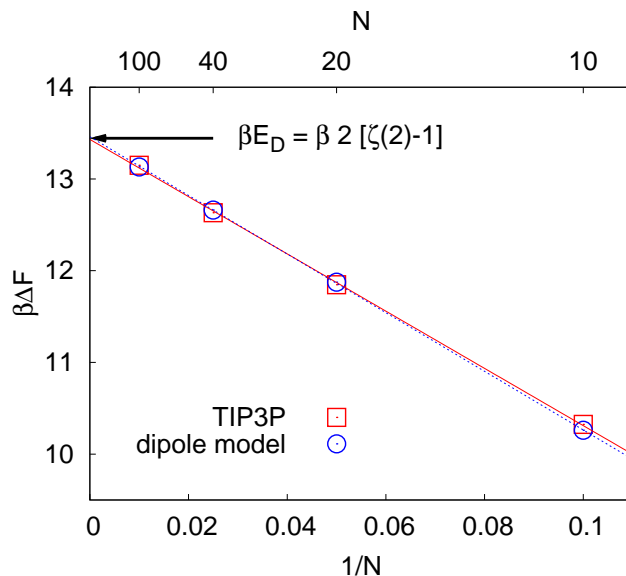
Figure 3.5: Free energy for creating a single defect at the center of a water chain. Shown is the free energy difference between configurations with a defect at the center and configurations without a defect (ordered states) as a function of the inverse system size $1/N$. The squares are results of Monte Carlo simulations using the TIP3P atomistic water model and the circles are results of Monte Carlo simulations of the dipole model. Lines are linear fits to the two data sets. The dipole model and the molecular system are in excellent agreement. For large system sizes, i.e., for $1/N \to 0$, the free energy ΔF converges to the defect excitation energy $\beta E_{\mathcal{D}} = \beta 2[\zeta(2) - 1]$ with exactly the slope expected from the theory (see Tab. 3.2).

than D_0. Since the probability of finding the total dipole moment within such an interval is an integral over the corresponding probability density function, $P(|D| < D_0) = \int_{-D_0}^{D_0} P(D)\mathrm{d}D$, this comparison of free energies is unaffected by discretization. Again, excellent agreement is observed.

For the conditions and the system sizes studied above, states with $D \approx 0$ have exactly one defect at the center of the water chain. Thus, the free energies as a function of the dipole moment as shown in Fig. 3.4 can be used to estimate the excitation energy of a single defect, $E_{\mathcal{D}}$. To do so, we calculate the free energy difference, ΔF, between all ordered configurations (all "up" and all "down") and all configurations with a single defect at the center (L or D defect). In the continuous molecular system, a single defect at the center of the chain corresponds to all configurations with $|D| < 1$, and the ordered states to all configurations with $|D| > N - 2$. Accordingly,

the free energy difference, ΔF is then given by

$$\beta \Delta F = -\ln \frac{P(|D| < 1)}{P(|D| > N - 2)} \,. \tag{3.2}$$

In the dipole model, this free energy difference is equivalent to the difference ΔE in the configurational energies of the perfectly ordered configurations and the configurations with a defect at the center. (There are exactly two energetically equal ordered states and two energetically equal states with a defect at the center). It follows from the total energy expressed in the charge picture that

$$\Delta E = 2 \left[\Phi\left(N\right) - \Phi\left(\frac{N-1}{2}\right) - \Phi\left(\frac{N+1}{2}\right) \right] + E_{\mathcal{D}} \,, \tag{3.3}$$

where the defect excitation energy is given by $E_{\mathcal{D}} = 2[\zeta(2) - 1]$ and $\zeta(m)$ is Riemann's zeta-function. In the above equation, the term $\Phi(N)$ originates from the interaction of the two charges located at the endpoints of the water chain. The terms $\Phi([N-1]/2)$ and $\Phi([N+1]/2)$ stem from the interaction of the two defect charges with the charges at the end points. Since the long-range interaction converges rapidly to the Coulomb interaction, i.e., $\Phi(x) = 1/(2x) - \mathcal{O}(x^{-3})$, the energy difference can be approximated by

$$\Delta E \approx -\frac{3}{N} + E_{\mathcal{D}} \,. \tag{3.4}$$

This is a linear function of the inverse system size, $1/N$, with a slope of $k = -3$. In the limit of infinite system size, i.e., for $1/N \to 0$, the energy difference converges to the defect excitation energy $E_{\mathcal{D}}$.

The free energy differences obtained from these calculations are shown in Fig. 3.5 as a function of $1/N$ for the molecular system and the dipole model. Also shown are linear fits to the data. To improve the statistical accuracy of the free energies for the molecular system, we used the property that the free energy curves are flat for $D \approx 0$ (see Fig. 3.4) and estimate the probability $P(|D| < 1)$ as $P(|D| < 1) \approx P(|D| < N/10)/(N/10)$. The results for both models are in excellent agreement with each other, and also

	analytical	TIP3P	dipole model
βk	-31.27	-31.21	-31.96
$\beta E_{\mathcal{D}}$	13.44	13.43	13.46

Table 3.2: Analytical results and estimates from linear fits as shown in Fig. 3.5 for the slope k and the defect excitation energy $E_{\mathcal{D}}$.
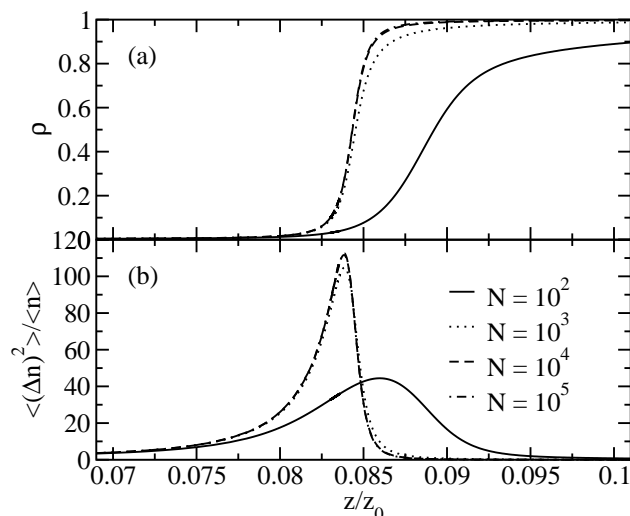
Figure 3.6: Filling/emptying transition. (a) Adsorption isotherms: particle density $\rho = \langle n \rangle / N$, as a function of the relative fugacity, z/z_0, for different system sizes. The filling transition occurs at about eight percent of the fugacity at ambient conditions. The adsorption isotherms become steeper with increasing system size. At $N = 10^4$ the adsorption isotherms have reached their large system limit. (b) Relative variance of the particle number fluctuations, $\langle (\Delta n)^2 \rangle / \langle n \rangle = (\langle n^2 \rangle - \langle n \rangle^2)/\langle n \rangle$, as a function of the relative fugacity, z/z_0, for different system sizes.

with the analytical prediction as shown in Tab. 3.2. In this table, numerical results for the slope and the defect excitation energy derived from a linear fit for both models are compared to the analytical result.

3.3 Tube filling/emptying

3.3.1 Overview

To probe the emptying/filling transition, we have determined the adsorption isotherms (i.e., the average particle density) as a function of the fugacity z relative to the fugacity at ambient conditions, z_0, for different system sizes [see Fig. 3.6(a)]. The transition from an empty to a full tube occurs in a narrow fugacity range around $z/z_0 \approx 0.084$, corresponding to ~ 8.4 % relative humidity at ambient conditions. The adsorption isotherm becomes steeper with increasing system size but remains continuous even in the thermodynamic limit, as is required by the impossibility of a true first-order phase transition.
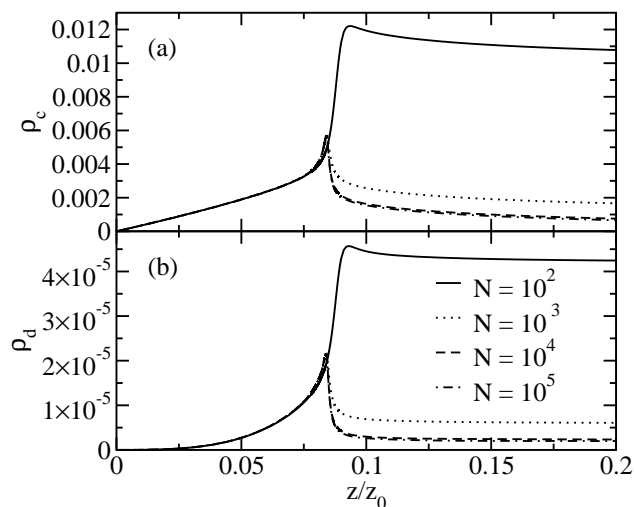
Figure 3.7: Water-chain fragmentation. (a) Fragment density, $\rho_{\mathrm{c}} = \langle n_{\mathrm{c}} \rangle / N$, as a function of the relative fugacity, z/z_0, for different system sizes. The average number of fragments $\langle n_{\mathrm{c}} \rangle$ has a maximum at the filling transition. (b) Hydrogen bonding defect density, $\rho_{\mathrm{d}} = \langle n_{\mathrm{d}} \rangle / N$, as a function of the relative fugacity, z/z_0, for different system sizes.

Corresponding behavior is observed in the relative variance of the particle number, n, as shown in Fig. 3.6(b). For macroscopic volumes, the relative particle number fluctuations are related to the isothermal compressibility κ_{T} via $(\langle n^2 \rangle - \langle n \rangle^2)/\langle n \rangle = \rho k_{\mathrm{B}} T \kappa_{\mathrm{T}}$, where ρ is the particle density and angle brackets indicate the ensemble average. The relative variance is peaked at the filling transition. Even though the peak height initially grows with increasing system size, it eventually converges to a finite value. We find that both the adsorption isotherms and the relative variance are nearly converged to their thermodynamic limits for a system size of 10^4 sites.

We conclude that at ambient temperature and relative humidity >10 % long pores are almost completely filled.

Water-Chain Fragmentation

As the water fugacity (relative humidity) is reduced and the tube begins to empty, an interesting coupling between hydrogen bonding defect formation and chain fragmentation is revealed. Both aspects are of considerable relevance in practical applications of 1D-confined water chains. In particular, for water-mediated proton transfer, e.g., in nanotube-based fuel-cell membranes, dipolar order and continuity of the water chains are both essential.

The formation and dynamics of hydrogen bonding defects in 1D water is a major factor for the break-up of long ordered chains into shorter segments. With the energetic cost of forming a defect at the end of a chain being lower than in the middle, defects facilitate chain fragmentation, and vice versa. Indeed, Figs. 3.7(a) and 3.7(b) show that the fragment and hydrogen bonding defect densities closely mirror each other when plotted as a function of the water fugacity. Here, fragments are defined as separate chains of hydrogen bonded molecules, or single molecules. We find that both the fragment density and the defect density are peaked at the filling transition. The peak in the fragment density reflects the entropic gain through fragmentation for low particle densities. For fugacities z below the filling transition, the average fragment number decays linearly towards zero. At low fugacity, the system behaves ideally with a particle density $\rho \approx 2z \exp(-\beta S_c)$, where S_c is the entropic contribution. The fragment number is then approximately equal to the number of particles, explaining the observed linear decay for small z. Moreover, with fragments too short to carry a defect, the average defect density ρ_d in Fig. 3.7(b) decays faster than linear with decreasing fugacity.

In essence, it is the entropic fragmentation that prevents a true phase transition in the thermodynamic limit [24] and destroys the dipolar order at the filling transition.

3.3.2   Drying/filling transition

The charge picture of the dipole lattice model gives direct physical insight into the microscopic properties of water in nanopores. The Coulomb-like interactions lead to an attraction between L- and D-defects and also to an attraction between a chain end and the defect next to it. So, the Coulomb interaction has clearly an important influence on these microscopic properties of water in nanopores. The question arises, what is the influence of the Coulomb-like interactions on the overall phase behavior? Or, in other words, which aspects of the system behavior are captured by the approximations that neglect Coulomb-like interactions (NCA and SCA)?

To clarify the role of the Coulomb-like interactions, we compare results derived in the SCA with results of the full Hamiltonian for the filling transition. We characterize the system by the particle density, $\rho = \langle n \rangle / N$, (Fig. 3.8), the particle fluctuations (relative variance, Fig. 3.9), the chain density $\rho_c = \langle n_c \rangle / N$, i.e., the number of chains per site, (Fig. 3.10), and the defect density $\rho_d = \langle n_d \rangle / N$, i.e., the number of defects per site (Fig. 3.11), as a function of the relative fugacity. The results for system sizes $N = 10^2$,

Figure 3.8: Particle density of (a) the full Hamiltonian and (b) the SCA. Circles denote SCA results for $N = 10^{10}$. The orange line shows results of the NCA for $N = 100$.

10^3, 10^4, and 10^5 sites are obtained by reweighting of biased sampling simulation data. Additionally, we show in Figs. 3.8 and 3.9 results for the SCA for $N = 10^{10}$ from Monte Carlo simulations at the corresponding fugacity values using the effective Hamiltonian of Eq. (2.42).

The adsorption isotherms (i.e., the average particle density) in Fig. 3.8 and the relative fluctuations of the particle number in Fig. 3.9 show that the results for the SCA are in excellent agreement with the results for the full Hamiltonian for the system sizes studied here. We find that both the adsorption isotherms and the relative variance are nearly converged to their thermodynamic limits for a system size of 10^4 sites which is supported by the results for the SCA for $N = 10^{10}$.

The adsorption isotherms become steeper with increasing system size but the slope remains finite even in the thermodynamic limit. The relative variance is peaked at the filling transition as shown in Fig. 3.9. Even though the peak height initially grows with increasing system size, it eventually converges to a finite value. This is in agreement with the impossibility of a true first-order phase transition in one dimension for $1/r^3$ interactions [24].

Figures 3.8 and 3.9 also show results for the NCA for a system size $N = 100$. The adsorption isotherms are in good agreement, but the relative
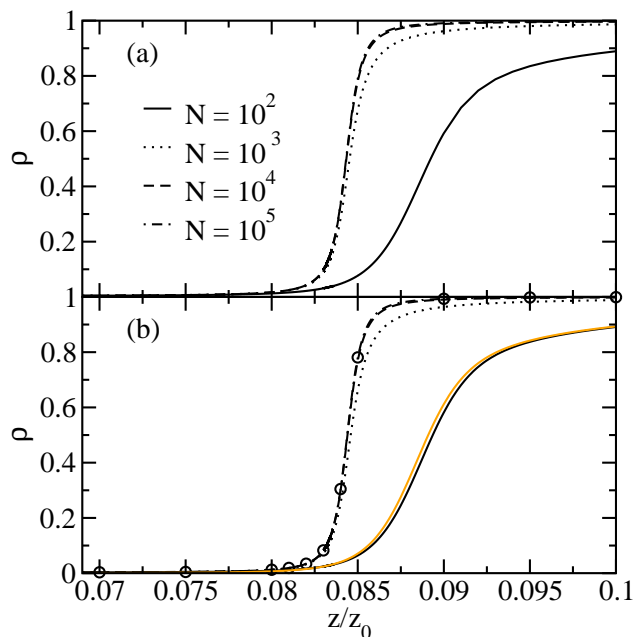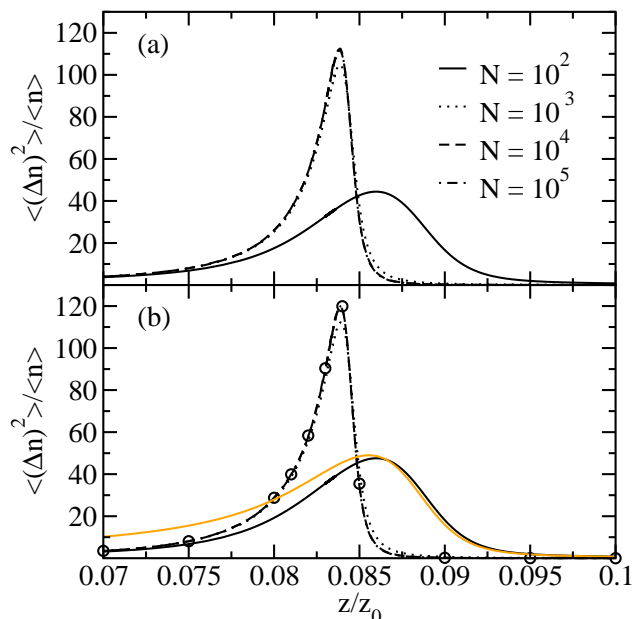
Figure 3.9: Relative variance of the particle number of (a) the full Hamiltonian and (b) the SCA. Circles denote SCA results for $N = 10^{10}$. The orange line shows results of the NCA for $N = 100$.

variance decays too slowly for fugacities below the filling transition compared to the results of the full Hamiltonian. The SCA reproduces the results of the full Hamiltonian well, as the system at low fugacities consists mainly of chains of length one, which are correctly described in the SCA.

Since the adsorption isotherms for the NCA and the full Hamiltonian are in good agreement we use this approximation to obtain an estimate for the chemical potential $\mu_{1/2}$, where the system is half full. Assuming that no defects exists, and that the number of particles is much larger than the number of chains, we obtain a Hamiltonian that only depends on the particle number,

$$\mathcal{H}' = nc - \mu n \,, \tag{3.5}$$

where we treat the chemical potential like a magnetic field in the Ising model and include it in the Hamiltonian. The n particles do not interact with each other but couple to the field $c - \mu$. The canonical partition function of this ideal lattice gas in an external field is given by $Z = (1 + e^{-\beta(c-\mu)})^N$. The density is obtained by $\langle n \rangle = -1/Z[\partial Z/\partial(\beta\mu)]$ which gives $\rho = \langle n \rangle/N = e^{-\beta(c-\mu)}/(1 + e^{-\beta(c-\mu)})$. If we demand that the system is half full, i.e. , the density is $\rho = 1/2$, then the energetic cost of inserting a particle into the

Figure 3.10: Chain density of (a) the full Hamiltonian and (b) the SCA. Circles denote SCA results for $N = 10^{10}$. The density of non-interacting particles is shown as straight line.

system is equaled by the chemical potential, $\mu = c$, which leads to

$$\mu_{1/2} = 1 + E_{\rm c} - \zeta(3) \,. \tag{3.6}$$

The corresponding relative fugacity $z_{1/2}/z_0 \approx 0.0841$ is in good agreement with the simulation result $z_{1/2}/z_0 \approx 0.084$, corresponding to 8.4% relative humidity. This result can also be derived for a lattice gas with dipole-dipole interactions and exploiting the isomorphism to the Ising model (see App. C).

Observables depending on the particle number are well reproduced in the SCA. We obtain insight into the structure of the system by looking at the chain and defect density as functions of the chemical potential. We find that at the filling transition both the chain density in Fig. 3.10 and the defect density in Fig. 3.11 are peaked. The peak in the chain density is also reproduced by the SCA although the curves are below the results of the full Hamiltonian. Thus, the peak in the fragment density reflects the entropic gain through fragmentation for low particle densities.

Figures 3.10 and 3.11 also show that for the full Hamiltonian the defect density roughly mirrors the fragment density. The reason is, that on the one hand a chain with a defect can lower its free energy by splitting the chain into two at the defect site. On the other hand, the generation of defects costs less
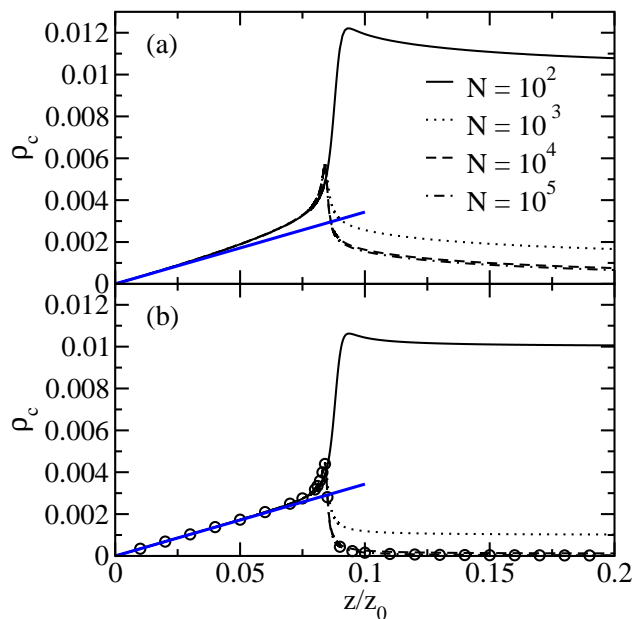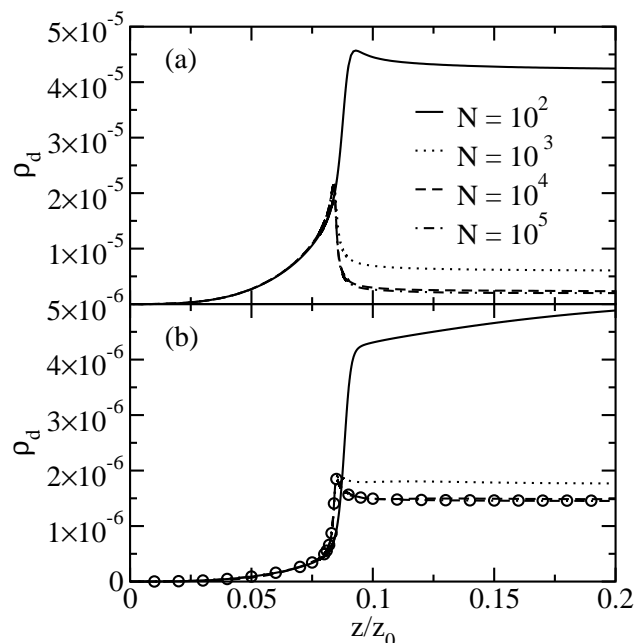
Figure 3.11: Defect density of (a) the full Hamiltonian and (b) the SCA. Circles denote SCA results for $N = 10^{10}$. Note the different scalings of the y-axes.

energy at the ends of water chains and the number of ends is proportional to the number of fragments. The latter is a consequence of the Coulomb-like attraction between the charge at the chain end and charges forming a defect next to this end. Thus, the results of the SCA only show a small peak in the defect density as the interaction of the two charges on the endpoints of segments of length one is included. These data do not reproduce the results of the full Hamiltonian at the filling transition quantitatively.

For fugacities z below the filling transition, the average fragment number decays approximately linearly with z towards zero. At low fugacity, the system behaves ideally. The grand-canonical partition function of ideal particles is given by $Z = \sum_n \binom{N}{n}(2ze^{-\beta S_c})^n$ which, for small fugacities, leads to a density $\rho \approx 2z \exp(-\beta S_c)$, where S_c is the entropic correction. The fragment number is then approximately equal to the number of particles, explaining the observed linear decay for small z. Moreover, with fragments too short to carry a defect, the average defect number decays even faster.

The increasing fragmentation while approaching the filling transition from high fugacities leads to a stronger decay of the orientational order. As a measure for the order we use the average of the squared total dipole mo-
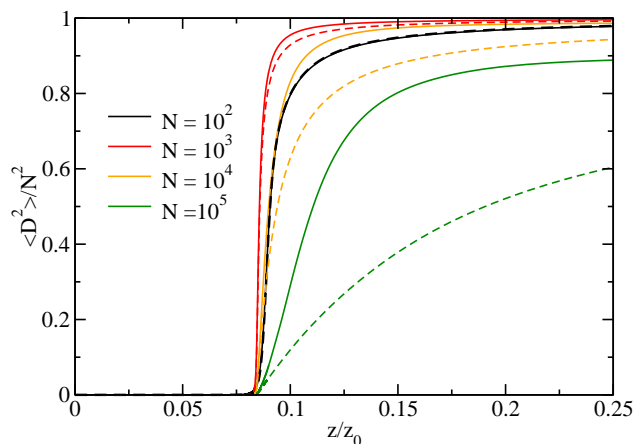
Figure 3.12: The average value of the squared total dipole moment divided by the system size squared as a function of the relative fugacity for different system sizes for the full Hamiltonian (solid lines) and for the SCA (dashed lines).

ment divided by the squared system size, $\langle D^2 \rangle / N^2$ as shown in Fig. 3.12 for different system sizes as a function of the relative fugacity. This order parameter is close to unity if the system is orientationally and translationally ordered and approaches zero for increasing disorder. Although the adsorption isotherm is steepest for $N = 10^5$ (see Fig. 3.8, where for $z/z_0 = 0.1$ the density is one for $N \gtrsim 10^4$), the order parameter starts to decrease at fugacities where the tube is still almost completely filled. This is a direct consequence of the peak in the chain density and the larger gaps for this system size which leads to a weaker coupling of the chains. Such weakly correlated chains can easily reorient and decrease the total dipole moment.

This conclusion is supported by results for the SCA (also shown in Fig. 3.12) which agree nicely with results for the full Hamiltonian for small system sizes of $N = 100$ and $N = 1000$ where fragmentation plays a minor role. For larger system sizes we observe that the square of the total dipole moment is lower for the SCA then for the full Hamiltonian. This indicates, that for the full Hamiltonian chains are coupled to their next neighbors via Coulomb-like interaction. Since the SCA is lacking these interactions, chains are uncorrelated, leading to a lower expectation value for the total dipole moment squared.

3.3.3   Bistability

It has already been observed for small systems at ambient conditions that the particle number distribution function is bimodal [16, 28], showing one peak for the empty and one for the full tube. In the following we investigate how this bistable behavior changes with system size and chemical potential and discuss the influence of the Coulomb-like interactions.

Similarly to Maibaum and Chandler in Ref. [28], we start the discussion with the Hamiltonian of a one-dimensional lattice gas in an external field h,

$$H = -J \sum_{i=1}^{N-1} s_i s_{i+1} - h \sum_{i=1}^{N} s_i , \qquad (3.7)$$

where the occupation number of site i is given by $s_i \in \{0, 1\}$ and the coupling constant of occupied sites by $J > 0$. This Hamiltonian can be written as

$$H = -(J + h)n + Jn_\mathrm{c} , \qquad (3.8)$$

where n is the total occupation number and n_c the number of domains (or chains) of particles. The above Hamiltonian is of the form

$$H = \mathcal{K}n + \mathcal{I}n_\mathrm{c} \qquad (3.9)$$

where $\mathcal{K}$ is the coupling constant and $\mathcal{I}$ the interface energy. The latter is the energy needed to break a chain into two and form two new interfaces between occupied and empty sites. In case of the NCA of the dipole model, the coupling constant is given by $\mathcal{K} = \beta c - \ln z$ and the interface energy by $\mathcal{I} = \beta c_\mathrm{c} - \ln 2$.

The particle number distribution of an ideal lattice gas (i.e., $\mathcal{I} = 0$) is given by the binomial distribution and therefore shows only a single peak. Only with a positive interface energy bistability of a partly or completely filled system and the empty system is observed. Then, the particle number distribution function is given by

$$P(n) \propto e^{-\beta \mathcal{K} n} \sum_{n_\mathrm{c}} \Gamma(n, n_\mathrm{c}) e^{-\beta n_\mathrm{c} I} \qquad (3.10)$$

where $\Gamma(n, n_\mathrm{c})$ is the number of states depending on the particle number and the number of chains, and a functional form that depends on the boundary conditions.

For periodic boundary conditions the number of states is given by [54]

$$\Gamma(n, n_\mathrm{c}) = \binom{n-1}{n_\mathrm{c}-1} \binom{N-n}{n_\mathrm{c}} + \binom{N-n-1}{n_\mathrm{c}-1} \binom{n}{n_\mathrm{c}} . \qquad (3.11)$$
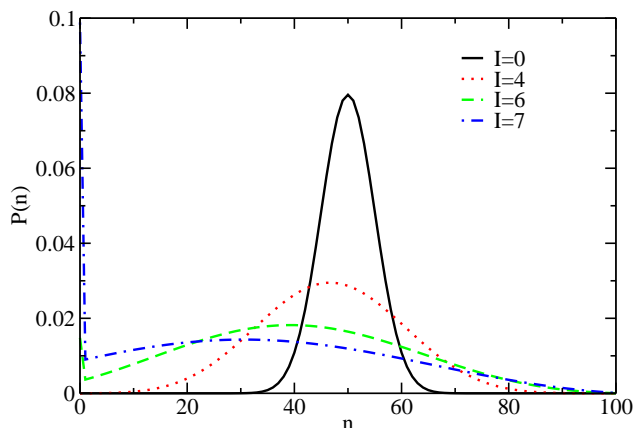
Figure 3.13: Particle number distributions for different values of the interface energy for a system with free boundary conditions of size $N = 100$ close to the filling transition ($\mathcal{K} = 0$). For an interface energy $I \gtrsim 6$ we observe a second peak for the empty system ($n = 0$).

For a constant number of chains, this function is unimodal and symmetric with respect to the location of its maximum at $n = N/2$. Thus the particle number distribution function is unimodal if one excludes the empty state. Free, rather than periodic, boundary conditions introduce a small asymmetry in the number of states, i.e.

$$\Gamma(n, n_{\mathrm{c}}) = \binom{n-1}{n_{\mathrm{c}} - 1} \binom{N - n + 1}{n_{\mathrm{c}}}, \qquad (3.12)$$

which is not sufficient to change this behavior.

For a positive interface energy, all non-empty states are energetically penalized according to their number of chains compared to the ideal lattice gas. Thus, the weight of the empty state in the partition function increases relative to the non-empty states and a second peak for $n = 0$ appears (see Fig. 3.13).

In contrast to this, water in nanopores shows a low density peak at densities larger than zero. The reason is that the Coulomb-like interaction of charges of opposite sign at the ends of short ordered chains lowers the internal energy of such chains compared to the energy they would have with nearest-neighbor interactions only. This is already the case for the SCA, where chains of length one, i.e., single dipoles for defect free systems, are treated separately.

In the following, we quantify this bistable behavior for the SCA as a function of the system size and the fugacity. We calculated the particle

Figure 3.14: Bistability map. Density plot of the bistability measure M of Eq. (3.18), which is close to one for a bistable system, for all investigated system sizes (top) and an enlarged view for large systems (bottom). The black solid lines are lines of constant density $\rho = 0.01, 0.5$, and 0.99 from left to right.

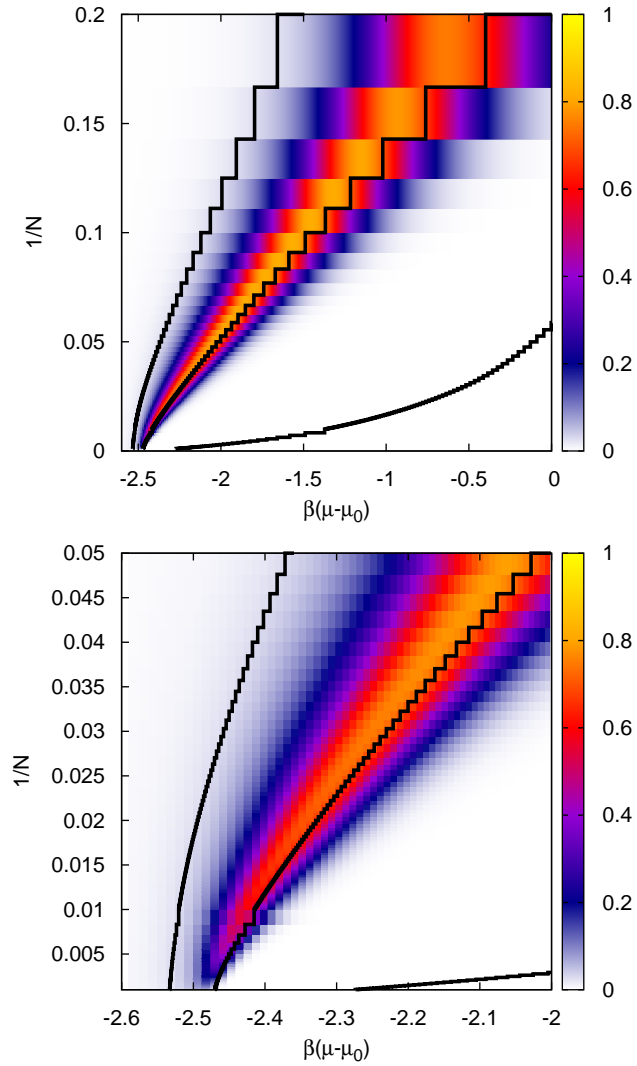number distribution function for system sizes up to $N = 1000$ for a certain value of the fugacity z. The particle number distribution function for the SCA is given by

$$P(n) \propto z^n \mathcal{Z}_N^{(1)}(n) \,, \tag{3.13}$$

with the canonical partition function $\mathcal{Z}_N^{(1)}(n)$ given by Eq. (2.41). We generated particle number distribution functions for fugacities in the range $z/z_0 \in [0, 1]$ by reweighting.

Bimodal particle number distribution functions show a low-density peak that is given by the binomial distribution of non-interacting particles,

$$P_{\mathrm{L}}(n) = \frac{1}{(1 + z2e^{-\beta S_{\mathrm{c}}})^N} \binom{N}{n} (2ze^{-\beta S_{\mathrm{c}}})^n \,. \tag{3.14}$$

Thus, we identify the low-density peak as

$$H_{\mathrm{L}}(n) = P_{\mathrm{L}}(n) \frac{P(0)}{P_{\mathrm{L}}(0)} \,, \tag{3.15}$$

where the factor $P(0)/P_{\mathrm{L}}(0)$ guarantees that the distribution function $P(n)$ and the low-density peak $H_{\mathrm{L}}(n)$ coincide for the empty tube, i.e., for $n = 0$. The second peak is a high-density peak, defined by $H_{\mathrm{H}}(n) = P(n) - H_{\mathrm{L}}(n)$.

Next, we define a measure M that quantifies the extent of bistability. It should be large if the areas below the two peaks, given by $N_{\mathrm{H}} = \sum_n H_{\mathrm{H}}(n)$ and $N_{\mathrm{L}} = \sum_n H_{\mathrm{L}}(n) = 1 - N_{\mathrm{H}}$, are of comparable size. Thus, we form the product of the two areas,

$$\mathcal{A} = 4N_{\mathrm{H}}N_{\mathrm{L}} \,. \tag{3.16}$$

The factor 4 ensures that $\mathcal{A} = 1$ if the two peaks have equal weight. If one peak dominates the particle number distribution function, then $\mathcal{A} \approx 0$.

If the two peaks were due to coexistence at a first order phase transition, changing the fugacity would only change the relative weight of the two peaks. Here, the location of the peaks changes with the fugacity. Thus, our measure should also include the distance between the two peaks. The positions of the peaks are given by the mean values of the low-density and the high-density peak and their distance R can be written as

$$R = \frac{1}{N} \sum_n n \left[\frac{H_{\mathrm{H}}(n)}{N_{\mathrm{H}}} - \frac{H_{\mathrm{L}}(n)}{N_{\mathrm{L}}} \right] \,. \tag{3.17}$$

Thus, we define our measure for bistability M as the product of $\mathcal{A}$ and the distance R,

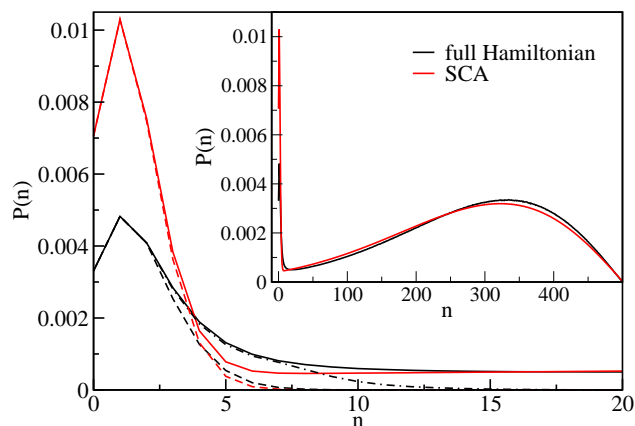$$M = R\mathcal{A} = 4RN_{\mathrm{H}}N_{\mathrm{L}} \,. \tag{3.18}$$

Figure 3.15: Particle distribution functions for $N = 500$ and $z/z_0 = 0.085$ for the full Hamiltonian and in the SCA. The dashed lines show fits of the low density peaks with binomial distributions of non-interacting single dipoles. The dashed-dotted line is a fit of a binomial distribution of non-interacting chains (with charges at their ends) up to a length of ten particles. The inset shows the distribution functions for the full range of the particle number.

Figure 3.14 shows a density plot of this measure as a function of the inverse system size and the chemical potential. For small systems, the bi-modal structure of the particle number distribution function can be seen for ambient conditions corresponding to $\mu = \mu_0$, as has also been observed in computer simulations [16]. For larger system sizes, the range of the chemical potential where bimodality is observed becomes narrower and the bimodality itself weaker. For $N \gg 1000$ bimodality vanishes completely. Also shown are the lines where the system is empty (average density $\rho = 0.01$), full ($\rho = 0.99$), and half filled ($\rho = 0.5$). For $1/N \to 0$ the density is determined by the corresponding value of the chemical potential in the thermodynamic limit. In this case, the lines of constant density intersect the μ-axis verti-cally. For the largest system sizes investigated here ($N = 1000$), the densities $\rho = 0.01$ and $\rho = 0.5$ and the corresponding chemical potentials are close to their values in the thermodynamic limit. This is, however, not the case for $\rho = 0.99$ (see Fig. 3.8) as the corresponding line of constant density does not seem to intersect the μ-axis at a right angle on the scale of Fig. 3.14. The maximum of the bistability measure is always to the left, i.e., at lower chemical potential, of the line of half filling. The bistability map for NCA (not shown) is nearly identical to the map for SCA.

The situation for the full Hamiltonian is slightly different from that in the SCA as exemplified in Fig. 3.15. The low-density peak is not perfectly
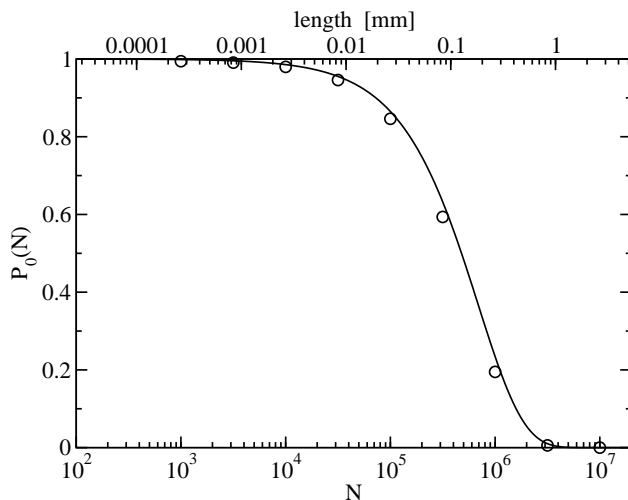
Figure 3.16: Order probability $P_0(N)$ obtained from canonical Monte Carlo simulations (circles) of a single chain as a function of the number of sites, N (lower x-axis). Also shown is the order probability calculated according to Eq. (3.19) (solid line). The labels on the upper x-axis indicate the corresponding tube length.

reproduced by a binomial distribution of non-interacting, single dipoles. Instead, we have to take into account the contributions of longer chains, that do not interact with each other, but whose energy is lowered (compared to the SCA) due to the effective charges at their ends. The peak is well reproduced if we include chains with lengths up to ten sites. Thus, the form of the low density peak can be explained by the lower energies of chains in the full Hamiltonian compared to the SCA.

3.4   The completely filled tube

3.4.1   Macroscopic dipolar order

In completely filled tubes at ambient conditions, narrow gaps one lattice spacing wide occur, but do not influence the ordering behavior of the chain, which is purely determined by the occurrence of orientational defects. Thus, we performed canonical Monte Carlo simulations of a full tube at ambient conditions for system sizes up to 10^7 water molecules, which become feasible in the charge representation. As a measure of the dipolar ordering of the system, we define the probability $P_0(N)$ that all water dipoles point in the same direction, for a system with N lattice sites. As shown in Fig. 3.16, the order probability decays only slowly with increasing system size and reaches
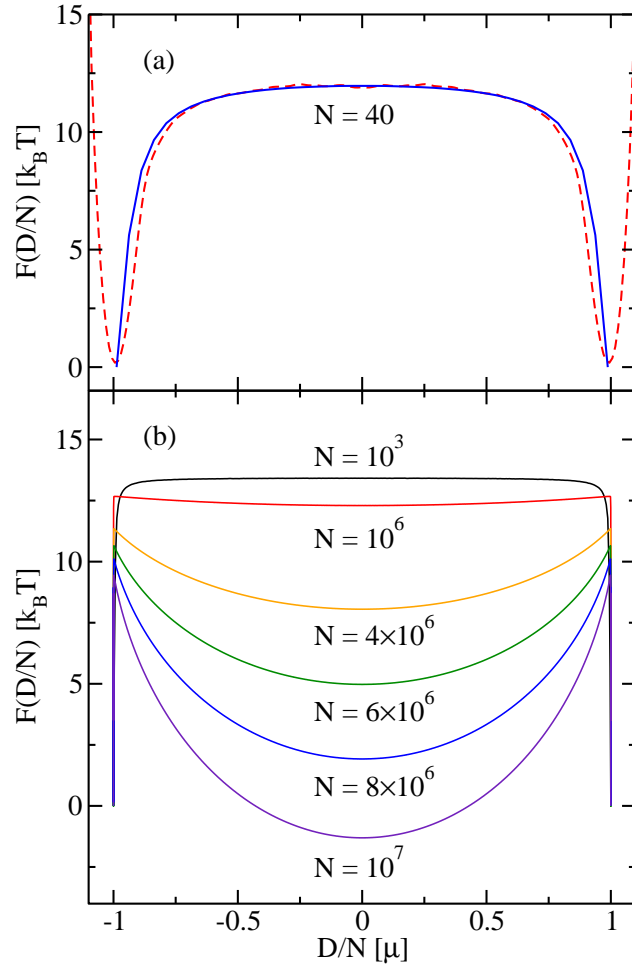
Figure 3.17: Free energy, $F(D/N)$, as a function of the total dipole moment, D, per site, N, of a fully water-filled tube at ambient conditions. (a) Comparison of $F(D/N)$ from atomistic Monte Carlo simulations (dashed line) and the dipole lattice model (solid line) for $N = 40$ water molecules. (b) $F(D/N)$ from the dipole lattice model for different system sizes. The curves are shifted so that the free energy vanishes for the ordered states $(D/N = \pm 1)$. For $N \lesssim 10^5$ the free energy barrier between the ordered states is flat, whereas for larger system sizes the curves exhibit a minimum for vanishing total dipole moment.

a 50%-ordered state at a macroscopic tube length of ~ 0.1 mm.

This macroscopic ordering can be explained with a simplified model of uncorrelated defects. Let $p = \exp(-\beta E_{\mathcal{D}})/[1 + \exp(-\beta E_{\mathcal{D}})]$ be the probability of an isolated defect within a long water chain, with $E_{\mathcal{D}}$ the free energy

of creating the defect, and $\beta^{-1} = k_B T$, where k_B is Boltzmann's constant and T is the absolute temperature. The probability $P_0(N)$ of finding no defect in a fully occupied system of N sites can then be approximated as

$$P_0(N) \approx (1 - p)^N = (1 + e^{-\beta E_\mathcal{D}})^{-N} \ . \qquad (3.19)$$

With the dipole model parameterized for water in (6,6) carbon nanotubes,we find that $E_\mathcal{D} \approx 13.4 \ k_B T$. As shown in Fig. 3.16, the order probability resulting from Eq. (3.19) agrees very well with the results of the canonical Monte Carlo simulations up to tube lengths of 1 mm.

The transition from dipole-ordered to disordered systems at tube lengths of > 0.1 mm is reflected in the free energy (or potential of mean force), $F(D/N)$, as a function of the dipole moment per site, D/N. Figure 3.17(a) shows that the dipole lattice model accurately reproduces the free energy profiles obtained from atomistic simulations, and thus the energetics of dipole defect formation. Free energies obtained for the dipole model for large system sizes are depicted in Fig. 3.17(b). For $N < 10^6$ water molecules, the system is either in an "up" or "down" state, with sharp minima at the two fully ordered states ($D/N = \pm 1$). For intermediate total dipole moments the free energy profile is flat since different values of the total dipole moment correspond to different positions of a single defect moving along the chain at no free energetic cost. With increasing system size, the ordered states become less stable since defect numbers increase. Eventually, for large systems, the dipole moment distributions become essentially Gaussian centered at zero, with additional local maxima at $D/N = \pm 1$ corresponding to residual ordered states. The width of the Gaussian distributions (for the dipole moment per site) decreases with increasing system size.

In summary, we find that at ambient conditions single-file water chains remain ordered up to macroscopic lengths of almost millimeter size.

Remarks on the molecular reference system

We note that TIP3P water offers only an approximate representation of water in nanotubes. The dipole moment entering the dipolar model appears thus somewhat uncertain. However, earlier studies of water inside (6,6)-type carbon nanotubes, in which both water and the nanotubes were treated using quantum-mechanical density functional theory, produced a dipole moment even higher than that of the classical TIP3P water model [15]. An explanation for such highly polarized water is the strongly collective character of the hydrogen bond interactions in dipole-oriented water chains. Similarly, in small water clusters dipole moments of ~ 2.7 Debye have been found [55],

exceeding the 2.35 Debye of TIP3P water. For a larger dipole moment the macroscopic ordering found in our simulations would be even more pronounced.

A second concern is that the interactions of water with the nanotube are somewhat uncertain, and small changes in those interactions can have large effects on the equilibrium between filled and empty states [16]. Thermodynamically, such changes are essentially equivalent to changes in the fugacity (or vapor pressure) of the water bath and would only shift the filling curves of Figs. 3.6 and 3.7 on the fugacity axis. The ordering properties of the completely filled tube would not be affected by this changed fugacity.

3.4.2   Uncorrelated defects and defect pairs

The agreement of the results for the order probability for the full Hamiltonian and for uncorrelated defects in Fig. 3.16 is good, but the order probability is overestimated by the analytical result. As we shall see in the following, this difference is due to the formation of defect pairs which consist of an L-defect and a D-defect separated by a single molecule. We first discuss a system of uncorrelated defects before taking into account uncorrelated defect pairs. We find that for large system sizes the approximation of uncorrelated defects and defect pairs quantitatively reproduces the order probability, the average defect number, and the free energy as a function of the total dipole moment.

Uncorrelated defects

We assume that all Coulomb-like interactions are neglected and choose the ordered states with all molecules pointing either "up" or "down" the tube axis as reference point for the total energy. As a consequence, the total energy of the system is given by the defect excitation energy times the number of defects, $n_{\mathrm{d}} E_{\mathcal{D}}$. The number of possible states as a function of the system size and the number of defects, $\Gamma_N(n_{\mathrm{d}})$, is determined by the number of possibilities to insert n_{d} defects into the chain of length N, which is given by a binomial coefficient, for each of the two possible orientations of the chain. Thus, we obtain

$$\Gamma_N(n_{\mathrm{d}}) = 2\binom{N - n_{\mathrm{d}} - 1}{n_{\mathrm{d}}}. \tag{3.20}$$

In this approximation, the partition function of a single chain can be written as

$$Z(\beta, N) = \sum_{n_{\mathrm{d}}=0}^{n_{\mathrm{d}}^{\max}} \Gamma_N(n_{\mathrm{d}}) e^{-\beta E_{\mathcal{D}} n_{\mathrm{d}}}, \tag{3.21}$$

where $n_{\mathrm{d}}^{\max}$ is the maximum number of defects given by

$$n_{\mathrm{d}}^{\max}(N) = \begin{cases} \frac{N}{2} - 1 & \text{for} \quad N \text{ even} \\ \frac{N-1}{2} & \text{for} \quad N \text{ odd} \end{cases}. \tag{3.22}$$

The Coulomb-like interactions between defects and chain ends can be neglected if the distances between defects (and ends) are large for most configurations in the canonical ensemble, i.e., if the defect number is small compared to the number of sites. For such systems, we can approximate $N - n_{\mathrm{d}} - 1$ by N in the factorial of Eq. (3.20) which leads to the following expression for the canonical partition function of a one-dimensional gas of uncorrelated, single defects,

$$Z_{\mathrm{s}}(\beta, N) = 2 \sum_{n_{\mathrm{d}}=0}^{n_{\mathrm{d}}^{\max}} \binom{N}{n_{\mathrm{d}}} e^{-\beta E_{\mathcal{D}} n_{\mathrm{d}}} . \tag{3.23}$$

For a large defect excitation energy, this expression can be approximated by

$$Z_{\mathrm{s}}(\beta, N) \approx 2(1 + e^{-\beta E_{\mathcal{D}}})^N . \tag{3.24}$$

We can easily derive an approximation for the average defect number $\langle n_{\mathrm{d}} \rangle$ from Eq. (3.23),

$$\langle n_{\mathrm{d}} \rangle = -\frac{1}{Z_{\mathrm{s}}(\beta, N)} \frac{\partial Z_{\mathrm{s}}(\beta, N)}{\partial(\beta E_{\mathcal{D}})} = N \frac{e^{-\beta E_{\mathcal{D}}}}{1 + e^{-\beta E_{\mathcal{D}}}} . \tag{3.25}$$

The order probability $P_0(N)$, i.e., the probability that the system is free of defects, is simply given by the number of ordered states divided by the partition function,

$$P_0(N) = \frac{2}{Z_{\mathrm{s}}(\beta, N)} = (1 + e^{-\beta E_{\mathcal{D}}})^{-N} , \tag{3.26}$$

in agreement with Eq. (3.19).

In Fig. 3.18, we compare this approximation with simulation results for the full Hamiltonian and for the NCA. In the latter, all Coulomb-like interactions are neglected but the configurational constraints dictated by the model are satisfied. We find excellent agreement between the NCA and the analytical result for uncorrelated defects, where configurational constraints are ignored. Both approximations overestimate the order probability compared to the full Hamiltonian. This difference is due to the occurrence of defect pairs, as we shall see in the following.
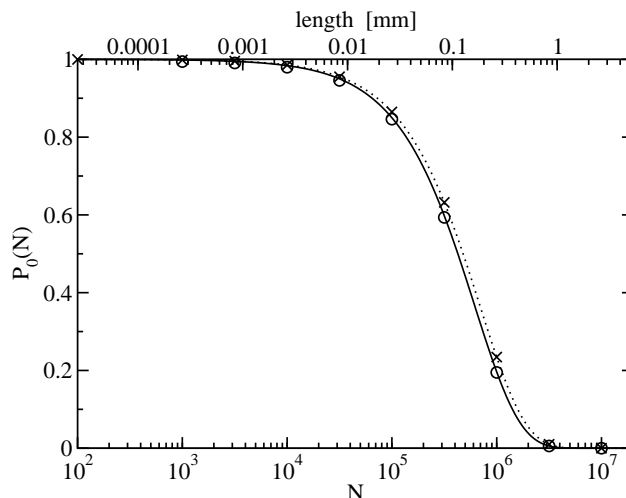
Figure 3.18: The order probability as a function of the total system size. Results for uncorrelated defects (dotted line) agree well with simulation results of the NCA (crosses). Simulation results for the full Hamiltonian (circles) are reproduced by the approximation of uncorrelated defects and defect pairs (solid line).

Uncorrelated defect pairs

A defect pair is formed by an L- and a D-defect separated by a single molecule. In contrast to single defects, which are formed at chain ends and which are mobile, defect pairs are formed anywhere within ordered segments and are immobile. The reason for the latter is that a defect pair is an energetically unstable configuration and a hop of this pair, which would require the concerted motion of the two defects, is improbable. The generation of a defect pair within an ordered segment with orientation s changes the total dipole moment by $-4s\mu$ independent of its position within the segment. Since in the charge picture the L- and and the D-defect are formed by charges of the same magnitude but opposite sign, a defect pair is charge neutral and forms an effective dipole. As a consequence, the interactions of a defect pair with other effective charges decay fast with the distance, as we shall see next.

The interaction energy of a defect pair with the next defect in the chain can be written as

$$\phi(x) = \phi_{\mathrm{LD}}(x-1) - \phi_{\mathrm{LD}}(x+1) \qquad (3.27)$$

where x is the distance between the defect and the center molecules of the defect pair and $\phi_{\mathrm{LD}}(x)$ is the interaction energy of an L- and a D-defect
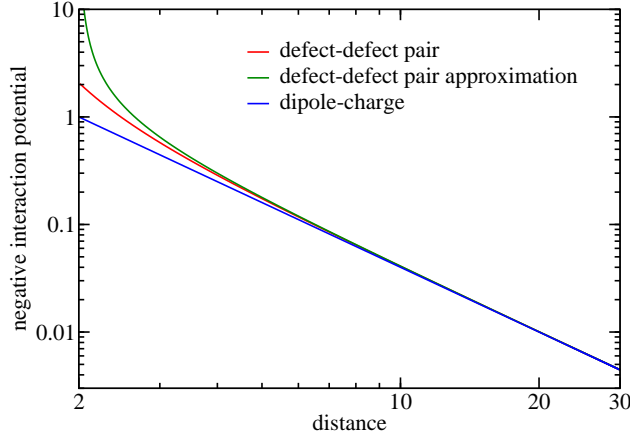
Figure 3.19: Double logarithmic plot of the negative interaction energy of a defect pair and a single defect as a function of the distance. The exact expression [Eq. (3.29), red], the approximation of Coulomb interactions between the constituting charges [Eq. (3.30), green], and the dipole-charge interaction [Eq. (3.33), blue] agree well with each other for distances larger than ~ 5 lattice spacings.

separated by a distance x,

$$\phi_{\mathrm{LD}}(x) = -\left[\Phi(x-1) + \Phi(x+1) + 2\Phi(x)\right], \tag{3.28}$$

where $\Phi(x)$ is the Coulomb-like interaction energy given by Eq. (2.10). Thus, we obtain

$$\phi(x) = \left[\Phi(x+2) - \Phi(x-2)\right] + 2\left[\Phi(x+1) - \Phi(x-1)\right], \tag{3.29}$$

which can approximated as

$$\phi(x) \approx \frac{1}{2}\left[\frac{1}{x-2} - \frac{1}{x+2}\right] + \left[\frac{1}{x-1} - \frac{1}{x+1}\right], \tag{3.30}$$

using $\Phi(x) \approx 1/(2x)$. From the series expansion of the terms in brackets,

$$\left[\frac{1}{x-k} - \frac{1}{x+k}\right] = \frac{2k}{x^2 - k^2} = \tag{3.31}$$

$$= -\frac{2k}{x^2} - \frac{2k^3}{x^4} - \frac{2k^5}{x^6} - \mathcal{O}\left(\frac{1}{x^8}\right), \tag{3.32}$$

we estimate the defect-defect pair interaction potential as

$$\phi(x) \approx -\frac{4}{x^2}. \tag{3.33}$$

With the unit of energy given by $\epsilon = 2\mu^2/(4\pi\varepsilon_0 a^3)$, this potential describes the interaction of a dipole of magnitude 4μ, representing the defect pair, and a charge of magnitude $2\mu/a$, representing the single defect.

In Fig. 3.19 we compare the different expressions for the defect pair interaction energy with each other. For distances larger than approximately five lattice spacings, the various expression for the defect-defect pair interaction agree well with each other.

With the interaction energies of defects decaying rapidly with distance, the excitation energy of a defect pair far from other effective charges is given by the sum of twice the defect excitation energy $E_{\mathcal{D}}$ and the interaction energy of the two defects, $I_{\mathrm{p}} = \Phi(1) + 2\Phi(2) + \Phi(3)$, as

$$E_{\mathrm{p}} = 2E_{\mathcal{D}} + I_{\mathrm{p}}\,, \tag{3.34}$$

where $\Phi(x)$ is the Coulomb-like interaction. Due to the large interaction energy of the two defects forming the defect pair, the defect pair excitation energy is only about 15% larger than the excitation energy of a single defect. For a water-filled carbon nanotube at ambient conditions (see Sec. 3.2), the defect pair excitation energy is $\beta E_{\mathrm{p}} \approx 15.55$, compared to $\beta E_{\mathcal{D}} \approx 13.44$ for the excitation energy of a single defect.

Due to the high excitation energies the defect pair density will be low, but cannot be neglected with respect to the density of single defects. For large system sizes, we can safely assume that defect pairs are uncorrelated and independent of single defects.

Thus, in the approximation of uncorrelated defects and defect pairs, the partition function of a competely filled tube factorizes, i.e.,

$$\begin{aligned} Z(\beta, N) &= Z_{\mathrm{s}}(\beta, N)Z_{\mathrm{p}}(\beta, N) = \\ &= 2\left[(1 + e^{-\beta E_{\mathcal{D}}})(1 + e^{-\beta E_{\mathrm{p}}})\right]^N. \end{aligned} \tag{3.35}$$

Here, $Z_{\mathrm{s}}(\beta, N)$ is the partition function of a system of uncorrelated defects given by Eq. (3.24) and the partition function of a system of uncorrelated defect pairs, $Z_{\mathrm{p}}(\beta, N)$, is given by

$$Z_{\mathrm{p}}(\beta, N) = \sum_{n_{\mathrm{p}}=0}^{n_{\mathrm{p}}^{\max}} \binom{N}{n_{\mathrm{p}}} e^{-\beta E_{\mathrm{p}} n_{\mathrm{p}}} \approx (1 + e^{-\beta E_{\mathrm{p}}})^N\,, \tag{3.36}$$

where $n_{\mathrm{p}}^{\max}$ is the maximum number of defect pairs. The order probability becomes

$$P_0(N) \approx \frac{2}{Z(\beta, N)} = \left[(1 + e^{-\beta E_{\mathcal{D}}})(1 + e^{-\beta E_{\mathrm{p}}})\right]^{-N}\,, \tag{3.37}$$
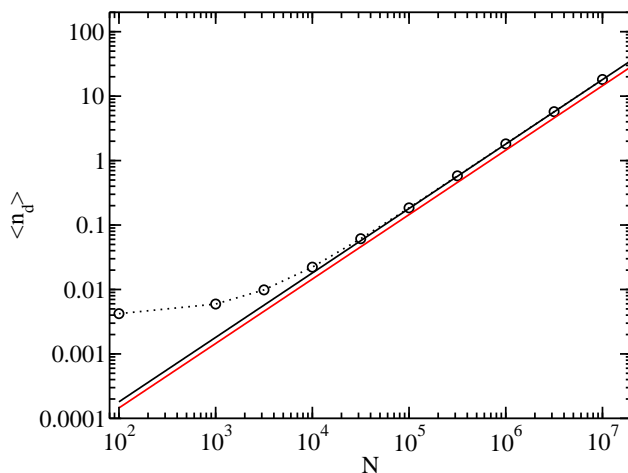
Figure 3.20: The average defect number as a function of the number of sites. Simulation results are depicted as circles and connected by dotted lines as guide to the eye. The approximation of uncorrelated defects is shown as solid red line, and the approximation also including uncorrelated defect pairs as solid black line.

which now is in excellent agreement with simulation results for the full Hamiltonian, as shown in Fig. 3.18. The average defect number is given by

$$\langle n_{\mathrm{d}} \rangle = \frac{1}{Z(\beta, N)} \left[\frac{\partial Z(\beta, N)}{\partial(\beta E_{\mathcal{D}})} + 2 \frac{\partial Z(\beta, N)}{\partial(\beta E_{\mathrm{p}})} \right], \qquad (3.38)$$

and we obtain

$$\langle n_{\mathrm{d}} \rangle / N = \frac{e^{-\beta E_{\mathcal{D}}}}{1 + e^{-\beta E_{\mathcal{D}}}} + 2 \frac{e^{-\beta E_{\mathrm{p}}}}{1 + e^{-\beta E_{\mathrm{p}}}} . \qquad (3.39)$$

In Fig. 3.20 we compare this analytical expression for the average defect number with simulation results for the full Hamiltonian. For small system sizes the Coulomb-like interaction of the defects with chain ends cannot be neglected. This leads to a higher defect density compared to a system of uncorrelated defects. For longer tubes the results of the full Hamiltonian agree well with the approximation of uncorrelated defects and defect pairs, but the average defect number is underestimated by a system of uncorrelated defects only.

In summary, for long tubes the order probability and the average defect number are quantitatively reproduced by a system consisting of uncorrelated defects and uncorrelated defect pairs. As we shall see in the following, for uncorrelated, single defects we can establish a relation to the Ising model with free boundary conditions, which allows us to derive an analytical expression for the free energy as a function of the total dipole moment.

3.4.3   Total dipole moment

We derive an analytical expression for the partition function for fixed value of the total dipole moment, and thus the dipole moment distribution and free energy, of a system of uncorrelated defects. To this end, we count the number of states as a function of the total dipole moment and the number of defects.

Partition function for fixed total dipole moment

We treat ordered and disordered states separately and write the partition function for fixed value of the total dipole moment as

$$Z_{\mathrm{N}}(D) = \begin{cases} 1 & \text{for } |D| = N \\ \mathcal{Z}_N(D) & \text{else.} \end{cases} \tag{3.40}$$

For the derivation of $\mathcal{Z}_N(D)$ we only consider disordered chains with at least one single defect, where positively and negatively oriented segments alternate. Numbering the chains from left to right, from 1 to $n_{\mathrm{d}}+1$, segments with odd and even index are oriented in the opposite direction. For an odd number of defects the number of segments with odd indices, given by $n_{\mathrm{o}} = (n_{\mathrm{d}} + 1)/2$, is equal to the number of segments with even indices, $n_{\mathrm{e}} = n_{\mathrm{o}}$. For an even defect number, the number of segments with odd indices, given by $n_{\mathrm{o}} = (n_{\mathrm{d}} + 1)/2$, is larger by one than the number of segments with even indices, i.e., $n_{\mathrm{e}} = n_{\mathrm{o}} - 1$.

The total lengths of the odd indexed segments, l_{o}, and the length of the even indexed segments, l_{e}, are not independent and their sum is given by

$$l_{\mathrm{e}} + l_{\mathrm{o}} = N - n_{\mathrm{d}} \,. \tag{3.41}$$

The orientations of all segments are determined by the orientation of the first segment, s. As a consequence, the total dipole moment can be written as

$$sD = l_{\mathrm{o}} - l_{\mathrm{e}} = 2l_{\mathrm{o}} - N + n_{\mathrm{d}} \tag{3.42}$$

and depends on s, l_{o}, and n_{d}. The above equations reflect the symmetry expressed by

$$l_{\mathrm{o}}(D, n_{\mathrm{d}}, s = \pm 1) = l_{\mathrm{e}}(D, n_{\mathrm{d}}, s = \mp 1) \,, \tag{3.43}$$

which states that a specific value of the total dipole moment can be realized by n_{d} defects and either a positive orientation, $s = +1$, and $l_{\mathrm{o}} = l_{+}$ and $l_{\mathrm{e}} = l_{-}$, where

$$l_{\pm} = \frac{N - n_{\mathrm{d}} \pm D}{2} \,, \tag{3.44}$$

or by a negative orientation, $s = -1$, and exchanged total lengths, i.e., $l_{\mathrm{o}} = l_{-}$ and $l_{\mathrm{e}} = l_{+}$.

Next, we count the number of states, $\Gamma(D, n_{\mathrm{d}})$, as a function of the total dipole moment D and the defect number n_{d}. For a given orientation s, the number of states is given by the number of possibilities to split a segment of length l_{o} in n_{o} parts, times the number of possibilities to split a segment of length l_{e} in n_{e} parts (see also App. A). Since a dipole moment D can be realized by $s = \pm 1$ we obtain

$$\Gamma(D, n_{\mathrm{d}}) = \sum_{s=-1,1} \binom{l_{\mathrm{o}} - 1}{n_{\mathrm{o}} - 1} \binom{l_{\mathrm{e}} - 1}{n_{\mathrm{e}} - 1}, \qquad (3.45)$$

where l_{o}, l_{e}, n_{o}, and n_{e} depend on s, D, and n_{d}. The canonical partition function of disordered states can be written as

$$\mathcal{Z}_N(D) = \sum_{n_{\mathrm{d}}=1}^{n_{\mathrm{d}}^{\max}} \Gamma(D, n_{\mathrm{d}}) e^{-\beta E_{\mathcal{D}} n_{\mathrm{d}}}, \qquad (3.46)$$

with the maximum number of defects $n_{\mathrm{d}}^{\max}$ given by Eq. (3.22).

Relation to the one-dimensional Ising model

For large system sizes we assume that the defect number is much smaller than the number of sites and that defects are uncorrelated. In a first step, we ignore configurational constraints dictated by the dipole lattice model and that domain walls are formed by defect molecules located on lattice sites. This approximation allows us to establish a relation to the one-dimensional Ising model where domain walls are located between lattice sites. In Ref. [54], the partition function as a function of the magnetization was derived for the 1D Ising model using various boundary conditions. As our model of uncorrelated defects corresponds to an 1D Ising model with free boundary conditions, we can follow their calculations to a large extent to obtain the free energy as a function of the total dipole moment[1].

For uncorrelated defects, Eqs. (3.41), (3.42), and (3.44) become $l_{\mathrm{e}} + l_{\mathrm{o}} = N$, $sD = l_{\mathrm{o}} - l_{\mathrm{e}} = 2l_{\mathrm{o}} - N$, and $l_{\pm} = (N \pm D)/2$ and we obtain for the number of states

$$\begin{aligned}
\Gamma(D, n_{\mathrm{d}}) &= \sum_{s=-1,1} \binom{l_{\mathrm{o}}}{n_{\mathrm{o}} - 1} \binom{N - l_{\mathrm{o}}}{n_{\mathrm{e}} - 1} = \qquad (3.47) \\
&= \binom{l_{+}}{n_{\mathrm{o}} - 1} \binom{N - l_{+}}{n_{\mathrm{e}} - 1} + \binom{N - l_{+}}{n_{\mathrm{o}} - 1} \binom{l_{+}}{n_{\mathrm{e}} - 1}.
\end{aligned}$$

---

[1] We performed the following derivation ourselves before we found out that it was already done in Ref. [54]. Always keep in mind that "two month in the laboratory can spare you a few hours in the library".

In the following we treat the case of an odd number of defects, i.e., $n_\text{o} = n_\text{e}$, for which the number of states is given by

$$\Gamma_\text{o}(D, n_\text{o}) = 2 \binom{l_+}{n_\text{o} - 1} \binom{N - l_+}{n_\text{o} - 1} , \tag{3.48}$$

and the case of an even number of defects, i.e., $n_\text{o} = n_\text{e} - 1$, with the number of states given by

$$\begin{aligned}\Gamma_\text{e}(D, n_\text{o}) & = \binom{l_+}{n_\text{o} - 1} \binom{N - l_+}{n_\text{o} - 2} + \\ & + \binom{N - l_+}{n_\text{o} - 1} \binom{l_+}{n_\text{o} - 2}\end{aligned} \tag{3.49}$$

separately. The partition function for an odd number of defects is given by

$$Z_\text{o}(D) = \sum_{n_\text{o}=1}^{n_\text{o}^{\max}} \Gamma_\text{o}(D, n_\text{o}) b^{2n_\text{o}-1} , \tag{3.50}$$

and for an even number of defects by

$$Z_\text{e}(D) = \sum_{n_\text{o}=2}^{n_\text{o}^{\max}} \Gamma_\text{e}(D, n_\text{o}) b^{2n_\text{o}-2} , \tag{3.51}$$

where b is the Boltzmann factor, $b = e^{-\beta E_\mathcal{D}}$. Next, we use Stirling's approximation for the binomial coefficients, i.e., $\binom{M}{m} \approx M^m / m!$, which leads to the following expression for the partition functions for an odd number of defects

$$Z_\text{o}(D) = 2b \sum_{n_\text{o}=1}^{n_\text{o}^{\max}} \frac{\left[l_+ (N - l_+) b^2 \right]^{n_\text{o}-1}}{(n_\text{o} - 1)!(n_\text{o} - 1)!} , \tag{3.52}$$

and for an even number of defects

$$Z_\text{e}(D) = Nb^2 \sum_{n_\text{o}=2}^{n_\text{o}^{\max}} \frac{\left[l_+ (N - l_+) b^2 \right]^{n_\text{o}-2}}{(n_\text{o} - 2)!(n_\text{o} - 2)!} \frac{1}{n_\text{o} - 1} . \tag{3.53}$$

We can simplify the above expressions using modified Bessel functions of the first kind, $I_0(x)$ and $I_1(x)$ [48]. For $Z_\text{o}(D)$ we use

$$I_0(2\sqrt{x}) = \sum_{n=0}^{\infty} \frac{x^n}{n!n!} \tag{3.54}$$

and obtain

$$Z_\text{o}(D) = 2b I_0(2b\sqrt{l_+[N - l_+]}) , \tag{3.55}$$

and for $Z_{\mathrm{e}}(D)$ we apply

$$\frac{I_1(2\sqrt{x})}{\sqrt{x}} = \sum_{n=0}^{\infty} \frac{x^n}{n!n!}\frac{1}{n+1} \tag{3.56}$$

and obtain

$$Z_{\mathrm{e}}(D) = Nb^2 \frac{I_1(2b\sqrt{l_+[N-l_+]})}{b\sqrt{l_+(N-l_+)}} \,. \tag{3.57}$$

The argument of the Bessel functions in the partition functions above can be written as

$$l_+(N-l_+) = \frac{N^2 - D^2}{4} \,, \tag{3.58}$$

which leads to

$$Z_{\mathrm{o}}(D) = 2bI_0(b\sqrt{N^2-D^2}) \tag{3.59}$$

and

$$Z_{\mathrm{e}}(D) = 2bN\frac{I_1(b\sqrt{N^2-D^2})}{\sqrt{N^2-D^2}} \,. \tag{3.60}$$

Discretization of the total dipole moment

Up to now, we have assumed that domain walls are located between molecules as in the Ising model, where the partition function is given by the sum $\mathcal{Z}_N(D) = Z_{\mathrm{o}}(D) + Z_{\mathrm{e}}(D)$. In contrast, in a chain of water molecules domain walls are formed by defect molecules. As a consequence, the sets of values of the total dipole moment that can be realized by a chain with an odd or even number of defects are disjoint. The total dipole moment of a chain with an odd number of defects can take values of the set

$$\mathcal{S}_{\mathrm{o}} = \{-(N-3), -(N-5), \dots N-5, N-3\} \,, \tag{3.61}$$

and with an even number of defects of the set

$$\mathcal{S}_{\mathrm{e}} = \{-(N-4), -(N-6), \dots N-6, N-4\} \,. \tag{3.62}$$

Thus, we have do differentiate between an odd and an even number of defects, i.e.,

$$\mathcal{Z}_N(D) = \begin{cases} Z_{\mathrm{o}}(D) & \text{for} \quad D \in \mathcal{S}_{\mathrm{o}} \\ Z_{\mathrm{e}}(D) & \text{for} \quad D \in \mathcal{S}_{\mathrm{e}} \end{cases} \,. \tag{3.63}$$

Under the assumption of a large system size, which is a precondition for this derivation, we can avoid this case differentiation by approximating the partition function as

$$\mathcal{Z}_N(D) = \frac{1}{2}\left[Z_{\mathrm{o}}(D) + Z_{\mathrm{e}}(D)\right] \,, \tag{3.64}$$

which leads to

$$\mathcal{Z}_N(D) = bI_0(by) + Nb\frac{I_1(by)}{y}\,, \tag{3.65}$$

with $y = \sqrt{N^2 - D^2}$. This approximation can be understood as a coarse graining of the partition function given by Eq. (3.63), where we assign neighboring values of the total dipole moment the average of the corresponding values of the partion function.

The partition function for fixed value of D, Eq. (3.40), is then given by

$$Z_{\mathrm{N}}(D) = \begin{cases} 1 & \text{for } |D| = N \\ bI_0(by) + Nb\frac{I_1(by)}{y} & \text{else,} \end{cases} \tag{3.66}$$

and we obtain for the total dipole moment distribution

$$P_N(D) = \frac{1}{Z_N}Z_N(D)\,, \tag{3.67}$$

where

$$Z_N = 2 + \sum_{D=-N+3}^{N-3} \mathcal{Z}_N(D)\,. \tag{3.68}$$

Consequently, the free energy as a function of the total dipole moment is given by

$$\beta F(D) = -\ln Z_N(D)\,. \tag{3.69}$$

Note, for sufficiently large system sizes the sum in Eq. (3.68) can be approximated by integrals.

Uncorrelated defects and defect pairs

In Fig. 3.21 we compare the free energy as a function of the total dipole moment obtained from simulations using the full Hamiltonian and from the analytical expression for uncorrelated defects, Eq. (3.69). Although the form of the free energy for disordered states is captured by the approximation of uncorrelated, single defects, it is shifted to higher free energies compared to the ordered states. The reason is that uncorrelated defect pairs lead to a larger statistical weight of the disordered states in the partition function, i.e.,

$$Z_{\mathrm{N}}(D) = \begin{cases} 1 & \text{for } |D| = N \\ b\left[I_0(by) + N\frac{I_1(by)}{y}\right](1 + e^{-\beta E_{\mathrm{P}}})^N & \text{else.} \end{cases} \tag{3.70}$$

Here, we used that the change in the total dipole moment due to the generation or recombination of defect pairs is small, compared to the change caused
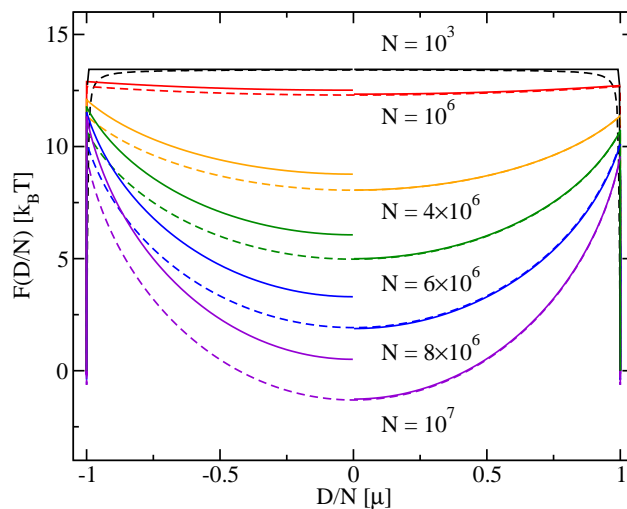
Figure 3.21: The free energy as a function of the total dipole moment per site. The curves are shifted so that the free energy of the ordered states vanishes. Dashed lines are simulation results for the full Hamiltonian. For negative values of the total dipole moment we plot the free energy for uncorrelated defects, which have a higher free energy at vanishing dipole moment than the results for the full Hamiltonian. For positive values of the total dipole moment we show results including uncorrelated defect pairs which agree well with the results for the full Hamiltonian. Note that for long tube lengths, defect pairs lead to a lower free energy of nearly ordered states with $D/N \approx \pm 1$ compared to the completely ordered states.

by the diffusion of single defects, and can be neglected. The degeneracy of the disordered states due to defect pairs results in a shift,

$$\beta F_{\mathrm{p}} = -\ln Z_{\mathrm{p}} = -N \ln(1 + e^{-\beta E_{\mathrm{p}}}), \qquad (3.71)$$

of the free energy given by Eq. (3.69). Taking this shift into account we obtain excellent agreement, as shown in Fig. 3.21.

We also observe that this shift is small for predominately ordered systems with $\lesssim 10^5$ molecules (for example, for a larger system size $N = 10^6$ the shift is only $\beta F_{\mathrm{p}} \approx 0.18$). Thus, the shift in the free energy can be neglected for these system sizes. For larger system sizes the shift increases the statistical weight of the disordered states. Since the statistical weight of the ordered states is already negligible for a system of uncorrelated defects only, this shift does not effect the thermodynamic behavior. As a consequence, the degeneracy of the disordered states with respect to the ordered states can be neglected if one is interested in averages over the probability distribution

function of the total dipole moment, like the average total dipole moment or its average fluctuations.

Thermodynamic limit

Finally, we have a look at the behavior of the partition function $\mathcal{Z}_N(D)$ when approaching the thermodynamic limit. The partition function for disordered states as a function of the dipole moment per site $d = D/N$ is given by

$$\mathcal{Z}_N(d) = b\left[I_0(bN\sqrt{1-d^2}) + \frac{I_1(Nb\sqrt{1-d^2})}{\sqrt{1-d^2)}} \right] . \tag{3.72}$$

For $y = Nb\sqrt{1-d^2} \gg 1$ the Bessel functions can be approximated by $I_\alpha(y) \approx e^y/\sqrt{2\pi y}$ and we can write the partition function as

$$\tilde{\mathcal{Z}}_N(y) \approx \frac{b}{\sqrt{2\pi y}}e^y\left[1 + \frac{Nb}{y} \right] . \tag{3.73}$$

For $d^2 \ll 1$, corresponding to $y/(Nb) \approx 1$, this expression becomes

$$\tilde{\mathcal{Z}}_N(y) \approx \frac{2b}{\sqrt{2\pi Nb}}e^y . \tag{3.74}$$

Using the first two terms of the Taylor series of y, $y \approx Nb(1 - d^2/2)$, the partition function of a disordered system with $-N < D < N$ given by Eq. (3.65) can be approximated by

$$\tilde{\mathcal{Z}}_N(D) \approx \frac{2be^{bN}}{\sqrt{2\pi Nb}}e^{-\frac{D^2 b}{2N}} . \tag{3.75}$$

Thus, in the thermodynamic limit the distribution function of the total dipole moment for $-N < D < N$ becomes Gaussian with variance $\sigma^2 = N/b = N\exp(\beta E_\mathcal{D})$.

3.4.4 Corresponding states

So far, we have seen that for long tubes in contact with a water bath at ambient conditions the dipole lattice model can be approximated by a system of uncorrelated defects. For the latter we find that the thermodynamic properties only depend on the product of the system size and the Boltzmann factor, Nb, where $b = e^{-\beta E_\mathcal{D}}$. Thus, systems for which Nb has the same value show the same thermodynamic behavior, as explained in the following.

The partition function of a system of completely uncorrelated defects is given by

$$Z_\text{s}(\beta, N) = 2\sum_{n=0}^{N} \binom{N}{n}e^{-\beta E_\mathcal{D} n} . \tag{3.76}$$

Using Stirling's formula and that the defect excitation energy is large, i.e., $e^{-\beta E_{\mathcal{D}}} \ll 1$, we can write the partition function as

$$Z_{\mathrm{s}}(\beta, N) \quad \approx \quad 2 \sum_{n=0}^{\infty} \frac{e^{(-\beta E_{\mathcal{D}} + \ln N) n}}{n!} = 2 \sum_{n=0}^{\infty} \frac{(Nb)^n}{n!} \,. \tag{3.77}$$

Similarly, the mean defect number is given by

$$\langle n_{\mathrm{d}} \rangle = N \frac{e^{-\beta E_{\mathcal{D}}}}{1 + e^{-\beta E_{\mathcal{D}}}} \approx e^{(-\beta E_{\mathcal{D}} + \ln N)} = Nb \,, \tag{3.78}$$

and the order probability, i.e., the probability that all dipoles point in the same direction, by

$$P_0(N) = (1 + e^{-\beta E_{\mathcal{D}}})^{-N} \approx 1 - e^{(-\beta E_{\mathcal{D}} + \ln N)} = 1 - Nb \,. \tag{3.79}$$

Thus, from the point of view of thermodynamics, a system of size N at an inverse temperature β can be viewed as a coarse grained description of a larger system with size N' and an inverse temperature β' if $Nb = N'b'$, i.e., if the relation

$$\frac{N}{N'} = e^{(\beta - \beta')E_{\mathcal{D}}} \tag{3.80}$$

is fulfilled. This equation can be used to test the assumption of uncorrelated defects, which we will be especially useful for the investigation of the dielectric response of nanopore water in the next chapter.

Chapter 4

Dielectric response of nanopore water

4.1 Introduction

In the previous chapter we have seen that a carbon nanotube in thermodynamic equilibrium with a heat and water reservoir at atmospheric pressure and room temperature is completely filled with a chain of single-file hydrogen bonded molecules [16,26]. For small tube lengths $\lesssim 0.1\,\mathrm{mm}$, the chain is orientationally ordered with all water molecules pointing in the same direction. Flips of the whole chain occur via the migration of a single, possibly protonated defect, a process which is fast compared to the persistence time of a completely ordered state. For large system sizes $\gtrsim 0.1\,\mathrm{mm}$ the chain of water molecules is orientationally disordered and consists of ordered domains connected by defect molecules acting as domain walls.

Here, we suggest how these order properties, which to date lack experimental verification, can be probed by dielectric spectroscopy. To this end, we investigate the linear response of nanopore water to a time-dependent homogeneous electric field in direction of the tube axis. As we shall see, the length and time scales involved are large but can be handled in simulations using the one-dimensional dipole lattice model that reproduces the free energetics of single-file water quantitatively [23, 26, 27]. Moreover, the model provides the theoretical framework to determine the fundamental properties of nanopore water, in particular the excitation energy and diffusion constant of defects, from dielectric spectroscopy experiments.

4.2   Static electric field

The transition from a predominately ordered system to a disordered system with increasing tube length is reflected in the free energy as a function of the total dipole moment (see Fig. 3.17). For short tubes, the free energy curves show two minima corresponding to the ordered states, effectively forming a two-state system. For long tubes, the free energy curve exhibits a single quadratic minimum for vanishing dipole moment with residual minima for the ordered states. For intermediate system sizes we observe a crossover behavior with two deep minima for the ordered states, and one shallow minimum for vanishing dipole moment. At all systems sizes the free energy is symmetric and thus the total dipole moment vanishes on average.

A homogeneous electric field, E, in direction of the tube axis couples to the total dipole moment M of the water chain and leads to an electrostatic interaction energy $-ME$. In the following, we additionally use the reduced total dipole moment $D = M/\mu$ and the reduced electric field $E_{\mathrm{f}} = E\mu/\epsilon$ for convenience.

Since the electric field couples to the total dipole moment, the distribution function, $P(D, E_{\mathrm{f}})$, of the total dipole moment, D, at field E_{f} can be obtained from the distribution function at vanishing field $P(D)$ as

$$P(D, E_{\mathrm{f}}) = \frac{P(D)e^{\beta D E_{\mathrm{f}}}}{\sum_{\{D\}} P(D)e^{\beta D E_{\mathrm{f}}}} \, . \tag{4.1}$$

With $\beta F(D, E_{\mathrm{f}}) = -\ln P(D, E_{\mathrm{f}})$, the free energy is given by

$$F(D, E_{\mathrm{f}}) = F(D) - D E_{\mathrm{f}} \, , \tag{4.2}$$

where $\beta F(D) = -\ln P(D)$ is the free energy for vanishing external field. Thus, the effect of an external homogeneous electric field in direction of the tube axis is to tilt the free energy curves as a function of the total dipole moment by $-D E_{\mathrm{f}}$.

We calculate $P(D)$ from Monte Carlo simulations (see Fig. 3.17) and from the analytical expression given by Eq. (3.66) and investigate first the alignment of the water molecules with the electric field, before we turn to the influence of the electric field on the total dipole moment of the chain.

4.2.1   Alignment probability

For water molecules within the chain, it is energetically favorable to align their dipole moments with the external field in direction of the tube axis. The probability that all water molecules are aligned with the external field
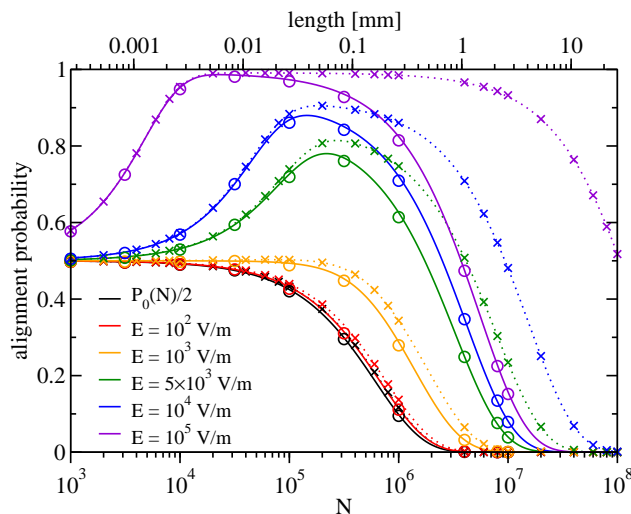
Figure 4.1: The alignment probability for different electric fields as a function of the system size. Lines are analytical results for uncorrelated defects (dotted lines) and for uncorrelated defects and defect pairs (solid lines). The crosses are numerical results for the NCA and circles are simulation results for the full Hamiltonian.

is given by $P(N, E_\mathrm{f})$ for a positive field and by $P(-N, E_\mathrm{f})$ for a negative field.

Figure 4.1 shows the alignment probability as a function of the system size for different strengths of the external electric field. Results for the full Hamiltonian agree well with numerical results for uncorrelated defects and defect pairs. For decreasing electric field, the alignment probability approaches half the order probability, Eq. (3.37), which corresponds to the alignment probability with an infinitely small electric field. The alignment probability increases with the strength of the external field which is coupled to the total dipole moment. Since the dipole moment of the ordered states increases with the chain length, the alignment probability also increases with the system size. This growth is opposed by the increase of the entropic contributions of disordered states with the chain length, which leads again to a decrease of the alignment probability for long tubes.

The simulation results of the NCA and analytical results for uncorrelated defects also shown in Fig. 4.1 agree well with each other, but overestimate the alignment probability as defect pairs are neglected. We have seen in Sec. 3.4.2 that, from a thermodynamical point of view, defect pairs essentially lead to a degeneracy of the disordered states. Since for long tubes the change in the total dipole moment caused by defect pairs is negligible,
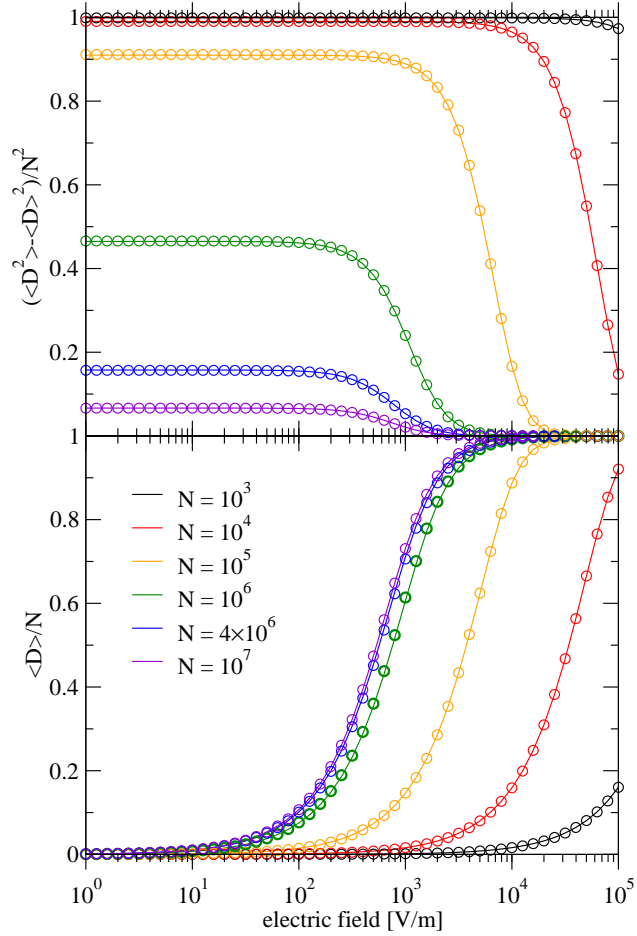
Figure 4.2: The average value (bottom) and the variance (top) of the total dipole moment per site as a function of the external electric field for different tube lengths. The analytical results are denoted by solid lines and simulation results by circles.

the alignment probability where defect pairs are neglected better reflects the macroscopic state of the system concerning the total dipole moment.

4.2.2   Static dielectric susceptibility

We obtain $P(D)$ from Monte Carlo simulations and from the analytical expression given by Eq. (3.66). Using Eq. (4.1), we determine the average value,

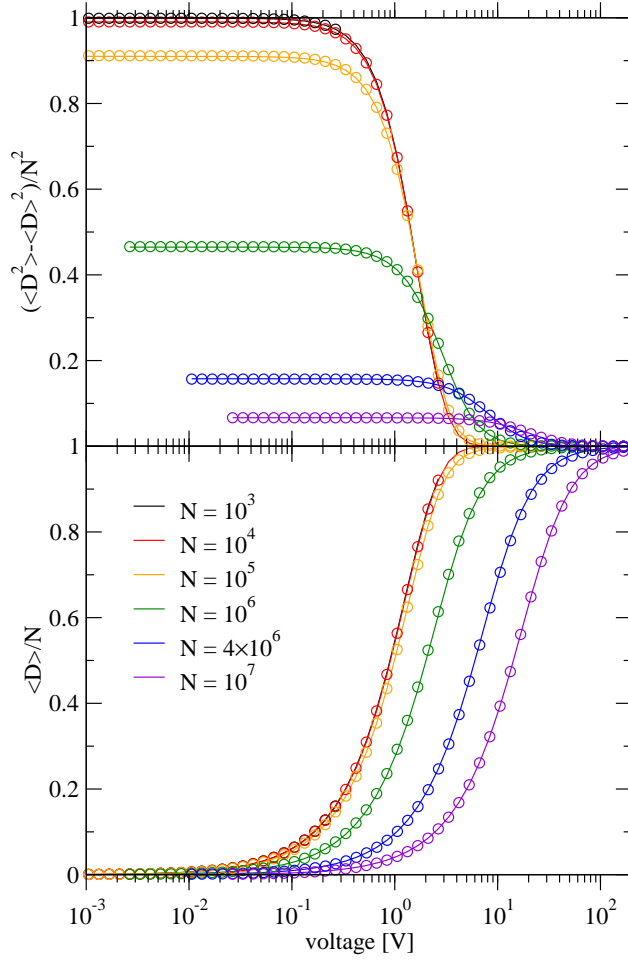$$\langle D \rangle = \sum_{\{D\}} D P(D, E_\mathrm{f}) \,, \qquad (4.3)$$

Figure 4.3: The average value (bottom) and the variance (top) of the total dipole moment per site as a function of the voltage applied to tubes of different lengths. The analytical results are denoted by solid lines and simulation results by circles.

and the variance,

$$\langle D^2 \rangle - \langle D \rangle^2 = \sum_{\{D\}} D^2 P(D, E_{\mathrm{f}}) - \langle D \rangle^2 \,, \tag{4.4}$$

of the total dipole moment as a function of the external electric field.

In Fig. 4.2 we show results for fields ranging from $E = 1\,\mathrm{V/m}$ to $E = 10^5\mathrm{V/m}$. The interaction energy of a dipole μ with a field $E = 1\mathrm{V/m}$ is $\sim 4 \times 10^{-9}\,\mathrm{kJ/mol}$ and thus about ten orders of magnitude smaller than $\epsilon \approx 25.8\,\mathrm{kJ/mol}$, the energy scale for the dipole-dipole interaction. Also, these fields are small compared to the ones used in molecular simulations of

short tubes in Ref. [52], where the properties of the water molecules within a chain remained unchanged by the fields used here. Thus, we are confident that for these electric field strengths our model is a good description of molecular water.

We observe that the longer the tube, the smaller the electric field required to align nearly all molecules in the field direction and maximize the total dipole moment, as expected from the alignment probability in Fig. 4.1. The variance starts to decrease from its value for vanishing external field when an average dipole moment of about 20% of the maximum dipole moment, $N\mu$, is reached. We find that the average dipole moment per site as a function of the system size has converged to its form in the thermodynamic limit for $N \approx 10^7$. For all tube lengths investigated here the simulation results for the full Hamiltonian are in excellent agreement with analytical results for uncorrelated defects.

Figure 4.3 shows the same data as in Fig. 4.2 as a function of the voltage $U = EL$, where L is the tube length, applied at the tube ends. We find that the curves for the average dipole moment per site lie on top of each other for predominately ordered systems with $\lesssim 10^5$ molecules. As a consequence, the static susceptibility χ is a linear function of the tube length for these system sizes, as we shall see in the next section.

Linear Response

The static dielectric susceptibility, χ, describes the response of the polarization, $\langle M \rangle / V$, of the tube to the electric field, E. It is defined as

$$\chi = \frac{1}{\varepsilon_0 V} \frac{\mathrm{d}\langle M \rangle}{\mathrm{d}E},$$

(4.5)

where V denotes the volume of the sample.

In the linear response regime, the static dielectric susceptibility can be determined from the equilibrium fluctuations of the total dipole moment for vanishing electric field via the fluctuation-dissipation theorem [56],

$$\chi = \frac{\beta}{\varepsilon_0 V} \left(\langle M^2 \rangle - \langle M \rangle^2 \right),$$

(4.6)

where angular brackets indicate the ensemble average. For vanishing average dipole moment, $\langle M \rangle = 0$, this equation becomes

$$\chi = \frac{\beta \langle M^2 \rangle}{\varepsilon_0 V},$$

(4.7)

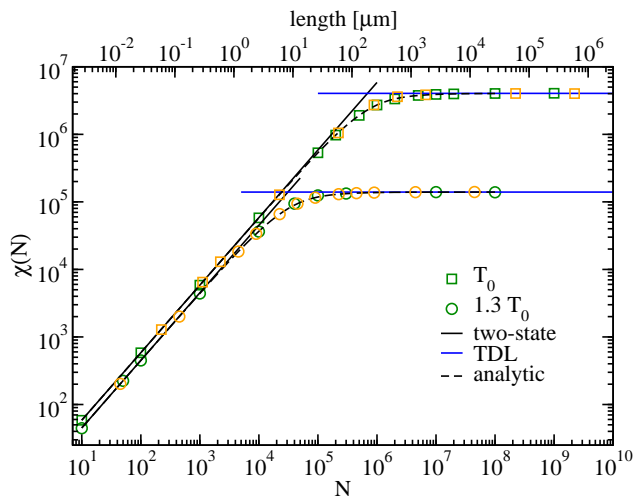where $\langle M^2 \rangle$ is the average value of the squared total dipole moment.

Figure 4.4: The static dielectric susceptibility, $\chi(N)$, of a water-filled tube with a diameter of 1 nm as a function of the system size for temperatures T_0 (squares) and $1.3\,T_0$ (circles). Estimates from Monte Carlo simulations are shown in green and rescaled data are shown in orange. Also shown are approximations for the dielectric susceptibility of a system of uncorrelated defects (dashed lines), the linear approximations for small system sizes (black, solid lines) and the values in the thermodynamic limit (blue, solid lines) for both temperatures.

In Fig. 4.4 we show results of Monte Carlo simulations using the full Hamiltonian, Eq. (2.28), for the static dielectric susceptibility χ for room temperature, $T_0 = 298\,K$, and $1.3\,T_0$. Note that $1.3\,T_0$ does not necessarily correspond to the same temperature for molecular water as our effective Hamiltonian implicitly depends on the temperature. We find for both temperatures that the static dielectric susceptibility increases linearly with the system size for short tubes, before it converges to its value in the thermodynamic limit.

The volume V in Eq. (4.7) can be written as $V = Nv$, where v is the volume per molecule. Here, we choose $v = r^2\pi a$ for a tube with radius $r = 0.5\,\text{nm}$. This choice leads to the giant value of $\chi_{\text{long}} \approx 4 \times 10^6$ for the dielectric susceptibility in the thermodynamic limit. For membranes of carbon nanotubes with an experimentally feasible tube density of $2.5 \times 10^{11}\,\text{cm}^{-2}$ [22] the dielectric susceptibility is lowered by a factor $\approx 1/500$. This value is still ~ 100 times larger than the dielectric susceptibility of bulk water ($\chi \approx 80$) although the water density is more than 3000 times smaller than in the bulk. Note that here we have assumed that interactions between

tubes can be neglected.

In the following we derive expressions for the dielectric susceptibility of a single chain in the limits of short and long tubes. In the two-state regime χ increases linearly with the chain length. From the fluctuation-dissipation theorem, Eq. (4.7), for a two-state system, where $\langle M^2 \rangle = N^2 \mu^2$, we obtain for the dielectric susceptibility

$$\chi_{\text{short}}(N) = \frac{\beta \mu^2}{\varepsilon_0 v} N \,, \tag{4.8}$$

which agrees excellently with simulation results shown in Fig. 4.4 for small tube lengths. This two-state behavior in the presence of an external electric field is confirmed by molecular dynamics simulations [52]. In this work, the authors apply a field of up to $\sim 10^9$ V/m to a chain of five water molecules. They compare simulation results of the average value and the variance of the total dipole moment to predictions of a two-state system and find them in excellent agreement. Only for field strengths larger than $\sim 2 \times 10^8$ V/m small polarization effects of the water molecules within the chain, compared to the average value of the dipole moment μ at vanishing external field, are observed.

For increasing tube length, chains become disordered. Due to the high defect excitation energy, the defect density is low and thus the average distance between defects is large. For typical configurations, the Coulomb-like interactions are weak and can be neglected. Then, a defect corresponds to a domain wall in the 1D Ising model with a coupling constant of half the defect excitation energy, $J = E_{\mathcal{D}}/2$. From the analytical solution of the 1D Ising model with periodic boundary conditions we obtain $\langle M^2 \rangle / N = e^{\beta E_{\mathcal{D}}}$ [57]. In the thermodynamic limit, where boundary conditions are of no importance, the dielectric susceptibility becomes

$$\chi_{\text{long}} = \frac{\beta \mu^2}{v \varepsilon_0} e^{\beta E_{\mathcal{D}}} \,. \tag{4.9}$$

At room temperature, this value is reached for $N \approx 10^7$ molecules (see Fig. 4.4).

This excellent agreement raises the question, if the Ising model allows estimates for the static dielectric susceptibility of shorter chains. Thus, we determine $\chi(N)$ as a function of the tube length from the distribution function of the magnetization for the Ising model with free boundary conditions (see Sec. 3.4.3). The partition function for fixed value of the total dipole moment $D = M/\mu$ is then given by

$$Z_N(D) = \begin{cases} 1 & \text{for} \quad |D| = N \\ b\left[I_0(by) + N I_1(by) y^{-1}\right] & \text{else,} \end{cases} \tag{4.10}$$

with $y = \sqrt{N^2 - D^2}$, $b = e^{-\beta E_{\mathcal{D}}}$, and where $I_0(x)$ and $I_1(x)$ are modified Bessel functions of the first kind [48]. With the average value of the squared dipole moment given by

$$\langle M^2 \rangle = \frac{\mu^2}{\sum_{\{D\}} Z_N(D)} \sum_{\{D\}} D^2 Z_N(D) \,, \tag{4.11}$$

we calculate the dielectric susceptibility using Eq. (4.7) numerically and find excellent agreement with simulation results for both temperatures and all system sizes investigated here (Fig. 4.4), indicating that defects are indeed uncorrelated to a large extent.

Corresponding States

For uncorrelated defects, we also find a relation between the static dielectric susceptibilities of corresponding states (see Sec. 3.4.4). In the limit of large system sizes, the partition function for states with at least a single domain wall (defect) for fixed total dipole moment, is given by Eq. (3.75) as

$$\tilde{\mathcal{Z}}_N(D) \approx \frac{2be^{bN}}{\sqrt{2\pi Nb}} e^{-\frac{D^2 b}{2N}} \,. \tag{4.12}$$

We calculate the average of the reduced total dipole moment squared as

$$\langle D^2 \rangle = \frac{1}{\tilde{\mathcal{Z}}_N} \left(2N^2 + \sum_{-N+3}^{N+3} D^2 \tilde{\mathcal{Z}}_N(D) \right) \,, \tag{4.13}$$

with the partitition function

$$\tilde{\mathcal{Z}}_N = 2 + \sum_{D=-N+3}^{N+3} \tilde{\mathcal{Z}}_N(D) \tag{4.14}$$

as normalization constant. For large system sizes, we approximate the sums by integrals,

$$\langle D^2 \rangle = \frac{1}{\tilde{\mathcal{Z}}_N} \left(2N^2 + \int_{-N+3}^{N+3} \mathrm{d}D D^2 \tilde{\mathcal{Z}}_N(D) \right) \,, \tag{4.15}$$

with

$$\tilde{\mathcal{Z}}_N = 2 + \int_{-N+3}^{N+3} \mathrm{d}D \tilde{\mathcal{Z}}_N(D) \,. \tag{4.16}$$

Integrating Eqs. (4.15) and (4.16) we obtain

$$\langle D^2 \rangle = \frac{N}{b} G(bN) \,, \tag{4.17}$$

where

$$G(y) = \frac{y - e^{y/2}\sqrt{\frac{2y}{\pi}} + e^y \mathrm{erf}\left(\sqrt{\frac{y}{2}}\right)}{e^y \mathrm{erf}\left(\sqrt{\frac{y}{2}}\right) + 1} . \tag{4.18}$$

Here, $y = bN = \exp[-\beta E_{\mathcal{D}} + \ln(N)]$ and $\mathrm{erf}(x)$ denotes the error function [48]. Thus, we obtain the following approximation for the dielectric susceptibility,

$$\chi(\beta, N) = \frac{\beta \mu^2}{\varepsilon_0 V} \frac{N}{b} G(bN) . \tag{4.19}$$

This expression captures the static dielectric susceptibility qualitatively, with the correct limits for short and long tubes. For small values of y, $G(y) \approx y$, and we find in agreement with Eq. (4.8),

$$\chi_{\mathrm{short}}(N) = \frac{\beta N^2 \mu^2}{\varepsilon_0 V} . \tag{4.20}$$

For large values of y the function $G(y)$ converges to $G(y) \approx 1$ and the dielectric susceptibility in the thermodynamic limit is given by

$$\chi_{\mathrm{long}} = \frac{\beta N \mu^2}{V \varepsilon_0} e^{\beta E_{\mathcal{D}}} , \tag{4.21}$$

as expected from Eq. (4.9).

The argument of the function $G(bN)$ in Eq. (4.19) has the same value for corresponding states, where $Nb = N'b'$. Since the volume is proportional to the tube length (for a single tube as well as for a membrane), i.e., $V = vN$ and $V' = vN'$, we obtain a relation between the dielectric susceptibilities of corresponding systems,

$$\frac{\chi(\beta, N)}{\chi(\beta', N')} = \frac{\beta}{\beta'} e^{(\beta - \beta') E_{\mathcal{D}}} . \tag{4.22}$$

We use this relation to obtain estimates for the static dielectric susceptibility at T_0 from simulations at $1.3\, T_0$, and the other way round, and find good agreement (see Fig. 4.4), further confirming the assumption of uncorrelated defects.

The limiting cases given by Eqs. (4.8) and (4.9) allow us to determine the average dipole moment of a water molecule along the tube axis, μ, and the defect excitation energy, $E_{\mathcal{D}}$, from the linear increase of the dielectric susceptibility at small system sizes and its value in the thermodynamic limit, provided we know $N = L/a$, where L is the length of the chain.

In summary, we have clarified the dielectric response of a hydrogen bonded chain of water molecules to a static, homogeneous electric field in

direction of the tube axis. Next, we investigate the dielectric response of the system to a time-dependent electric field which provides additional insight into the kinetic and dielectric properties of nanopore water.

4.3 Time-dependent electric fields

In general, the linear response of a system to a periodically varying electric field is described by

$$\frac{\langle M \rangle(\omega)}{V} = \varepsilon_0 \chi(\omega) E(\omega) \tag{4.23}$$

where ω is the frequency of the applied complex electric field, $E(\omega) = E e^{\imath \omega t}$, and $\chi(\omega)$ is the frequency dependent complex dielectric susceptibility. The latter is related to the complex dielectric constant via

$$\varepsilon(\omega) = 1 + \chi(\omega) = \varepsilon'(\omega) - \imath \varepsilon''(\omega), \tag{4.24}$$

where $\varepsilon'(\omega)$ denotes the real part and $\varepsilon''(\omega)$ the imaginary part.

The dielectric susceptibility can be determined from the time derivative of the time autocorrelation function of the total dipole moment by Fourier transformation [56],

$$\begin{aligned} \chi(\omega) &= \frac{\beta}{V \varepsilon_0} \int_0^\infty e^{-\imath \omega t} \langle \dot{M}(0) M(t) \rangle \mathrm{d}t = \\ &= -\frac{\beta}{V \varepsilon_0} \int_0^\infty e^{-\imath \omega t} \frac{\mathrm{d}}{\mathrm{d}t} \langle M(0) M(t) \rangle \mathrm{d}t. \end{aligned} \tag{4.25}$$

Thus, to determine the frequency-dependent dielectric constant of single-file water we have to know the kinetics of the total dipole moment, which is determined by the diffusive migration of orientational defects as we will discuss in the following.

4.3.1 Kinetic dipole lattice model

Molecular dynamics simulations show that the kinetics of defect generation, recombination, and migration involve the cleavage and formation of hydrogen bonds and the rotation of molecules. When a defect hops from one molecule to the next, the hydrogen bond between these two molecules is broken, the molecules rotate, and a new bond is formed [Fig. 4.5(a) and (b)]. Similarly, single defects are formed at the end of the chain, when the hydrogen bond between the end molecule and the next molecule is broken, the molecules rotate and form new bonds [Fig. 4.5(c)]. A defect is annihilated if it hops from the molecule next to the end molecule towards the
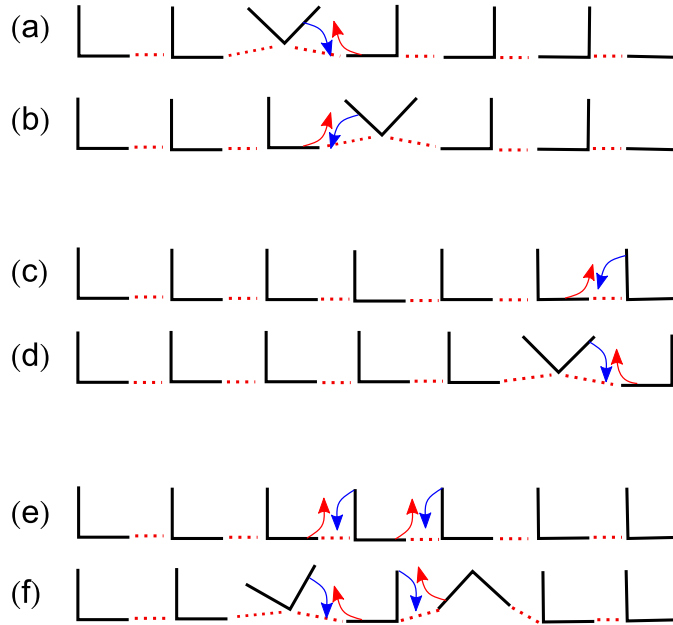
Figure 4.5: Mechanisms determining the kinetics of water chains. Water molecules are symbolized by black, right angles and hydrogen bonds are depicted as red, dotted lines. Rotations of molecules that break (form) a hydrogen bond are indicated with red (blue) arrows at the corresponding OH bonds. (a) Hop of a D-defect to the right and (b) to the left. (c) Generation and (d) annihilation of a D-defect at the chain end. (e) Generation of a defect pair and (f) recombination of defects.

end [Fig. 4.5(d)]. Within an ordered domain, defect pairs can be formed [Fig. 4.5(e)]. In this process, both hydrogen bonds of a single molecule are broken and the molecule itself and its two neighbors rotate and form new bonds. The molecules on the left and on the right of the center molecule form the two defects. A defect pair recombines, if one of these defects hops to the other one [Fig. 4.5(f)].

Since the kinetics of the reorientation of water molecules is determined by the diffusion of defects [23], we can use the dipole lattice model and implement the kinetics of water in nanopores as a Markov process [56]. We use discrete time, where one time unit, Δt, corresponds to the average time a single defect in an infinitely long chain needs to hop to a next neighbor site.

We only have to specify the transition rates for the displacement of a defect and the generation of defect pairs. All other events, i.e., defect recombination and annihilation at a chain end, can be viewed as a direct

consequence of defect diffusion: If the hop of a defect to an adjacent site brings it next to another defect, then these defects recombine. If a defect hops to the molecule at the chain end, then it is annihilated. The transition rates obey detailed balance to guarantee that the equilibrium distribution of states is conserved by the dynamics.

4.3.2 Kinetic simulation

In a straightforward implementation of the kinetic dipole lattice model, we proceed in the following steps. First, we randomly choose a site and perform a trial move. Which trial move is carried out depends on the position and orientation of the chosen molecule. Then, we accept or reject the trial move according to an acceptance criterion. We repeat this procedure N times before advancing the time by Δt.

The trial moves take into account the configurational constraints dictated by the model and we accept or reject them using either the Metropolis [58] or the Glauber [59] acceptance criterion, both obeying detailed balance. One of the trial moves is the displacement of a defect, which can lead to the annihilation of the defect at a chain end or to the recombination with another defect. If a molecule at a chain end is chosen, we try to generate a single defect at the molecule next to it. For a molecule within an ordered domain, we try the generation of a defect pair.

In Metropolis dynamics, the acceptance probability is given by

$$p_{\mathrm{M}}^{\mathrm{a}} = \min \left\{ 1, e^{-\beta \Delta E} \right\} , \qquad (4.26)$$

where ΔE is the energy difference between the new and the old state. For the diffusion of a defect on a flat energy landscape, where $\Delta E = 0$, the probability to stay at its position is $p = 0$, the probability to move to the left is $p = 1/2$ and to the right is $p = 1/2$.

In Glauber dynamics, the acceptance probability is given by

$$p_{\mathrm{G}}^{\mathrm{a}} = \frac{1}{1 + e^{\beta \Delta E}} . \qquad (4.27)$$

For the diffusion on a flat energy landscape the probability to accept a move to the left, $p = 1/4$, is equal to the probability to move to the right. Thus we have a probability $p = 1/2$ to stay at the original position.

The connection of simulation time to real time is established via the diffusion law in one dimension,

$$\langle x(t)^2 \rangle = 2Dt , \qquad (4.28)$$

where $x(t)$ is the displacement, t the time, and D the diffusion constant. Thus, we obtain for the hopping time, Δt, of a defect to an adjacent site, $\Delta t = a^2/(2D)$. At room temperature, L-defects with a diffusion constant of $D_L \approx 0.03\,\text{nm}^2/\text{ps}$ are slower than D-defects with a diffusion constant of $D_D \approx 0.05\,\text{nm}^2/\text{ps}$ [23]. For the moment, we use the average diffusion constant D given by

$$D = \frac{D_L + D_D}{2} \qquad (4.29)$$

for both kinds of defects obtaining $D = 0.04\,\text{nm}^2/\text{ps}$. As we shall see, under the assumption of uncorrelated defects and equal excitation energies for L- and D-defects, the time dependence of the total dipole moment is the same if one uses either the average diffusion constant, D, for both kinds of defects, or D_L and D_D for each kind of defects.

Demanding that the diffusion of a defect on a flat landscape occurs at the same speed as in molecular simulations, one sweep corresponds to a time $\Delta t_M = \Delta t \approx 0.88\,\text{ps}$ and $\Delta t_G = \Delta t/2 \approx 0.44\,\text{ps}$ using Metropolis and Glauber dynamics, respectively. Since Metropolis dynamics is twice as fast as Glauber dynamics, $\Delta t_M = 2\Delta t_G$, we use it for our simulations which agree well with predictions for Glauber dynamics, indicating that our results are not sensitive to the details of the dynamics.

Event-driven kinetic simulation

In large systems with a low density of defects the most frequently attempted move is the generation of a defect pair, which, however, has a very small acceptance probability. Thus, we spend a large amount of computing time selecting and rejecting the generation of defect pairs.

The situation is improved by introducing a cutoff in the effective charge interaction for the generation of defect pairs. For all other moves, we calculate the interaction energy using the full Hamiltonian without a cutoff. By doing so, we take advantage of the charge neutrality of defect pairs as L- and D-defect consist of charges of the same magnitude but opposite sign, forming an effective dipole parallel to the tube axis. The dipole moment of the defect pair determines the interaction energy for large distances (see Sec. 3.4.2).

Based on these results, we choose for the defect pair generation move a cutoff distance of 20 lattice spacings for the interaction of defect pairs with all other effective charges in the chain. Thus, the generation of a defect pair far from all other charges, i.e., outside the cutoff region of all other defects and chain end points, happens with a known rate.

To determine this rate we define two regions. Region A consists of all N_A sites within the cutoff distance of all defects. Region B is given by all other $N_B = N - N_A$ sites. The only trial move applicable in region B is the generation of a defect pair and since each site is further away from all other defects than the cutoff distance, the acceptance probability p_B^a is known independently from the actual configuration. For Metropolis dynamics the acceptance probability is given by $p_B^a = \exp(-\beta E_p)$ and for Glauber dynamics by $p_B^a = 1/[1 + \exp(\beta E_p)]$ with the defect pair excitation energy, E_p, given by Eq. (3.34).

An event in region A occurs if a site in this region is chosen, i.e., a move is attempted. Thus, the probability of an event in region A, p_A, is given by the generation probability of a trial move in region A as

$$p_A = p_A^g = \frac{N_A}{N}. \tag{4.30}$$

For an event in region B, a site in this region has to be chosen and the resulting move, i.e., defect pair generation, has to be successful. This is in contrast to an event in region A, where a trial move only has to be attempted. The probability of an event in B is given by the product of the generation probability $p_B^g = N_B/N$ and the acceptance probability p_B^a, i.e.,

$$p_B = p_B^g p_B^a. \tag{4.31}$$

The probability that one of these events happens is given by the sum of the probabilities of an event in region A and in region B,

$$p_e = p_A + p_B. \tag{4.32}$$

The waiting time between any of these two events, i.e., the number of time steps we have to uniformly choose a site until either a defect pair in region B is generated or a trial move in region A is selected, is given by the geometric distribution,

$$p(t) = p_e(1 - p_e)^{t-1}, \tag{4.33}$$

where t is the discrete time. The geometric distribution is the probability distribution of the number of trials, which have a random outcome that is considered to be either a success or a failure, needed to get one success. Consequently, we bridge the waiting time by drawing a time t from the geometric distribution and advancing the actual time by this time increment t. Then, we choose if we either perform an event in A or in B according to the probabilities

$$p_A' = \frac{p_A}{p_e} \tag{4.34}$$

and

$$p'_{\mathrm{B}} = \frac{p_{\mathrm{B}}}{p_{\mathrm{e}}} = 1 - p_{\mathrm{A}} \,. \tag{4.35}$$

We then draw a site within the corresponding region from a uniform distribution and perform a trial move. If this move is accepted, which is always the case for region B, then we update the sizes of regions A and B.

This algorithm allows us to do kinetic simulations for macroscopic system sizes, spanning huge time scales from picoseconds to milliseconds.

4.3.3   Debye behavior

We perform extensive kinetic simulations and determine the time autocorrelation function of the total dipole moment at a temperature $1.3\,T_0 \approx 384\,\mathrm{K}$, as shown in Fig. 4.6. We find that for times $t \gg \Delta t$ the autocorrelation functions decay exponentially for all system sizes, ranging from the two-state regime to completely disordered states. Only for very short tubes and short times comparable to the hopping time, deviations of the exponential behavior were observed due to fast fluctuations of the total dipole moment between the values of the ordered states and states with a single defect close to the chain end. Apart from that, the autocorrelation functions are of the form

$$\langle M(0)M(t)\rangle = \langle M^2\rangle e^{-t/\tau} \tag{4.36}$$

and only depend on the average of the squared total dipole moment, $\langle M^2\rangle$, and the relaxation time τ.

At a temperature of $1.3\,T_0$, we observe similar order behavior as for room temperature, as illustrated by the order probability of a completely filled tube for both temperatures in Fig. 4.7. The simulation results agree well with predictions for uncorrelated defects. Also shown is the rescaling of the data for $1.3\,T_0$ to room temperature using Eq. (3.80), which agrees well with the data obtained at this temperature. For small tube lengths, we find predominately ordered systems for both temperatures. At the higher temperature, the order probability is always smaller than one, even for the shortest tubes, indicating deviations from true two-state behavior.

We have chosen do to simulations and determine the time autocorrelation function of the total dipole moment at 1.3 times room temperature, because at room temperature the time scales for long tubes are too large to obtain good statistics for even a few multiples of the relaxation time within a reasonable amount of computing time.

Let us illustrate the computational requirements with the longest tube considered at $1.3\,T_0$, which consists of $N = 3 \times 10^5$ molecules, as an example.
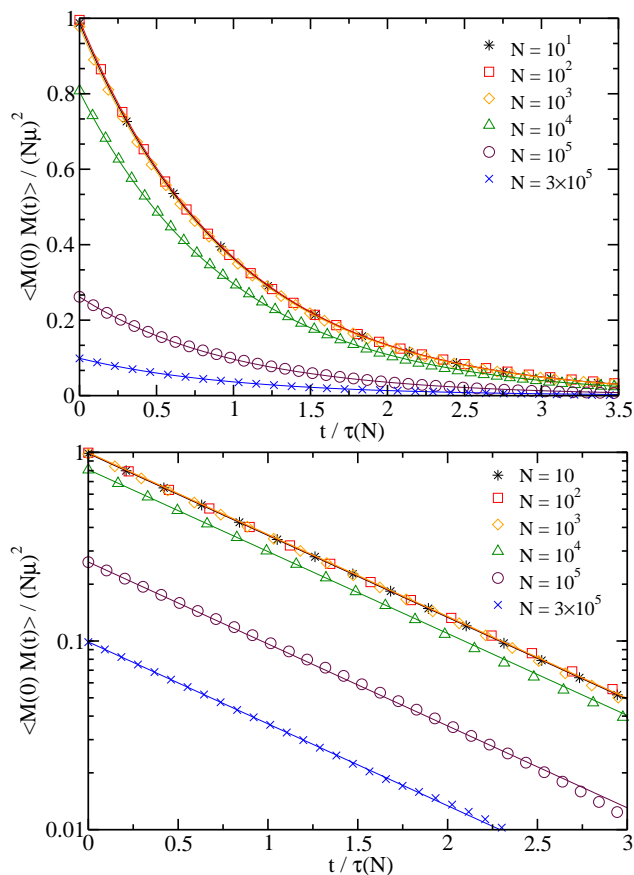
Figure 4.6: Simulation results for the time-dependent autocorrelation function of the total dipole moment for $T = 1.3\,T_0$ (symbols) and fitted curves (lines) as a function of the time divided by the corresponding size-dependent relaxation time, $\tau(N)$, for different system sizes. In the logarithmic plot at the bottom these correlation functions appear as linear functions with a slope of minus unity.

The relaxation time of the autocorrelation function is $\tau \approx 0.4\,\text{ms}$ which corresponds to $\sim 4.5 \times 10^8$ MC-sweeps ($\sim 10^{14}$ MC-steps) in a straightforward implementation of the kinetic model. In the event-driven kinetic simulation of this system, the number of MC-steps is reduced by $\sim 10^4$ steps, leading to $\sim 10^{10}$ MC-steps for a simulation with a length corresponding to just once the relaxation time. This example emphasizes the necessity of simplified models, efficient algorithms, and high performance computing facilities for the investigation of long tubes.

The exponential decay in the limits of short and long tubes has different reasons which is supported by analytical results. For short tubes, we
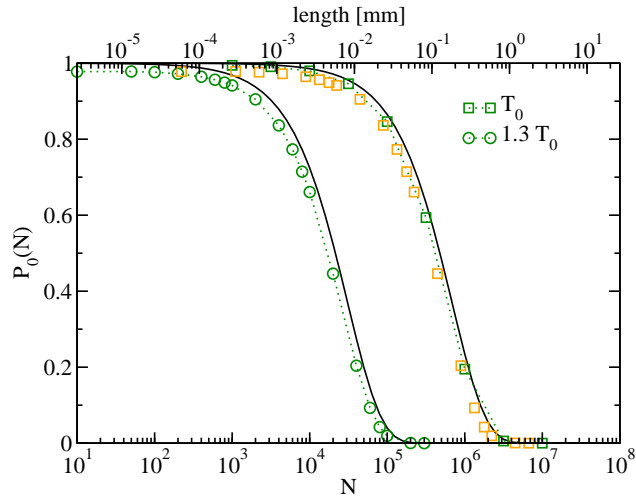
Figure 4.7: The order probability as a function of the system size at T_0 (squares) and at $1.3 \, T_0$ (circles). Estimates from Monte Carlo simulations are shown in green and rescaled data are shown in orange. The solid lines are predictions for uncorrelated defects. Dotted lines are used as guide to the eye.

observe two-state behavior with flips between the two ordered states of all dipoles aligned either "up" or "down" the tube axis. These flips are fast compared to the persistence times of the ordered states. Thus, the kinetics of short tubes is captured by a stochastic process of a two-state system with symmetric transition rates between the two states. In App. D we show how the exponential form of the time autocorrelation function of the total dipole moment can be derived for such a two-state system.

For long tubes we assume that defects are uncorrelated. In this limit our system can be related to the kinetic Ising model [59]. Identifying the magnetization with the total dipole moment we also find an exponentially decaying autocorrelation function in the thermodynamic limit (for details see App. E). Although the change in the total dipole moment is essentially caused by the diffusive motion of uncorrelated defects, defect generation and recombination are crucial for the observed time dependence of the autocorrelation function. The reason is that defect generation and recombination open reaction channels to regions of the phase space that would not be accessible otherwise.

Frequency-dependent dielectric constant

Dielectric relaxation characterized by exponential correlation functions of the form

$$\langle M(0)M(t)\rangle = \langle M^2\rangle e^{-t/\tau} \qquad (4.37)$$

is called Debye behavior [56]. In this case, one obtains from Eq. (4.25) for the real part of the dielectric susceptibility

$$\varepsilon'(\omega) - 1 = \chi\frac{1}{(1 + \omega^2\tau^2)}\,, \qquad (4.38)$$

and for the imaginary part,

$$\varepsilon''(\omega) = \chi\frac{\omega\tau}{(1 + \omega^2\tau^2)}\,. \qquad (4.39)$$

Thus, the dielectric constant is completely determined by the static susceptibility χ and the relaxation time τ. The static susceptibility depends on $\langle M^2\rangle$ and can be determined from Monte Carlo simulations (see Sec. 4.2.2). Estimates of both quantities can be obtained via exponential fits to the kinetic simulation data, as shown in Fig. 4.6.

4.3.4   Relaxation time

Figure 4.8 shows results for the relaxation time for $T = T_0$ and $T = 1.3\,T_0$ as obtained from fits to autocorrelation functions. At room temperature, we obtain an estimate of the relaxation time for $N = 10^6$ molecules from a fit to the autocorrelation function for a time shorter than the relaxation time and we could not obtain an estimate of τ for a completely disordered system of size $N = 10^7$ within a reasonable amount of computing time. Thus, strictly speaking, we have not confirmed Debye behavior for these systems in our simulations. Nevertheless, we can relate the results for $T = 1.3\,T_0$, where we have observed Debye behavior for all tube lengths, ranging from predominately ordered to completely disordered chains, to room temperature. To this end, we use the knowledge of corresponding states derived in Sec. 3.4.4 and show that the observed Debye behavior at $1.3\,T_0$ is characteristic for room temperature.

For corresponding systems of uncorrelated, diffusing defects obeying Eq. (3.80), we can also establish a relation between the dynamics (and thus the relaxation times) of these systems at different temperatures. Having two such corresponding systems and assuming that the smaller one is a coarse grained description of the other we can rescale time using the diffusion law,

i.e.,

$$t = t' \left(\frac{N}{N'} \right)^2 . \tag{4.40}$$

Figure 4.8 shows rescaled results for the relaxation times at $1.3\,T_0$ and room temperature using Eq. (4.40) for the time and Eq. (3.80) for the system size. The excellent agreement for long tubes, where Coulomb-like interaction can be neglected, strengthens the assumption of uncorrelated defects for both temperatures. Consequently, the Debye behavior observed at $1.3\,T_0$ (see Fig. 4.6) is a strong evidence for Debye behavior at room temperature for tube lengths, where our simulation results lack significance.

   As in the case of the static dielectric susceptibility, the relaxation time increases linearly for small, but not too small system sizes, before it converges to the thermodynamic limit. For both limits we find simple expressions for the relaxation time as discussed in the following.

Short tubes

Short chains show two-state behavior as the free energy curves have two deep minima for the ordered states separated by a nearly flat free energy barrier. The autocorrelation function of a two-state system decays exponentially and the relaxation time is given by

$$\tau = \frac{\tau_{\mathrm{MFP}}}{2} , \tag{4.41}$$

where the mean first passage time, τ_{MFP}, is the average time it takes the two-state system to change from one state to the other (see App. D).

   The orientation of the chain of water molecules is flipped by the diffusive migration of a single defect, which is either an L-defect or a D-defect. The free energy as a function of the total dipole moment acts as a potential of mean force on the defect, which performs uncorrelated hops to the left or right. In this non-linear one-step hopping process (NOSHP) [60] each value of the total dipole moment corresponds to a defect at a particular site n with free energy F_n. For hops of the defect, and hence for the total dipole moment, we define transition rates between adjacent sites. The forward transition rate, g_n, for a hop from site n to site $n + 1$ and the backward transition rate, r_n, for a hop from site n to site $n - 1$ are determined by imposing detailed balance,

$$\frac{g_n}{r_{n+1}} = e^{-\beta \Delta F_n} . \tag{4.42}$$

with $\Delta F_n = F_{n+1} - F_n$. This condition guarantees that the equilibrium distribution of states is conserved by the process. For Metropolis dynamics,
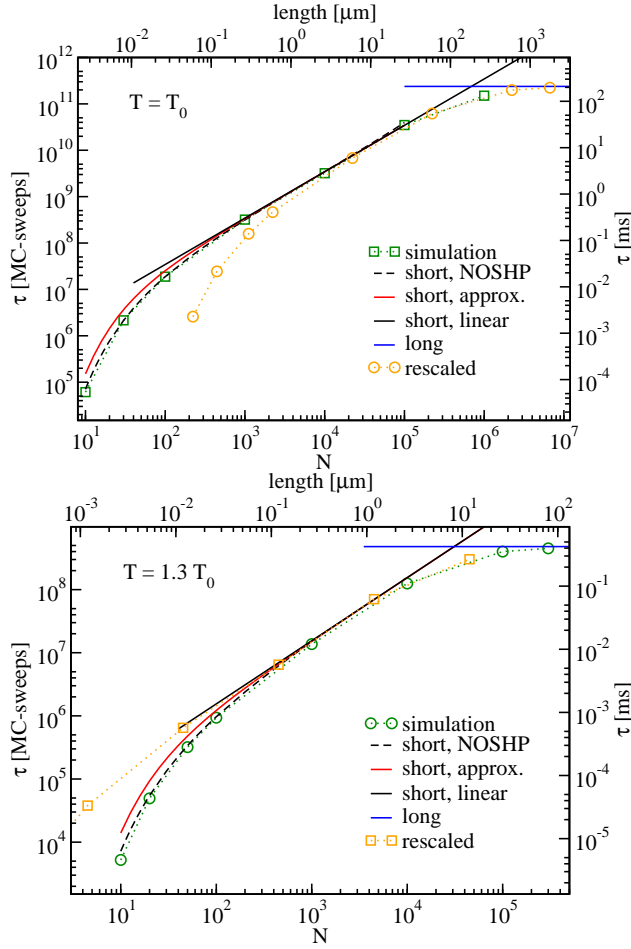
Figure 4.8: The relaxation time τ as a function of the number of molecules N (bottom axis) and the tube length (top axis) at room temperature (top) and at 1.3 times the room temperature (bottom). Estimates obtained directly from simulations are shown in green, rescaled data are shown in orange. Results from the numerical calculation of the relaxation time (NOSHP) for the two-state regime are shown as dashed lines, and for the approximation of a rectangular free energy barrier as red lines. The linear approximation for small sizes is shown as black solid line and the thermodynamic limit as blue line. The relaxation time is shown in units of Monte Carlo sweeps in a straightforward implementation of the kinetic model (left axis) and in units of milliseconds (right axis).

we obtain for the transition rates

$$g_n \quad = \quad \frac{1}{2\Delta t} \min\left\{1, e^{-\beta\Delta F_n}\right\} , \tag{4.43}$$

$$r_{n+1} \quad = \quad \frac{1}{2\Delta t} \min\left\{1, e^{\beta\Delta F_n}\right\} , \tag{4.44}$$

and for Glauber dynamics,

$$g_n = \frac{1}{\Delta t} \frac{1}{1 + e^{\beta \Delta F_n}}, \tag{4.45}$$

$$r_{n+1} = \frac{1}{\Delta t} \frac{1}{1 + e^{-\beta \Delta F_n}}. \tag{4.46}$$

To calculate the mean first passage time between the two ordered states, we consider an ensemble of independent random walkers. A walker corresponds to a defect and its position determines the total dipole moment of the chain. The mean first passage time is given by the average time a walker needs to reach site R starting from site $m < R$. If a random walker reaches site R, then it is annihilated, which corresponds to an absorbing boundary placed at R. We impose that all walkers starting at m will reach site R eventually by putting a reflecting boundary at $L \leq m$. In this case, we can write the mean first passage time as [60]

$$\tau_{R,m} = \sum_{\nu=m}^{R-1} \sum_{\mu=L}^{\nu} \frac{r_\nu r_{\nu-1} \cdots r_{\mu+1}}{g_\nu g_{\nu-1} \cdots g_{\mu+1} g_\mu} =$$

$$= \sum_{\nu=m}^{R-1} \sum_{\mu=L}^{\nu} \frac{e^{\beta(F_\nu - F_\mu)}}{g_\nu}, \tag{4.47}$$

where we have used the detailed balance condition, Eq. (4.42), to obtain the last line. The relaxation time is then given as half the mean first passage time from one ordered state to the other ($R = N$, $L = m = 1$),

$$\tau_{\text{short}} = \frac{1}{2} \sum_{\nu=1}^{N-1} \sum_{\mu=1}^{\nu} \frac{e^{\beta(F_\nu - F_\mu)}}{g_\nu}. \tag{4.48}$$

The free energy F_n experienced by a moving defect is given by the Hamiltonian in the charge picture, Eq. (2.28). We choose the ordered states as reference point for the total energy, $\beta F_1 = \beta F_N = 0$, and obtain

$$\beta F_n = \beta \Delta E(n) - \ln 2 \tag{4.49}$$

for $1 < n < N$, where $\ln 2$ accounts for the two reaction channels - one for a chain flip via the diffusion of an L-defect and one for the D-defect. $\Delta E(n)$ is given by the defect excitation energy plus the interaction energy of a single defect with the chain ends as

$$\Delta E(n) = \epsilon \left[2\Phi(N) - \Phi(n) - \Phi(n-1) \right.$$
$$\left. - \Phi(N-n) - \Phi(N-n+1) \right] + E_{\mathcal{D}}. \tag{4.50}$$

Simulation results for small system sizes agree well with results obtained by solving Eq. (4.48) for Metropolis dynamics numerically, as shown in Fig. 4.8. Results for Glauber dynamics are not shown since they agree well with results for Metropolis dynamics on the scale of this figure. With the free energy given by Eq. (4.49), the relaxation time, Eq. (4.48), explicitly depends on the energy constant ϵ which can be used to determine the dipole moment μ from fits of these expressions to experimental results. Moreover, such a fit would confirm the Coulomb-like interactions of the defect with the chain ends.

Since the free energy barrier between ordered states is flat for sufficiently long tubes, we can approximate the free energy landscape as a rectangular barrier. The height of the barrier is given by the defect excitation energy plus the Coulomb interaction of a defect located in the middle of the chain, $\beta F_{N/2}$, which becomes

$$\beta F_{N/2} \approx \beta \left(E_{\mathcal{D}} - \frac{3\epsilon}{N} \right) - \ln 2 \,. \tag{4.51}$$

This expression is accurate for $N \gtrsim 10$. In this case of a rectangular barrier, Eq. (4.48) can be simplified by counting the different terms that occur in the double sum. We obtain

$$\frac{\tau_{\mathrm{MFP}}^{\mathrm{M}}}{\Delta t_{\mathrm{M}}} = (N-1)\left(2e^{\beta F_{N/2}} + N - 2 \right) \tag{4.52}$$

for Metropolis dynamics and

$$\frac{\tau_{\mathrm{MFP}}^{\mathrm{G}}}{2\Delta t_{\mathrm{G}}} = (N-2)\left(2e^{\beta F_{N/2}} + e^{-\beta F_{N/2}} + N - 2 \right) + 2 \tag{4.53}$$

for Glauber dynamics. As long as the system size N is smaller than $e^{\beta F_{N/2}}$, but large enough so that the Coulomb-like interactions do not influence the barrier height, the relaxation time depends linearly on the tube length. The quadratic term in N in Eqs. (4.52) and (4.53) dominates for tube lengths where our assumption of a single defect no longer holds. Both, Metropolis and Glauber dynamics lead to the same results for the relaxation time for small systems, i.e.,

$$\tau_{\mathrm{short}}(N) \approx \frac{1}{2} e^{\beta(E_{\mathcal{D}} - 3\epsilon/N)} N \Delta t \,, \tag{4.54}$$

which reproduces simulation results for small chain lengths qualitatively (see Fig. 4.8). For increasing chain length the Coulomb attraction decreases

and can be neglected for sizes $N \gtrsim 1000$ at room temperature. Then, the relaxation time becomes

$$\tau_{\text{short}}(N) \approx \frac{1}{2} e^{\beta E_{\mathcal{D}}} N \Delta t \tag{4.55}$$

and increases linearly for tube lengths $1000 \lesssim N \lesssim 10^5$.

The basis for the above relaxation time calculations is that the system shows two-state behavior, which allows us to relate the mean first passage time to the relaxation time, and that the dynamics of the total dipole moment are determined by the diffusion of a single defect. Both conditions are violated for chains longer than $\sim 10^5$ molecules, where the system becomes increasingly disordered.

Long Tubes

For completely disordered systems we derive an analytical result under the assumption of uncorrelated defects. Glauber showed in Ref. [59] that for the kinetic Ising model with periodic boundary conditions, the time autocorrelation function of the total magnetization decays exponentially. Again, we establish the connection to real time with the diffusion law resulting in a spin flipping rate of $1/(2\Delta t)$. For large excitation energies, we obtain from Glauber's expression for the relaxation time

$$\tau_{\text{long}} \approx e^{2\beta E_{\mathcal{D}}} \Delta t \,. \tag{4.56}$$

We find good agreement with simulation results using Metropolis dynamics for $T = 1.3 \, T_0$, as shown in Fig. 4.8, indicating that these results do not depend on the details of the chosen dynamics. For room temperature we could not obtain an estimate for τ_{long} from simulations within a reasonable amount of computation time. Equating Eqs. (4.55) and (4.56) we obtain $N = \exp(\beta E_{\mathcal{D}})$ for the crossover length, at which the system changes from a predominately ordered to a predominately disordered state.

In summary, the simulation results depicted in Fig. 4.8 for small system sizes agree well with the numerical results obtained for the NOSHP. For large chain lengths, the relaxation time converges to its value in the thermodynamic limit given by Eq. (4.56). Equations (4.54) and (4.56) might be used to determine the effective diffusion constant and the defect excitation energy experimentally from the dielectric response of a system to a periodically varying electric field. By combining Eqs. (4.54) and (4.56), one can use the size dependence of the relaxation time in the linear and constant regime to determine the defect energy

$$E_{\mathcal{D}} = k_{\text{B}} T \ln \left(\frac{\tau_{\text{long}}}{2s} \right), \tag{4.57}$$

where s is the slope of the relaxation time as a function of N in the linear regime. The diffusion constant of the defects is then given by

$$D = \frac{a^2 \tau_{\text{long}}}{8s^2}. \tag{4.58}$$

Defect diffusion constants and excitation energies

Up to now, we have used the average diffusion constant and a single excitation energy for both kinds of defects. Under the assumption of uncorrelated defects, the time dependence of the total dipole moment of such a system cannot be distinguished from that of a system with different diffusion constants for L- and D-defects.

Let us assume an L-defect and a D-defect moving independently of each other. The total dipole moment at time t is determined by the distance, $\Delta x_{\text{LD}}(t)$, between these two defects. The average value of the squared distance can be written as

$$\langle \Delta x_{\text{LD}}^2(t) \rangle = \langle [x_{\text{L}}(t) - x_{\text{D}}(t)]^2 \rangle = \langle x_{\text{L}}^2(t) - 2x_{\text{L}}(t)x_{\text{D}}(t) + x_{\text{D}}^2(t) \rangle, \tag{4.59}$$

where $x_{\text{L}}(t)$ and $x_{\text{D}}(t)$ are the positions of the two defects. Using the diffusion law in one dimension, Eq. (4.28), this expression becomes

$$\langle \Delta x_{\text{LD}}^2(t) \rangle = \langle x_{\text{L}}^2(t) \rangle + \langle x_{\text{D}}^2(t) \rangle = 2(D_{\text{L}} + D_{\text{D}})t, \tag{4.60}$$

under the assumption of uncorrelated defects for which $\langle x_{\text{L}}(t)x_{\text{D}}(t) \rangle$ vanishes. Thus, the distance between the two defects obeys a diffusion law with a diffusion constant given by the sum of the diffusion constants of L- and D-defects. We expect that the total dipole moment shows the same time dependence if one uses either D_{L} and D_{D} or the average constant for both kinds of defects.

If the excitation energies of L- and D-defect, E_{L} and E_{D}, are different, then the defect excitation energy in the expressions for the static susceptibility [Eq. (4.9)] and the relaxation time [Eq. (4.56)] in the limit of long tubes is replaced by the average excitation energy, $(E_{\text{D}} + E_{\text{L}})/2$, as we shall see in the following.

In the static case, this follows directly from the partition function for n_{d} uncorrelated defects with different excitation energies. Since L- and D-defects alternate within a chain we have the same number of L- and D-defects if the total defect number is even. If it is odd, then these numbers differ by ± 1 which can be neglected for large n_{d}. Consequently, we assume that half of the n_{d} defects are L-defects and the other half are D-defects, which determines the total energy. The number of possibilities to place n_{d} defects

on the sites of a one-dimensional lattice is given by a binomial coefficient. Thus, the partition function is given by

$$Z = \sum_{n_\mathrm{d}=1}^{n_\mathrm{d}^\mathrm{max}} \binom{N}{n_\mathrm{d}} e^{-\beta \frac{n_\mathrm{d}}{2}(E_\mathrm{L}+E_\mathrm{D})} , \qquad (4.61)$$

which depends on the sum of the defect excitation energies only.

Regarding the influence of different excitation energies on the relaxation time in the thermodynamic limit, we recognize that the term $\exp(2\beta E_\mathcal{D})$ in Eq. (4.56) corresponds to the square of the average domain length. The latter is the average distance between neighboring defects, which is given by the inverse of the defect density, $N/\langle n_\mathrm{d} \rangle \approx \exp(\beta E_\mathcal{D})$. The origin of the square can be understood if one considers a chain of finite length with a single non-interacting defect. Simulation studies of such simple systems show that the relaxation time of the autocorrelation function of the defect position, which determines the autocorrelation function of the total dipole moment, is proportional to the tube length squared. Consequently, disordered systems of uncorrelated defects might be viewed as a composition of chains of length $\exp(\beta E_\mathcal{D})$, each of which carries a single non-interacting defect. Since the average defect density, and thus the average domain length, depends on the sum of the excitation energies, we can replace the defect excitation energy in Eq. (4.56) by the average value, $E_\mathcal{D} = (E_\mathrm{D} + E_\mathrm{L})/2$.

Only in the two-state regime we have to treat the reaction channels for an L-defect and a D-defect separately and Eq. (4.55) becomes

$$\tau_\mathrm{short}(N) = N \left(\frac{e^{-\beta E_\mathrm{L}}}{\Delta t_\mathrm{L}} + \frac{e^{-\beta E_\mathrm{D}}}{\Delta t_\mathrm{D}} \right)^{-1} , \qquad (4.62)$$

where Δt_L and Δt_D are the different hopping times of L- and D-defects. Still, the relaxation time increases linearly with N, but the slope is not determined by the average defect excitation energy and average diffusion constant. Since these quantities can be determined via Eqs. (4.8), (4.56), and (4.9), deviations of the relaxation time in the two-state regime from Eq. (4.55) could provide evidence for different defect excitation energies, possibly due to boundary effects. In molecular simulations of non-polar nanotubes, D-defects were energetically favorable which is consistant with the preferred orientation of water molecules entering the tube from the water bath [61]. A different behavior is observed in polar pores. The curvature of nanotubes is expected to induce a static dipole moment which causes an electric field at the tube ends, pointing towards the tube center [62]. Molecular simulations show that in such a tube an L-defect is preferred over a D-defect [37, 63].

4.4 Conclusion

In summary, the fluctuations of the total dipole moment are determined by the diffusion of highly uncorrelated defects. Hence, our results are neither affected by the details of defect generation and recombination nor by the details of the chosen diffusive dynamics. The latter is a consequence of our choice of the unit of time, which guarantees that the speed of diffusion of a defect in an infinitely long chain, i.e., an uncorrelated defect, is reproduced by our kinetic model.

A chain of hydrogen bonded water molecules inside a molecularly narrow pore shows Debye relaxation behavior. Performing dielectric spectroscopy, the frequency dependent dielectric constant can be measured. By fitting the Debye form to these results, the static susceptibility χ and the relaxation time τ can be determined. We found simple expressions for these quantities so that predictions about tube filling and macroscopic order can be tested and the defining properties (defect excitation energy, diffusion constant, dipole moment μ) can be measured. The static dielectric susceptibility and the relaxation time show a strong dependence on the tube length, which might be used for capacitors in sensor applications and other nanofluidic devices [64, 65].

Chapter 5

Outlook

In this work, we have developed a one-dimensional dipole lattice model for water in narrow nanopores and have investigated the properties of water in non-polar and pristine carbon nanotubes. We found that tubes with a sub-nanometer diameter, in contact with a water bath at room temperature and atmospheric pressure, are completely filled with a nearly contiguous chain of molecules, which remains predominately ordered up to a chain length of 0.1 mm.

We are currently investigating the consequences of our findings for membranes of parallel nanochannels (see Figure 5.1), which are considered to be promising building blocks of fuel cells [23, 66]. The interaction of ordered chains in different channels is determined by an effective Coulomb interaction of charges at the chain ends, which converges to a dipole-dipole interaction for large distances. Consequently, ordered chains of water molecules are anti-ferroelectrically coupled. Perfect anti-ferroelectric alignment, however, might be frustrated by the lattice geometry.

Although we have only considered non-polar and pristine pores in this work, the dipole lattice model is not restricted to such pores. The effects of tube polarizability and of defects in the tube wall can be included in our dipole lattice model provided that these effects are weak and do not destroy the structural properties of hydrogen bonded chains considered here.

A polarizable pore is expected to reduce the dipole moment of the water molecules in its interior [67], for which we can account by adjusting the model parameters.

Charged defects in the pore wall that interact electrostatically with the chain of water molecules might trap hydrogen bonding defects, similar to what is observed in aquaporin water channels [7, 68]. This effect, which might be used for the design of novel proton storage devices, is captured by
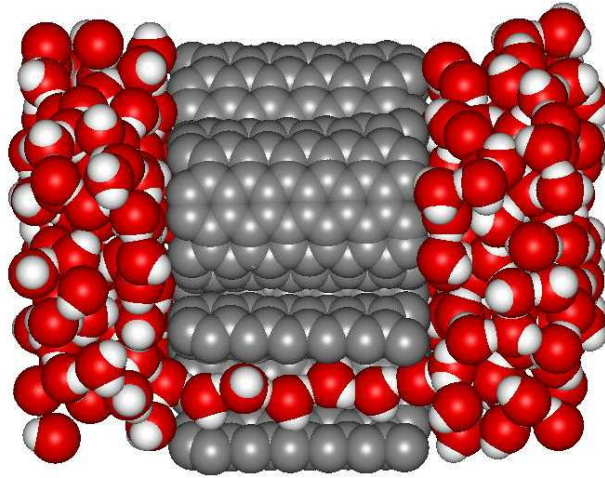
Figure 5.1: Snapshot of a molecular dynamics simulation of a membrane of carbon nanotubes immersed in water. One of the tubes is sliced open along the tube axis to show the hydrogen bonded chain of water molecules on the inside [32].

the dipole lattice model, as the dipoles simply couple to the electric field caused by the defect in the wall.

Another interesting possibility is to implement the kinetics of water transport in our model. This extension could facilitate the study of the filling and emptying kinetics of pores [47, 69], from nanoscopic to macroscopic lengths.

In conclusion, we are optimistic that the dipole lattice model will prove to be a reliable and versatile tool for future investigations and applications of the remarkable properties of water in nanopores.

Appendix A

Number of states

For the NCA and the SCA we can count the number of states as a function of the independent variables of the respective Hamiltonians. Here, we show the derivation for the SCA, where the number of states depends on the particle number n, chain number n_c, defect number n_d, and number n_I of single dipoles corresponding to segments of length one. For the simpler NCA, the derivation of the number of states is similar.

To model the free boundary conditions we add empty sections of length one to each end of our fully occupied system consisting of N sites. Thus, the fully occupied system is given by an empty section of length one, an occupied section of length N, and again an empty section of length one. These end sections are useful for the formulation of trial moves and for the derivation of the number of states, as we will see in the following.

To calculate the number of states, we first take a section of length $n - n_d - n_I$ and split it into $n_s - n_I$ parts, each of which is at least of length two, i.e., $l_{\min} = 2$. To split a section of M sites into m parts we have to choose $m - 1$ of the $M - 1$ points between sites where the section can be split. The number of possibilities to do so is given by the binomial coefficient $\binom{M-1}{m-1}$. If we demand that each new section consists of at least $l_{\min}$ sites then the number of points where we can split the section into parts is reduced by $(l_{\min} - 1)m$. Thus, the number of possibilities, γ, of splitting a section with M sites in m sub-sections, where each section has a length $l \geq l_{\min}$ is given by

$$\gamma = \binom{M - (l_{\min} - 1)m - 1}{m - 1}. \tag{A.1}$$

Inserting $M = n - n_d - n_I$, $m = n_s - n_I$, and $l_{\min} = 2$ in the above expression we obtain the first binomial coefficient of Eq. (2.32).

Next we count in how many ways we can combine the $n_s - n_I$ segments

with lengths larger than one and the n_I segments of length one to a particular sequence of these n_s segments. We do so by choosing positions for the n_I identical, single dipoles out of n_s possible positions, which gives the second binomial coefficient of Eq. (2.32). Then, we put the remaining $n_\mathrm{s} - n_\mathrm{I}$ segments of lengths larger than one on the remaining positions without changing their order, which is uniquely determined.

Grouping these segments to chains corresponds to splitting this sequence of n_s segments into n_c parts, each consisting of at least one segment. This gives the third binomial coefficient of Eq. (2.32). Each of these n_c chains has two possible orientations which gives the factor 2^{n_c}.

Finally, $N - n + 2$ empty sites have to be partitioned in $n_\mathrm{c} + 1$ sections that are at least of length one, i.e., $l_\mathrm{min} = 1$ in Eq. (A.1), which gives the last binomial coefficient of Eq. (2.32). By alternating empty sections and chains, a particular configuration is obtained, which is again uniquely determined.

To do Monte Carlo simulation of the SCA effective Hamiltonian given by Eq. (2.42), we need not only the degeneracy, but we also have to know the limits of the volume spanned by the variables $\{n, n_\mathrm{d}, n_\mathrm{c}, n_\mathrm{I}\}$, i.e., their minimum and maximum values. The minimum particle number is $n^\mathrm{min} = 0$ and the maximum particle number is $n^\mathrm{max}(N) = N$. The minimum number of defects is $n_\mathrm{d}^\mathrm{min} = 0$ and the maximum number is given by $n_\mathrm{d} = 0$ for $n < 3$ and otherwise

$$n_\mathrm{d}^\mathrm{max}(n) = \begin{cases} \frac{n}{2} - 1 & \text{for} \quad n \text{ even} \\ \frac{n-1}{2} & \text{for} \quad n \text{ odd} \end{cases} . \tag{A.2}$$

The minimum number of chains is

$$n_\mathrm{c}^\mathrm{min}(n) = \begin{cases} 0 & \text{for} \quad n = 0 \\ 1 & \text{for} \quad n > 0 \end{cases} \tag{A.3}$$

and the maximum number is $n_\mathrm{c}^\mathrm{max}(N, 0, n_\mathrm{d}) = 0$ for the empty system and otherwise

$$n_\mathrm{c}^\mathrm{max}(N, n, n_\mathrm{d}) = \min\{N - n + 1, n - 2n_\mathrm{d}\}. \tag{A.4}$$

The minimum number of chains of length one is given by

$$n_\mathrm{I}^\mathrm{min}(n, n_\mathrm{d}, n_\mathrm{c}) = \begin{cases} 0 & \text{for} \quad n - n_\mathrm{d} \geq 2n_\mathrm{s} \\ 2n_\mathrm{s} - n + n_\mathrm{d} & \text{for} \quad n - n_\mathrm{d} < 2n_\mathrm{s} \end{cases} . \tag{A.5}$$

The maximum number of chains of length one is given by

$$n_\mathrm{I}^\mathrm{max}(n, n_\mathrm{d}, n_\mathrm{c}) = \begin{cases} n_\mathrm{s} & \text{for} \quad n - n_\mathrm{d} = n_\mathrm{s} \\ n_\mathrm{s} - 1 & \text{for} \quad n_\mathrm{s} < n \end{cases} . \tag{A.6}$$

Appendix B

Monte Carlo simulation

B.1   Non-local trial moves

In the following we present the trial moves for the Monte Carlo simulation
of the dipole lattice model.

In the Metropolis algorithm [51], the transition probability from an old
state o to a new state n is given by the product of the generation probability
of a move, $P_{\text{gen}}(o \rightarrow n)$ and the acceptance probability, $P_{\text{acc}}(o \rightarrow n)$. Impos-
ing detailed balance, the Metropolis acceptance probability in the canonical
ensemble is given by

$$P_{\text{acc}}(o \rightarrow n) = \min \left\{ 1, \frac{P_{\text{gen}}(n \rightarrow o)e^{-\beta E(n)}}{P_{\text{gen}}(o \rightarrow n)e^{-\beta E(o)}} \right\} \tag{B.1}$$

and correspondingly for $P_{\text{acc}}(n \rightarrow o)$. In simulations of the grand-canonical
ensemble, the energies contain additional terms $-n \ln z$ where n is the fluc-
tuating particle number. Usually the generation probabilities of the forward
and the backward move are chosen to be equal and they cancel each other
in the above equation.

In our simulation, a configuration is given in the segment picture, i.e.,
by the lengths of all sections and their orientations. This is a simple way to
include the configurational constraints mentioned above but has the disad-
vantage that for some trial moves the generation probability for the forward
and the backward move is asymmetric. These asymmetric generation prob-
abilities have to be explicitly included in Eq. (B.1). This is the case for
defect generation and recombination, chain splitting and joining, and the
insertion and removal of a single dipole, as is explained below.

For simplicity, in the remaining part of this section we use the word
"choose" when we mean "choose with equal probability", i.e., when we draw

some quantity from a uniform distribution.

For the *displacement of a defect* we choose a chain $c \in \{1, \ldots, n_c\}$ that consists of m segments from which we choose segment $i \in \{1, \ldots, m-1\}$. We change the length of segment i by $d\Delta l$ and the length of segment $i+1$ by $-d\Delta l$ where we have chosen a length $\Delta l \in \{1, \Delta_{\max}\}$ and a direction $d = \pm 1$. The generation probability is given by

$$P_{\text{gen}}^{\text{dis}} = \frac{1}{2n_c(m-1)\Delta_{\max}} . \tag{B.2}$$

For the *generation of a defect* we choose a chain $c \in \{1, \ldots, n_c\}$ that consists of m segments from which we choose segment $i \in \{1, \ldots, m\}$. If the length of this segment, l, is long enough to carry a defect, i.e., $l \geq 3$, then we choose a length $l' \in \{1, \ldots, l-2\}$ and a direction $d = \pm 1$. The segment i is split into two segments of length $l_1 = l'$ and $l_2 = l - l' - 1$ and all segments of chain c, on the side given by d are reoriented. The generation probability is given by

$$P_{\text{gen}}^{\text{gen}} = \frac{1}{2n_c m(l-2)} . \tag{B.3}$$

This move increases the number of defects n_d by one.

For *defect recombination* we choose a chain $c \in \{1, \ldots, n_c\}$ that consists of m segments from which we choose segment $i \in \{1, \ldots, m-1\}$. Additionally we choose a direction $d = \pm 1$ and join segments i and $i+1$ to a new segment with length $l = l_i + l_{i+1} + 1$. All segments on the side d are reoriented. The generation probability is given by

$$P_{\text{gen}}^{\text{rec}} = \frac{1}{2n_c(m-1)} . \tag{B.4}$$

This moves decreases the number of defects n_d by one.

For the *displacement of a fragment* we choose a chain $c \in \{1, \ldots, n_c\}$, a direction $d = \pm 1$, and a displacement $\Delta l \in \{1, \ldots, \Delta_{\max}\}$. The empty section on the side d of the fragment is lengthened by Δl and the empty section on the opposite side is shortened by Δl. The generation probability is given by

$$P_{\text{gen}}^{\text{fra}} = \frac{1}{2n_c\Delta_{\max}} . \tag{B.5}$$

The generation probability for the *reorientation of a chain*, i.e., the reorientation of all segments of chain $c \in \{1, \ldots, n_c\}$, is given by

$$P_{\text{gen}}^{\text{reo}} = \frac{1}{n_c} . \tag{B.6}$$

The *exchange* move shortens a segment $i \in \{1, \ldots, m_1\}$ of fragment c_1 consisting of m_1 segments, and lengthens a segment $j \in \{1, \ldots, m_2\}$ of c_2

consisting of m_2 segments a length $\Delta l \in \{1, \Delta_{\max}\}$, therefore conserving the number of occupied sites. The generation probability is given by

$$P_{\text{gen}}^{\text{exc}} = \frac{1}{n_{\text{c}}^2 m_1 m_2} \,. \tag{B.7}$$

To *split a chain in two chains* we choose a chain $c \in \{1, \dots, n_{\text{c}}\}$ and a segment $i \in \{1, \dots, m\}$ of length l. Next we have to choose where in the segment i a bond is broken by choosing a length $l' \in \{1, l-1\}$. One of the new fragments is displaced in direction $d = \pm 1$ by a length $\Delta l \in \{1, \Delta_{\max}\}$. The generation probability is given by

$$P_{\text{gen}}^{\text{spl}} = \frac{1}{2 n_{\text{c}} m (l-1) \Delta_{\max}} \,. \tag{B.8}$$

This move increases the number of chains by one and the number of segments by one.

The inverse move is the *joining of two chains* to a single chain. We choose a chain $c \in \{1, \dots, n_{\text{c}} - 1\}$. If the last ordered segment of chain c and the first ordered segment of chain $c + 1$ have the same direction and if they are not further apart than $\Delta_{\max}$ (i.e., the length of the empty section between them is $l \leq \Delta_{\max}$) then we try to join them. We choose a direction $d = \pm 1$ that decides if the left chain is moved towards the right or the right chain towards the left. We get for the generation probability

$$P_{\text{gen}}^{\text{joi}} = \frac{1}{2(n_{\text{c}} - 1)} \,. \tag{B.9}$$

This move decreases the number of chains by one and the number of ordered segments by one.

Next we present moves that change the occupation number. The *transfer move* adds or removes dipoles at the end of chains. First we choose a chain $c \in \{1, \dots, n_{\text{c}}\}$, at which end particles are transferred ($d_1 = \pm 1$), and then how many particles ($\Delta l \in \{1, \Delta_{\max}\}$) are either added or removed by lengthening or shortening of the chosen end segment ($d_2 = \pm 1$). Lengthening of the end segment is only possible if the empty section next to it is longer than the number of added particles. This also guarantees that the number of chains is not changed. This gives a generation probability of

$$P_{\text{gen}}^{\text{tra}} = \frac{1}{4 n_{\text{c}} \Delta_{\max}} \,. \tag{B.10}$$

The above move is only applicable if there already are occupied sites. Therefore, we also *insert single dipoles* in empty sections. To do so we choose an empty section $i \in \{1, \dots, n_{\text{c}} + 1\}$ and a site by choosing a length

$l' \in \{1, l-2\}$ for the empty section on the left of the inserted dipole, which we assign an orientation $d = \pm 1$. This results in a generation probability

$$P_{\text{gen}}^{\text{ins}} = \frac{1}{2(n_{\text{c}} + 1)(l - 2)} \, . \tag{B.11}$$

This move increases the occupation number, the number of chains, and the number of ordered segments by one.

The inverse move *removes a single dipole* by choosing a chain with index $c \in \{1, \ldots, n_{\text{c}}\}$ and checking if it is of length one. If so, we remove the single dipole by eliminating this chain consisting of segment j and the empty section to its right with index $j + 1$. We assign the empty section to its left the new length $l'_{j-1} = l_{j-1} + l_{j+1} + 1$. The generation probability is

$$P_{\text{gen}}^{\text{rem}} = \frac{1}{n_{\text{c}}} \, . \tag{B.12}$$

This move decreases the occupation number, the number of chains, and the number of ordered segments by one.

B.2   Biased sampling

The particle number distribution function $P(n, z')$ at the fugacity z' is obtained from the particle number distribution function $P_w(n)$, that stems from a biased sampling simulation at the fugacity z, by unfolding of the weight function $w(n)$ and reweighting to the new fugacity z',

$$P(n, z') = \frac{1}{N(z')} P_w(n) z^{-w(n)} \left(\frac{z'}{z} \right)^n , \tag{B.13}$$

with the normalization constant $N(z')$ given by

$$N(z') = \sum_{n=0}^{N} P_w(n) z^{-w(n)} \left(\frac{z'}{z} \right)^n . \tag{B.14}$$

If we want to calculate the average value of the observable $\mathcal{O}$ (which can be any element of the sampled list or a function of these elements) from a biased simulation, we need the joint distribution function of the order parameter and the observable in the biased ensemble is given by

$$P_w(n, \mathcal{O}) = \frac{1}{M} \sum_i \delta(n^{(i)} - n) \delta(\mathcal{O}^{(i)} - \mathcal{O}) \tag{B.15}$$

for a discrete observable $\mathcal{O}$, where M is the number of samples and $\delta(x)$ is Dirac's delta function. We obtain the average of the observable $\mathcal{O}$ at a fugacity z' by evaluating

$$\langle\mathcal{O}\rangle = \frac{1}{N(z')}\sum_n\sum_{\mathcal{O}}P_w(n,\mathcal{O})\mathcal{O}z^{-w(n)}\left(\frac{z'}{z}\right)^n . \qquad \text{(B.16)}$$

Instead of calculating the two-dimensional histogram and performing the above average, we calculate the following average of the observable $\mathcal{O}$ for each value of the order parameter in the biased ensemble, i.e.,

$$\langle\mathcal{O}\rangle_w(n) = \sum_{\mathcal{O}}P_w(n,\mathcal{O})\mathcal{O} = \frac{1}{M}\sum_i\delta(n^{(i)}-n)\mathcal{O}^{(i)} . \qquad \text{(B.17)}$$

We then do the unfolding of the weight function and the reweighting to the new fugacity z' in a single step and obtain for the average of the observable $\mathcal{O}$ as a function of the order parameter

$$\langle\mathcal{O}\rangle(n) = \frac{1}{N(z')}\langle\mathcal{O}\rangle_w(n)z^{-w(n)}\left(\frac{z'}{z}\right)^n . \qquad \text{(B.18)}$$

The average value of the observable $\mathcal{O}$ at the new fugacity z' is then obtained as $\langle\mathcal{O}\rangle = \sum_n\langle\mathcal{O}\rangle(n)$.

Appendix C

Lattice gas

We determine the chemical potential, $\mu_{1/2}$, where the system is half filled by exploiting the isomorphism between the Ising model with dipole-dipole interactions in an external field in the canonical ensemble and a lattice gas in the grand canonical ensemble. This allows us to determine $\mu_{1/2}$ from symmetry considerations. The Hamiltonian of the lattice gas is given by

$$H = \frac{1}{2} \sum_{i,j} n_i n_j J(|j-i|), \qquad (C.1)$$

where $n_i = 0, 1$ is the occupation number of site i and the interaction potential is given by

$$J(|j-i|) = \begin{cases} 0 & \text{for} \quad i = j \\ E_{\text{c}} & \text{for} \quad |j-i| = 1 \\ -|j-i|^{-3} & \text{else} . \end{cases} \qquad (C.2)$$

The grand canonical partition function of this lattice gas is given by

$$\Xi = \sum_{n_k = 0,1} \exp\left[-\beta \left(\frac{1}{2} \sum_{i,j} n_i n_j J(|j-i|) - \mu \sum_i n_i \right) \right] . \qquad (C.3)$$

This partition function is isomorphic to the canonical partition function of the Ising model with dipole-dipole interactions

$$Q = \sum_{s_n = -1,1} \exp\left[-\beta \left(\frac{1}{2} \sum_{i,j} s_i s_j \tilde{J}(|j-i|) - h \sum_i s_i \right) \right] . \qquad (C.4)$$

as we shall see next.

We establish the isomorphism between the grand canonical partition function of the lattice gas and the canonical partition function of the Ising

model by relating spins s_i to the occupation numbers n_i via $s_i = 2n_i - 1$. Then, the interaction energy $\tilde{J}(|j - i|)$ is given by

$$\tilde{J}(|j - i|) = \frac{J(|j - i|)}{4}. \tag{C.5}$$

It follows that the chemical potential μ and the external field h are related via

$$\mu = 4\tilde{J} + 2h\,, \tag{C.6}$$

where we introduce $\tilde{J} = \sum_{k=1}^{\infty} \tilde{J}(k)$.

The magnetization of the Ising model as a function of the external field h is point symmetric about the origin. As consequence, for vanishing external field ($h = 0$) the average magnetization vanishes. This state of the Ising model corresponds to a half filled state of the lattice gas which allows us to calculate $\mu_{1/2}$. From Eq. (C.6) we obtain $\mu_{1/2} = 4\tilde{J} = \sum_{k=1}^{\infty} J(k) = E_\mathrm{c} - \sum_{k=2}^{\infty} k^{-3}$ for vanishing external field, which can be written as

$$\mu_{1/2} = E_\mathrm{c} + 1 - \zeta(3)\,, \tag{C.7}$$

using $\zeta(3) = \sum_{k=1}^{\infty} k^{-3}$, in agreement with Eq. (3.6).

Appendix D

Two-state system

For small system sizes, the total dipole moment of a chain of water molecules exhibits two-state behavior, which we discuss in the following. Let us assume that we have a system with two states A and B. The transition rates from state A to B, $k_{A \to B}$, and from state B to A, $k_{B \to A}$, are equal, i.e., $k_{A \to B} = k_{B \to A} = k$. The master equation is then given by

$$\dot{p}_A(t) = k[p_B(t) - p_A(t)], \qquad (D.1)$$
$$\dot{p}_B(t) = k[p_A(t) - p_B(t)], \qquad (D.2)$$

where $p_i(t)$ is the probability that the system is in state i at time t. These two equations are redundant as the equation $p_A(t) + p_B(t) = 1$ is fulfilled for all times t. Solving a single differential equation for $\Delta p(t) = p_B(t) - p_A(t)$,

$$-\frac{\mathrm{d}\Delta p(t)}{\mathrm{d}t} = 2k\Delta p(t), \qquad (D.3)$$

we obtain

$$\Delta p(t) = p_0 e^{-2kt}, \qquad (D.4)$$

where $p_0 \equiv \Delta p(0)$ is the initial condition. Thus, the time-dependent probabilities become

$$p_A(t, p_0) = \frac{1}{2}[1 - \Delta p(t)], \qquad (D.5)$$

$$p_B(t, p_0) = \frac{1}{2}[1 + \Delta p(t)], \qquad (D.6)$$

which are symmetric with respect to the initial condition,

$$p_A(t, p_0) = p_B(t, -p_0). \qquad (D.7)$$

Let us assume that state A and B correspond to the two ordered states with dipole moments M_A and M_B. To calculate the time autocorrelation

function of the dipole moment we take the average over initial conditions. In equilibrium the system is in state A ($p_0 = -1$) with a probability $\tilde{p}_A = 1/2$ and in state B ($p_0 = 1$) with $\tilde{p}_B = 1/2$. The autocorrelation function is given by

$$
\begin{aligned}
\langle M(0)M(t)\rangle &= \tilde{p}_A M_A \left[p_A(t,-1)M_A + p_B(t,-1)M_B \right] + \\
&\quad + \tilde{p}_B M_B \left[p_A(t,1)M_A + p_B(t,1)M_B \right]
\end{aligned}
\tag{D.8}
$$

and using Eqs. (D.5) and (D.6) we obtain

$$
\begin{aligned}
\langle M(0)M(t)\rangle &= M_A M_B \frac{1}{2}\left[1 - e^{-2kt} \right] + \\
&\quad + \frac{1}{2}\left(M_A^2 + M_B^2 \right) \frac{1}{2}\left[1 + e^{-2kt} \right].
\end{aligned}
\tag{D.9}
$$

For $M_A = -N\mu$ and $M_B = N\mu$, this autocorrelation function becomes

$$
\langle M(0)M(t)\rangle = N^2\mu^2 e^{-\frac{t}{\tau}},
\tag{D.10}
$$

where the relaxation time is given by $\tau = 1/(2k)$. The inverse transition rate, $1/k$, corresponds to the average time needed to change from one state to the other and is called the mean first passage time, $\tau_{\mathrm{MFP}} = 1/k$.

Appendix E

Kinetic Ising model

If we assume that defects are uncorrelated and neglect that domain walls are formed by defect molecules and not located between next neighbor sites, then our model corresponds to the one-dimensional Ising model with free boundary conditions.

Glauber used periodic boundary conditions for the kinetic Ising model, and we can draw conclusions from his results for our model in the thermodynamic limit, where boundary conditions do not play a role [59]. A domain wall in the kinetic Ising model corresponds to defect in the water chain, i.e., $2J = E_{\mathcal{D}}$, where J is the coupling constant. The rate of a spin flip is given by

$$p_{\mathrm{G}} = \frac{\alpha}{1 + e^{\beta \Delta E}} \, , \tag{E.1}$$

where ΔE is the energy difference between the new and the old state and $\alpha = 1/\Delta t_{\mathrm{G}}$ is the flipping rate of a free spin.

Starting from the master equations, Glauber has derived an expression for the time-dependent spin correlation function, which determines the time autocorrelation function of the magnetization. Replacing the magnetization by the total dipole moment, this autocorrelation function for the kinetic Ising model is given by

$$\langle M(0)M(t) \rangle = \langle M^2 \rangle e^{-|t|/\tau} \, , \tag{E.2}$$

where $M(t)$ is the total dipole moment depending on time t and angular brackets indicate canonical time averages. Glauber's expression for the average value of the squared total dipole moment is given by

$$\langle M^2 \rangle = \mu^2 N \frac{1 + \eta}{1 - \eta} \tag{E.3}$$

and for the inverse relaxation time by

$$\tau^{-1} = \alpha(1 - \gamma), \tag{E.4}$$

where $\gamma = \tanh(2J/k_{\mathrm{B}}T)$ and $\eta = \tanh(J/k_{\mathrm{B}}T)$. These expressions, valid for periodic boundary conditions at all system sizes, can be applied for our system with free boundary conditions in the thermodynamic limit. We identify the energetic cost of a domain wall in the Ising model, $2J$, with that in the dipole lattice model, $E_{\mathcal{D}}$, leading to $J = E_{\mathcal{D}}/2$. Using

$$\tanh(x) = \frac{e^x - e^{-x}}{e^x + e^{-x}} \, , \tag{E.5}$$

and in the following

$$1 - \tanh(x) = \frac{2}{1 + e^{2x}} \, , \tag{E.6}$$

the inverse relaxation time given by Eq. (E.4) becomes

$$\tau^{-1} = \frac{2}{\Delta t_{\mathrm{G}}[1 + e^{2\beta E_{\mathcal{D}}}]} \, . \tag{E.7}$$

For large defect excitation energies, the relaxation time can be approximated by

$$\tau \approx \frac{\Delta t_{\mathrm{G}}}{2} e^{2\beta E_{\mathcal{D}}} \, . \tag{E.8}$$

In summary, we expect an exponentially decaying autocorrelation function of the total dipole moment of a hydrogen bonded chain of water molecules in the thermodynamic limit, where defects are uncorrelated to a large extent.

Bibliography

[1] M. T. Tyree, Nature **423**, 923 (2003).

[2] D. N. Ku, Annual Review of Fluid Mechanics **29**, 399 (1997).

[3] M. Whitby and N. Quirke, Nat Nano **2**, 87 (2007).

[4] J. Pfahler, J. Harley, H. Bau, and J. Zemel, Sensors and Actuators A: Physical **22**, 431 (1989).

[5] S. A. Miller, V. Y. Young, and C. R. Martin, Journal of the American Chemical Society **123**, 12335 (2001).

[6] B. Hille, *Ion Channels of Excitable Membranes*, 3rd ed. (Sinauer Associates, Inc., Sunderland, 2001).

[7] E. Tajkhorshid, P. Nollert, M. O. Jensen, L. J. W. Miercke, J. O'Connell, R. M. Stroud, and K. Schulten, Science **296**, 525 (2002).

[8] R. Pomès and B. Roux, Biophysical Journal **75**, 33 (1998).

[9] R. Pomès and B. Roux, Biophysical Journal **82**, 2304 (2002).

[10] D. E. Sagnella and G. A. Voth, Biophysical Journal **70**, 2043 (1996).

[11] P. Brzezinski and R. Gennis, Journal of Bioenergetics and Biomembranes **40**, 521 (2008).

[12] M. Wikström, Current Opinion in Structural Biology **8**, 480 (1998).

[13] I. Schlichting, J. Berendzen, K. Chu, A. M. Stock, S. A. Maves, D. E. Benson, R. M. Sweet, D. Ringe, G. A. Petsko, and S. G. Sligar, Science **287**, 1615 (2000).

[14] J. C. Rasaiah, S. Garde, and G. Hummer, Annual Review of Physical Chemistry **59**, 713 (2008).

[15] C. Dellago and M. M. Naor, Computer Physics Communications **169**, 36 (2005), proceedings of the Europhysics Conference on Computational Physics 2004.

[16] G. Hummer, J. C. Rasaiah, and J. P. Noworyta, Nature **414**, 188 (2001).

[17] A. I. Kolesnikov, J.-M. Zanotti, C.-K. Loong, P. Thiyagarajan, A. P. Moravsky, R. O. Loutfy, and C. J. Burnham, Phys. Rev. Lett. **93**, 035503 (2004).

[18] N. Naguib, H. Ye, Y. Gogotsi, A. G. Yazicioglu, C. M. Megaridis, and M. Yoshimura, Nano Letters **4**, 2237 (2004).

[19] J. K. Holt, H. G. Park, Y. Wang, M. Stadermann, A. B. Artyukhin, C. P. Grigoropoulos, A. Noy, and O. Bakajin, Science **312**, 1034 (2006).

[20] J. K. Holt, A. Noy, T. Huser, D. Eaglesham, and O. Bakajin, Nano Letters **4**, 2245 (2004).

[21] F. Zhu and K. Schulten, Biophysical Journal **85**, 236 (2003).

[22] F. Fornasiero, H. G. Park, J. K. Holt, M. Stadermann, C. P. Grigoropoulos, A. Noy, and O. Bakajin, Proceedings of the National Academy of Sciences **105**, 17250 (2008).

[23] C. Dellago, M. M. Naor, and G. Hummer, Phys. Rev. Lett. **90**, 105902 (2003).

[24] D. Ruelle, Communications in Mathematical Physics **9**, 267 (1968).

[25] E. Luijten and H. W. J. Blöte, Phys. Rev. B **56**, 8945 (1997).

[26] J. Köfinger, G. Hummer, and C. Dellago, Proceedings of the National Academy of Sciences **105**, 13218 (2008).

[27] J. Köfinger, G. Hummer, and C. Dellago, J. Chem. Phys. **130**, (2009).

[28] L. Maibaum and D. Chandler, The Journal of Physical Chemistry B **107**, 1189 (2003).

[29] A. Kalra, S. Garde, and G. Hummer, Proceedings of the National Academy of Sciences of the United States of America **100**, 10175 (2003).

[30] B. Corry, The Journal of Physical Chemistry B **112**, 1427 (2008).

[31] C. Peter and G. Hummer, Biophysical Journal **89**, 2222 (2005).

[32] C. Dellago and G. Hummer, Physical Review Letters **97**, 245901 (2006).

[33] K.-D. Kreuer, S. J. Paddison, E. Spohr, and M. Schuster, Chemical Reviews **104**, 4637 (2004).

[34] C. R. Martin and Z. S. Siwy, Science **317**, 331 (2007).

[35] X. Liu, T. P. Bigioni, Y. Xu, A. M. Cassell, and B. A. Cruden, The Journal of Physical Chemistry B **110**, 20102 (2006).

[36] C. Y. Won and N. R. Aluru, Journal of the American Chemical Society **129**, 2748 (2007).

[37] C. Y. Won and N. R. Aluru, The Journal of Physical Chemistry C **112**, 1812 (2008).

[38] X. Blase, A. Rubio, S. G. Louie, and M. L. Cohen, EPL (Europhysics Letters) **28**, 335 (1994).

[39] N. G. Chopra, R. J. Luyken, K. Cherrey, V. H. Crespi, M. L. Cohen, S. G. Louie, and A. Zettl, Science **269**, 966 (1995).

[40] D. Xu, L. Sun, H. Li, L. Zhang, G. Guo, X. Zhao, and L. Gui, New Journal of Chemistry **27**, 300 (2003).

[41] E. V. Shevchenko, D. V. Talapin, N. A. Kotov, S. O'Brien, and C. B. Murray, Nature **439**, 55 (2006).

[42] V. F. Puntes, K. M. Krishnan, and P. Alivisatos, Applied Physics Letters **78**, 2187 (2001).

[43] K. Butter, P. H. H. Bomans, P. M. Frederik, G. J. Vroege, and A. P. Philipse, Nat Mater **2**, 88 (2003).

[44] B. H. Erne, M. Claesson, S. Sacanna, M. Klokkenburg, E. Bakelaar, and B. W. Kuipers, Journal of Magnetism and Magnetic Materials **311**, 145 (2007).

[45] T. Chou, Journal of Physics A: Mathematical and General **35**, 4515 (2002).

[46] T. Chou, Biophysical Journal **86**, 2827 (2004).

[47] X. Zhou, C.-Q. Li, and M. Iwamoto, The Journal of Chemical Physics **121**, 7996 (2004).

[48] *Handbook of Mathematical Functions*, edited by M. Abramowitz and I. A. Stegun (Dover, New York, 1965).

[49] F. Wang and D. P. Landau, Phys. Rev. E **64**, 056101 (2001).

[50] B. A. Berg and T. Neuhaus, Phys. Rev. Lett. **68**, 9 (1992).

[51] D. Frenkel and B. Smit, *Understanding Molecular Simulation* (Academic Press, New York, 2002).

[52] S. Vaitheeswaran, J. C. Rasaiah, and G. Hummer, The Journal of Chemical Physics **121**, 7955 (2004).

[53] W. L. Jorgensen, J. Chandrasekhar, J. D. Madura, R. W. Impey, and M. L. Klein, The Journal of Chemical Physics **79**, 926 (1983).

[54] T. Antal, M. Droz, and Z. Rácz, Journal of Physics A: Mathematical and General **37**, 1465 (2004).

[55] J. K. Gregory, D. C. Clary, K. Liu, M. G. Brown, and R. J. Saykally, Science **275**, 814 (1997).

[56] D. A. McQuarrie, *Statistical Mechanics*, 2$^{\text{nd}}$ ed. (University Science Books, New York, 2000).

[57] R. J. Baxter, *Exactly Solved Models in Statistical Mechanics* (Dover Publications, New York, 2007).

[58] M. Metropolis, A. W. Rosenbluth, M. N. Rosenbluth, A. N. Teller, and E. Teller, J. Chem. Phys. **21**, 1087 (1953).

[59] R. J. Glauber, Journal of Mathematical Physics **4**, 294 (1963).

[60] N. G. van Kampen, *Stochastic Processes in Physics and Chemistry* (Elsevier Science Publishers, Amsterdam, North-Holland, 1992).

[61] R. B. Best and G. Hummer, Proceedings of the National Academy of Sciences of the United States of America **102**, 6732 (2005).

[62] T. Dumitrica, C. M. Landis, and B. I. Yakobson, Chemical Physics Letters **360**, 182 (2002).

[63] U. Zimmerli, P. G. Gonnet, J. H. Walther, and P. Koumoutsakos, Nano Letters **5**, 1017 (2005).

[64] S. K. Saha and D. Chakravorty, Applied Physics Letters **89**, 043117 (2006).

[65] D. V. Matyushov, The Journal of Chemical Physics **127**, 054702 (2007).

[66] G. Menzl, J. Köfinger, and C. Dellago, to be published (2009).

[67] D. J. Mann and M. D. Halls, Phys. Rev. Lett. **90**, 195503 (2003).

[68] B. L. de Groot and H. Grubmuller, Science **294**, 2353 (2001).

[69] T. Chou, Phys. Rev. Lett. **80**, 85 (1998).

Index

113